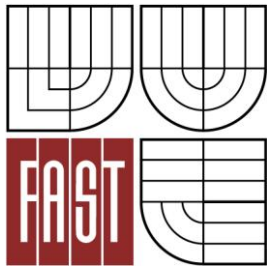




VYSOKÉ UČENÍ TECHNICKÉ V BRNĚ  
BRNO UNIVERSITY OF TECHNOLOGY



FAKULTA STAVEBNÍ  
ÚSTAV STAVEBNÍ MECHANIKY

FACULTY OF CIVIL ENGINEERING  
INSTITUTE OF STRUCTURAL MECHANICS

# ANALYSIS OF FRACTURE OF QUASI-BRITTLE MATERIALS USING NUMERICAL MODELLING AND ACOUSTIC/ELECTROMAGNETIC EMISSION

ANALÝZA PORUŠOVÁNÍ KVAZIKŘEHKÝCH MATERIÁLŮ ZA POUŽITÍ NUMERICKÉHO  
MODELOVÁNÍ A AKUSTICKÉ/ELEKTROMAGNETICKÉ EMISE

DIPLOMOVÁ PRÁCE  
MASTER'S THESIS

AUTOR PRÁCE  
AUTHOR

Bc. ONDŘEJ VODÁK

VEDOUCÍ PRÁCE  
SUPERVISOR

Ing. VÁCLAV VESELÝ, Ph.D.

BRNO 2013



# VYSOKÉ UČENÍ TECHNICKÉ V BRNĚ FAKULTA STAVEBNÍ

<b>Studijní program</b>	N3607 Stavební inženýrství
<b>Typ studijního programu</b>	Navazující magisterský studijní program s prezenční formou studia
<b>Studijní obor</b>	3608T001 Pozemní stavby
<b>Pracoviště</b>	Ústav stavební mechaniky

## ZADÁNÍ DIPLOMOVÉ PRÁCE

<b>Diplomant</b>	Bc. ONDŘEJ VODÁK
<b>Název</b>	Analýza porušování kvazikřehkých materiálů za použití numerického modelování a akustické/elektromagnetické emise
<b>Vedoucí diplomové práce</b>	Ing. Václav Veselý, Ph.D.
<b>Datum zadání diplomové práce</b>	31. 3. 2012
<b>Datum odevzdání diplomové práce</b>	11. 1. 2013
V Brně dne 31. 3. 2012	

.....  
prof. Ing. Drahomír Novák, DrSc.  
Vedoucí ústavu

.....  
prof. Ing. Rostislav Drochytka, CSc.  
Děkan Fakulty stavební VUT

### **Podklady a literatura**

- Červenka, V. a kol. (2007) ATENA Program Documentation, Praha: Cervenka Consulting.
- Bažant, Z. P., Planas, J. (1998) Fracture and size effect in concrete and other quasi-brittle materials. Boca Raton: CRC Press.
- Karihaloo, B. L. (1995) Fracture mechanics and structural concrete. New York: Longman Scientific & Technical.
- Jirásek, M. (1998) Numerical modeling of deformation and failure of materials. Czech Technical University, Prague.
- van Mier, J. G. M. (1997) Fracture Processes of Concrete: Assessment of Material Parameters for Fracture Models. Boca Raton: CRC Press.
- Další podklady dle pokynů vedoucího práce, zejména vědecké články o použití akustické a elektromagnetické emise při studiu porušování materiálů.

### **Zásady pro vypracování**

- Vypracujte rešerši použití nedestruktivních technik při studiu porušování materiálů.
- Vypracujte stručný přehled teorií porušování kvazikřehkých materiálů se zaměřením na vybrané teoretické aspekty materiálových modelů a výpočetních technik implementovaných v použitém softwaru.
- Vypracujte podrobné numerické modely testu v zadaných zkušebních konfiguracích.
- Vypracujte metody zpracování výsledků simulací vhodné pro porovnání se získanými experimentálními daty.
- S odladěnými numerickými modely proveďte parametrickou studii vlivu materiálových a konstrukčních parametrů (okrajových podmínek) na odezvu zkušebního tělesa.

### **Předepsané přílohy**

.....

Ing. Václav Veselý, Ph.D.  
Vedoucí diplomové práce

**Abstrakt**

Tato diplomová práce poskytuje přehled nedestruktivních testů betonu a podrobné informace týkající se akustické a elektromagnetické emise při monitorování porušování prostého betonu. Popisují se provedené zatěžovací zkoušky betonových vzorků a jsou vytvořeny numerické simulace těchto testů v softwaru ATENA. Výsledky simulací porušení vzorků jsou podrobně analyzovány a porovnávány s experimentálními výsledky zachycujícími procesy porušení prostřednictvím akustické a elektromagnetické emise. Většina výsledků simulací v softwaru ATENA 3D vykazuje dobrou shodu s naměřenými daty.

**Klíčová slova**

akustická emise, elektromagnetická emise, trhliny, numerická simulace, ATENA 2D, ATENA 3D, nedestruktivní zkoušení betonu, prostý beton, příčný tah

**Abstract**

This master thesis gives overview of non-destructive tests of concrete and provides detailed information concerning the acoustic and electromagnetic emission during monitoring of concrete failure. Conducted loading tests of plain concrete specimens are described in the thesis together with the performed numerical simulations of these tests in the software ATENA. The simulation results of concrete failure are analysed in detail and compared with the experimental results recording failure processes with the help of acoustic and electromagnetic emission. The majority of simulation results in software ATENA 3D show good agreement with the recorded data.

**Keywords**

acoustic emission, electromagnetic emission, cracks, numerical simulation, ATENA 2D, ATENA 3D, non-destructive testing of concrete, plain concrete, tensile splitting

### **Bibliografická citace VŠKP**

VODÁK, Ondřej. *Analysis of fracture of quasi-brittle materials using numerical modelling and acoustic/electromagnetic emission*. Brno, 2013. 112 s., XX s. příl. Diplomová práce. Vysoké učení technické v Brně, Fakulta stavební, Ústav stavební mechaniky. Vedoucí práce Ing. Václav Veselý, Ph.D..

**Prohlášení:**

Prohlašuji, že jsem diplomovou práci zpracoval samostatně a že jsem uvedl všechny použité informační zdroje.

V Brně dne 11.1.2013

.....  
podpis autora  
Ondřej Vodák

### **Poděkování:**

Tato práce vznikla v rámci řešení projektu Grantové agentury České republiky GAP104/11/0734 - Využití elektromagnetické a akustické emise ve výzkumu moderních kompozitních materiálů pro konstrukční aplikace

Rád bych poděkoval vedoucímu této práce Ing. Václavu Veselému, Ph.D. za odborné vedení, cenné rady, čas, pravidelné konzultace a ochotu a také kolegům podílejících se na řešení výše uvedeného projektu.

Dále bych chtěl poděkovat své rodině za podporu, Guro – protože je to skvělá holka, přátelům, spolubydlícím, kamarádům z práce, kde jsem dostal volno na dokončení diplomové práce a především mým očím za to, že to vydržely.

## Table of contents

<b>1</b>	<b>Introduction .....</b>	<b>1</b>
<b>2</b>	<b>Goals .....</b>	<b>2</b>
<b>3</b>	<b>Non-destructive testing of concrete.....</b>	<b>3</b>
3.1	<i>Introduction .....</i>	3
3.2	<i>The beginning of non-destructive testing.....</i>	3
3.3	<i>Surface hardness test.....</i>	4
3.4	<i>Penetration resistance test.....</i>	5
3.5	<i>Pull-out test .....</i>	6
3.6	<i>Break-off test .....</i>	6
3.7	<i>Tensile bond strength test.....</i>	7
3.8	<i>Maturity test.....</i>	7
3.9	<i>Pulse velocity test .....</i>	8
3.10	<i>Impact echo method.....</i>	8
3.11	<i>Other methods of non-destructive testing .....</i>	9
<b>4</b>	<b>Acoustic and electromagnetic emission .....</b>	<b>11</b>
4.1	<i>Acoustic emission .....</i>	11
4.1.1	<i>Introduction .....</i>	11
4.1.2	<i>History.....</i>	12
4.1.3	<i>AE sources .....</i>	12
4.1.4	<i>Acoustic waves.....</i>	14
4.1.5	<i>Set-up for the AE measurements .....</i>	16
4.2	<i>Electromagnetic emission.....</i>	18
<b>5</b>	<b>Experimental data .....</b>	<b>20</b>
5.1	<i>Introduction .....</i>	20
5.2	<i>Sets of specimens .....</i>	20
5.3	<i>Parameters of specimens .....</i>	22
5.4	<i>Compression tests of specimens.....</i>	25
5.5	<i>Ultrasonic pulse velocity method.....</i>	25



<b>6</b>	<b>Computational software ATENA – Program description and theoretical background.....</b>	<b>28</b>
6.1	<i>Introduction</i> .....	28
6.2	<i>Program description</i> .....	28
6.3	<i>Two-dimensional elasticity</i> .....	28
6.3.1	Plane stress.....	30
6.3.2	Plane strain.....	31
6.4	<i>Three-dimensional elasticity</i> .....	32
6.5	<i>Material model</i> .....	33
6.5.1	3D Non Linear Cementitious 2.....	33
6.5.2	SBeta.....	35
6.5.3	Parameters of constitutive model.....	36
6.5.4	Smearred cracks.....	37
6.5.5	Fixed crack model.....	37
6.5.6	Rotated crack model.....	37
6.5.7	Material stiffness matrices.....	39
6.6	<i>Nonlinear equations</i> .....	40
6.7	<i>Solution of nonlinear equations</i> .....	43
6.7.1	Linear solvers – Cholesky decomposition.....	43
6.7.2	Nonlinear solvers – Full Newton-Raphson method.....	44
6.7.3	Nonlinear solvers – Modified Newton-Raphson Method.....	45
6.7.4	Nonlinear solvers – Arc-length method.....	46
<b>7</b>	<b>Simulations in ATENA 2D.....</b>	<b>47</b>
7.1	<i>Parametric study</i> .....	47
7.1.1	Mesh connectivity.....	49
7.1.2	FE mesh size (density).....	52
7.1.3	Material model.....	59
7.2	<i>Failure location in 2D (AE + EME)</i> .....	61
7.3	<i>Conclusion</i> .....	65
<b>8</b>	<b>Simulations in ATENA 3D.....</b>	<b>66</b>
8.1	<i>Specimen set One</i> .....	67
8.2	<i>Specimen set Two</i> .....	68
8.3	<i>Failure location in 3D (AE + EME)</i> .....	69
8.3.1	Configuration BII.....	70
8.3.2	Configuration AI.....	71
8.3.3	Configuration AII.....	72

8.3.4	Conclusion.....	73
8.4	<i>Failure location in 3D (AE)</i> .....	74
8.4.1	Configuration CC.....	75
8.4.2	Configuration 1C.....	75
8.4.3	Configuration 2C.....	76
8.4.4	Conclusion.....	78
<b>9</b>	<b>Post-processing</b> .....	<b>80</b>
9.1	<i>Data processing in AtenaWin</i> .....	80
9.2	<i>Post-processing in Microsoft Excel</i> .....	81
9.2.1	Load Results workbook.....	81
9.2.2	Import of data workbook.....	84
9.2.3	Fracture strain 3D workbook.....	85
<b>10</b>	<b>Conclusion</b> .....	<b>87</b>
<b>11</b>	<b>Bibliography</b> .....	<b>89</b>
<b>12</b>	<b>List of symbols, physical constants and abbreviations</b> .....	<b>95</b>
<b>A</b>	<b>Appendix</b> .....	<b>II</b>

## List of Figures

Figure 3-1 : Two types of Schmidt hammer. Adopted from [6].	5
Figure 3-2 : Rebound principle of Schimdt hammer. Adopted from [6].	5
Figure 3-3 : Windsor probe. Adopted from [7].	6
Figure 3-4 : Typical failure of concrete from probe penetration. Adopted from [1].	6
Figure 4-1 : Scheme of acoustic emission testing. Adopted from [10].	11
Figure 4-2 : Example of slip dislocation. Only small force causes dislocation that moves gradually through a crystal grain (a-h). Adopted from [12].	13
Figure 4-3 : Basic AE history plot showing Kaiser effect (BCB), Felicity effect (DEF) and emission during hold (GH). Adopted from [10].	14
Figure 4-4 : Primitive AE wave released at a source. Adpoted from [10].	15
Figure 4-5 : Angular dependence of AE radiated from a growing microcrack. Adopted from [10].	15
Figure 4-6 : Schematic view of the transducer. Adopted from [10].	16
Figure 4-7 : Transducers attached to the surface of the measured concrete block	16
Figure 4-8 : Experimental set-up for the AE measurements	17
Figure 4-9 : Parallel plate capacitors formed by – (a) adjustable steel bracket, (b) graphite paste	19
Figure 5-1 : Configuration AI	20
Figure 5-2 : Configuration AII	20
Figure 5-3 : Configuration BII	20
Figure 5-4 : Configuration CC	21
Figure 5-5 : Configuration 1C	21
Figure 5-6 : Configuration 2C	21
Figure 5-7 : Sawed standard beam-shaped testing specimen	21
Figure 5-8 : Material testing machine FPZ-100/1	21
Figure 5-9 : Material testing machine Fröwag	21
Figure 5-10 : Scheme of sides and positions of dimensions – (a) Total view, (b) Individual sides	22
Figure 5-11 : Proceq TICO - Ultrasonic testing instrument	26
Figure 5-12 : Transducers and specimen R3K_V	26
Figure 6-1 : Two-dimensional state of stress. Adopted from [36].	29
Figure 6-2 : Principal stresses and their directions. Adopted from [36].	29
Figure 6-3 : Infinitesimal element at a point of the structure. Adopted from [36].	30
Figure 6-4 : Plate with fillet. Adopted from [36].	30
Figure 6-5 : Plate with hole. Adopted from [36].	30
Figure 6-6 : Rankine failure surface represented in Haigh-Westergaard coordinates – (a) 3D failure surface, (b) Rendulic plane (meridians) and (c) deviatoric plane (deviatoric section). Adopted from [39].	34
Figure 6-7 : Menétrey-Willam failure criterion represented in Haigh-Westergaard coordinates – (a) 3D failure surface, (b) Rendulic plane and (c) deviatoric plane. Adopted from [39].	34
Figure 6-8 : (a) Intersection of Rankine and Menétrey-Willam failure surfaces for $\lambda_t = 2$ and (b) no intersection for $\lambda_t = 1$ . Adopted from [39].	35

Figure 6-9 : Components of plane stress state. Adopted from [38].	36
Figure 6-10 : Components of strain state. Adopted from [38].	36
Figure 6-11: Fixed crack model. Stress and strain state. Adopted from [38].	37
Figure 6-12 : Rotated crack model. Stress and strain state. Adopted from [38].	38
Figure 6-13 : Fixed vs. rotated crack model - scheme of specimen and its L–D curves. Adopted from [41].	38
Figure 6-14 : Lagrangian mesh. Adopted from [42].	41
Figure 6-15 : Eulerian mesh. Adopted from [42].	42
Figure 6-16 : Full Newton-Raphson method. Adopted from [13].	46
Figure 6-17 : Modified Newton-Raphson method. Adopted from [13].	46
Figure 6-18 : The Arc-length method. Adopted from [13].	46
Figure 7-1 : Specimen with 2 steel loading prisms	47
Figure 7-2 : Monitors and boundary conditions	47
Figure 7-3 : SBeta_es10 load–displacement curves	50
Figure 7-4 : Failure by tensile splitting – (a) Real concrete specimen BII, (b) Numerical model Sbeta_es10_10x10	51
Figure 7-5 : Number of elements versus file for used specimens.	55
Figure 7-6 : Error warnings during execution of NLC2_es03_3x3 simulations	56
Figure 7-7 : Load–displacement curves for SBeta specimens.	56
Figure 7-8 : Load–displacement curves for NLC2sa specimens	56
Figure 7-9 : Load–displacement curves for NLC2se specimens	57
Figure 7-10 : Load–displacement curves for _es_05_5x5 specimens	60
Figure 7-11 : Example of load–displacement curve for splitting test. Adopted from [45].	60
Figure 7-12 : Scheme of specimen BII showing the determination of the spatial angle $\alpha$ between the normal vector of a plane of a forming crack and the normal vector of the capacitor's plate	61
Figure 7-13 : Histogram for BII specimens showing distance between fracture event and acoustic transducer	62
Figure 7-14 : Distances filtered by various filters – NLC2sa_es06_5x6 specimen.	64
Figure 7-15 : Distances of fracture events for specimen NLC2sa_es05_5x5.	65
Figure 7-16 : Distances of fracture events for specimens NLC2sa at step no.10 (peak point of L–D curve)	65
Figure 8-1 : Monitors and prescribed displacement of set One – (a) Total view, (b) Magnified upper part of specimen	68
Figure 8-2 : Monitors and prescribed displacement of set Two – (a) Total view, (b) Magnified upper part of specimen	69
Figure 8-3 : Load–displacement curves – 3D_BII vs. es_05_5x5	70
Figure 8-4 : Distances of fracture events – 3D_BII_step15	71
Figure 8-5 : Distances of fracture events – 3D_BII_5E-5.	71
Figure 8-6 : Load–displacement curves – Set One.	72
Figure 8-7 : Distances of fracture events – 3D_AI_step16	72
Figure 8-8 : Distances of fracture events – 3D_AII_step17	73
Figure 8-9 : Transducers positions – (a) "Front" view, (b) "Rear" view	73
Figure 8-10 : Horizontal–vertical displacement curves – R3K_IV_1C	74

Figure 8-11 : Load–displacement curves – R3K_CC.....	75
Figure 8-12 : Load–displacement curves – R4K_CC.....	75
Figure 8-13 : Load–displacement curves – R3K_IV_1C.....	76
Figure 8-14 : Distances of fracture events in the $x$ direction – 3D_R3I_2C_5E-5.....	77
Figure 8-15 : Distances of fracture events in the $y$ direction – 3D_R3I_2C_5E-5.....	77
Figure 8-16 : Distances of fracture events in the $z$ direction – 3D_R3I_2C_5E-5.....	77
Figure 8-17 : Load–displacement curves – R3I_2C.....	78
Figure 8-18 : Fracture plane – (a) Specimen R3K_II_1C, (b) Specimen R5I_2C .....	78
Figure 9-1 : Example of ATENA 3D results sheet .....	80
Figure 9-2 : AtenaWin error message .....	80
Figure 9-3 : LoadData Macro – VBA code.....	82
Figure 9-4 : Screenshot of worksheet in Load Results workbook.....	83
Figure 9-5 : MoveResults macro – VBA code.....	83
Figure 9-6 : Import of data macro – VBA code .....	84
Figure 9-7 : Scheme showing the determination of the spatial angle $\alpha$ between the normal vector of a plane of a forming crack and the normal vector of the capacitor's plate.....	86

## List of Tables

Table 5-1 : Dimensions of specimens with 2 steel prisms .....	23
Table 5-2 : Dimensions of specimens with 1 steel prism .....	23
Table 5-3 : Aggregate size of concrete mix .....	24
Table 5-4 : Specimen specific material weight .....	25
Table 5-5 : Compression tests of specimens .....	25
Table 5-6 : Specimens parameters for ultrasonic test.....	26
Table 5-7 : Strength classes for concrete C12/15 to C35/45 .....	27
Table 6-1 : Default formulae of material parameters .....	36
Table 7-1 : Relevant parameters of material models.....	48
Table 7-2 : Macro-element mesh settings for SBeta specimens.....	48
Table 7-3 : Generated mesh for SBeta_es10_2x2 and 8x10 specimens .....	49
Table 7-4 : Analysis information for SBeta_es10 specimens.....	50
Table 7-5 : Crack width SBeta_es10.....	51
Table 7-6 : Macro-element mesh settings for used specimens .....	53
Table 7-7 : Analysis information for used specimens .....	54
Table 7-8 : Generated mesh for XX_es05_5x5 specimen .....	55
Table 7-9 : Crack width SBeta specimens.....	57
Table 7-10 : Crack width and PFS NLC2 specimens .....	58
Table 7-11 : Crack pattern for _es04_4x4 and _es08_8x8 specimens .....	59
Table 7-12 : Intervals for classification of distances between the centre of fracture events and acoustic transducer .....	63
Table 7-13 : Filters applied to NLC2sa_es06_5x6 specimen.....	64
Table 8-1 : Relevant parameters of material models.....	68
Table 8-2 : Relevant parameters of material model for the set Two .....	76

# 1 Introduction

Sound is a part of daily life for most of the population (of course, excluding the people with hearing impairment). We are obtaining information concerning surrounding environment by means of hearing which is registering incoming acoustic waves. From the experiences we know that when something breaks into pieces, it is accompanied by noise (e.g. glass breaking). This acoustic phenomenon is connected with specific frequencies that allow us to recognise, more or less precise, what kind of material has been broken. On the other hand, not many people know the fact that such specific frequencies can be found in materials even during its loading. In other words, the energy is released in the form of acoustic waves even before the material completely breaks. It is possible to use this phenomenon, known as acoustic emission, for "listening" to the structural materials. This master thesis describes the way how to "listen" to the concrete (quasi-brittle material) and presents numerical models created in order to compare the numerical results with the test ones.

Location of fracture events arising in material is possible with a method using several acoustic transducers placed on the specimen surface. The method is similar to the process that takes place in our hearing system. We are able to locate sound events by means of time lag between incoming acoustic signals. Time lag is caused due to the fact that both our ears are placed at two different locations on our head. Thanks to this time lag, the brain can locate the sound event and the same task can do the transducers ("ears") connected to the computer ("brain").

In addition, there is another phenomenon known as electromagnetic emission. When a structure is subjected to an external stimulation (change in pressure, load or temperature), the energy is released in the form of electromagnetic field which can be recorded by a capacitor. Therefore, both mentioned phenomena enable to "take a look" inside the material without its destruction.

The reader will find overview of non-destructive tests of concrete, obtains detailed information concerning the acoustic and electromagnetic emission, tested specimens, their numerical representation in the software ATENA and comparison of the experimental results detecting acoustic/electromagnetic emission with the simulated ones.

## 2 Goals

The aim of this master thesis is to investigate the detection of acoustic/electromagnetic emission arising during mechanical testing of concrete specimens. The investigation is done with help of numerical simulations in program ATENA.

Individual tasks of the work are following:

- to create the suitable model representation of the real specimen/test,
- to find and calibrate the proper material model for simulations,
- to investigate which program outputs are proper to use for comparison with the experimental results,
- to approximately determine the smallest size of fracture events that the experimental technique is capable to detect.

In conclusion, this thesis describes strong and weak points of the experiments/simulations and suggests steps for further analysis.



## 3 Non-destructive testing of concrete

### 3.1 Introduction

Non-destructive test (NDT) methods are used to determine properties of hardened concrete and to evaluate the condition of concrete in deep foundations, bridges, buildings, pavements, dams and other concrete constructions. Non-destructive testing is defined as testing that causes no structurally significant damage to concrete.

There are many sources describing non-destructive testing of concrete, therefore, only portion of them were chosen [1; 2; 3; 4; 5] in order to form brief overview of NDT presented in this thesis.

NDT methods are applied to concrete construction for four primary reasons:

- quality control of new construction,
- troubleshooting of problems with new construction,
- condition evaluation of older concrete for rehabilitation purposes,
- quality assurance of concrete repairs.

There is no standard definition for NDT as applied to concrete. For some persons, they are tests that do not alter anyhow the concrete of the investigated structure. For some, they are tests that do not impair the function of a structure, in which case the drilling of cores is considered a NDT test. For others, they are tests that do less damage to the structure than drilling of cores. This overview deals with methods which either do not alter the concrete or result in only superficial local damage.

### 3.2 The beginning of non-destructive testing

Some of the first methods to evaluate the in-situ strength of concrete were adaptations of the Brinell hardness test for metals, which involves pushing a high strength steel ball into the test piece under a given force and measuring the area of the indentation. In the metals test, the load is applied by a hydraulic loading system. Modifications were required to enable this type of test to be made on a concrete structure. In 1934 Prof. K. Gaede reported on the use of a spring-driven impactor to supply the force to drive a steel ball into the concrete. A nonlinear, empirical relationship was obtained between cube strength and indentation diameter.

In 1938 there appeared a landmark paper by D.G.Skramtajev. It summarised 14 different techniques, 10 of which were developed for measuring the in-situ strength of concrete. Skramtajev divided the test methods into two groups:

1. methods that required installation of test hardware prior to placement of concrete

## 2. methods that did not require pre-installation of test hardware

The methods described by Skramtajev included the following: moulds placed in the structure to form in-situ test specimens; pullout tests of embedded bars; an in-situ punching shear test; an in-situ fracture test using a pincer-device; penetration of a chisel by hammer blows; guns that fired indentors into the concrete; and penetration of a ball by a spring-driven apparatus.

In 1938 another landmark paper was published which dealt with a truly NDT. The paper was by T.C. Powers who reported on the use of resonant frequency testing to establish the modulus of elasticity of concrete. Prismatic specimens were struck with a hammer, and the resulting resonant frequencies were determined by comparing the tones to those of calibrated steel bars. Subsequent advancements resulted in electronic devices that eliminated the need of matching tones by listening to sounds. Typically, these devices used a special speaker to vibrate the test specimen at variable frequencies and a transducer was used to measure the amplitude of the vibration. When the specimen was vibrated at its resonant frequency, maximum amplitude was noted.

### 3.3 Surface hardness test

In 1948 Ernst Schmidt, a Swiss engineer, developed a device for testing concrete based upon the rebound principle. The Schmidt rebound hammer (Figure 3-1) is principally a surface hardness tester. It works on the principle that the rebound of an elastic mass depends on the hardness of the surface against which the mass impinges. There is little apparent theoretical relationship between the strength of concrete and the rebound number of the hammer. However, within limits, empirical correlations have been established between strength properties and the rebound number and the hardness as measured by the Brinell method.

The way how to perform a rebound test can be observed in (Figure 3-2). During rebound, the slide indicator travels with the hammer mass and records the rebound distance (rebound number). The rebound distance is indicated by a pointer on a scale graduated from 0 to 100; the rebound readings are termed "R-values". These values give an indication of the concrete surface hardness with values increasing with the hardness of the concrete.

The rebound hammer provides a quick and inexpensive means of assessing the general quality of concrete and for locating areas of poor quality. A large number of readings can be taken rapidly so that large exposed areas can be scanned in a few hours. The Schmidt hammer should not be regarded as a substitute for standard compression tests but as a method for determining the uniformity of concrete in structures and comparing one concrete against another.



Figure 3-1 : Two types of Schmidt hammer. Adopted from [6].

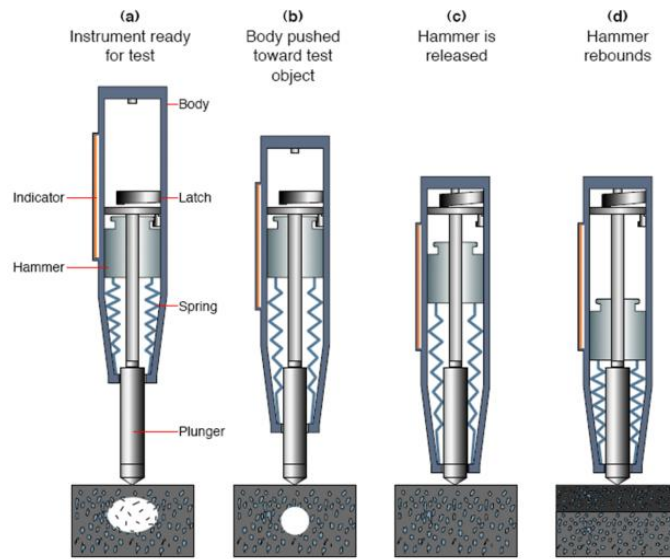


Figure 3-2 : Rebound principle of Schmidt hammer. Adopted from [6].

### 3.4 Penetration resistance test

The penetration resistance test is based on the depth of penetration of steel-alloy probes that are shot into the concrete. This method determines the hardness or penetration resistance of the concrete, which is related to its strength. The Windsor probe test system was introduced between 1964 and 1966.

Windsor probe, like the rebound hammer, is a hardness tester. The probe penetration relates to the compressive strength of the concrete below the surface, which makes it possible to develop empirical correlations between compressive strength properties and the penetration depth of the probe.

The Windsor probe (Figure 3-3) consists of a powder-actuated gun or driver into which a 6 mm diameter hardened steel-alloy probe is inserted and then driven into the concrete by firing a cartridge. After the probe is driven into the concrete, the exposed probe length is used as a measure of the penetration resistance. The depth of penetration is inversely proportional to the mortar strength and coarse aggregate hardness. The penetration resistance test is generally considered non-destructive; however, the probe leaves a minor hole in the concrete (Figure 3-4).

The Windsor probe is simple to operate, durable and requires minimal maintenance except for occasional cleaning of the gun barrel. The concrete strength correlations are affected by a relatively smaller number of variables than the rebound hammer.



Figure 3-3 : Windsor probe. Adopted from [7].

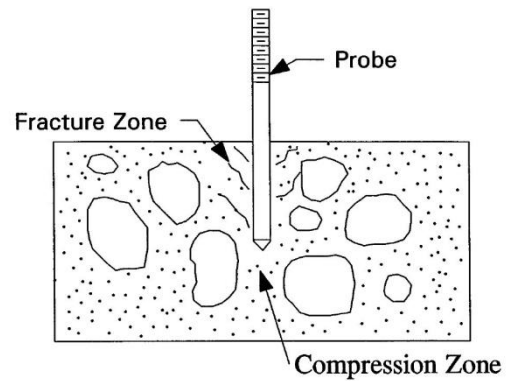


Figure 3-4 : Typical failure of concrete from probe penetration. Adopted from [1].

### 3.5 Pull-out test

The pull-out test measures the force required to pull an embedded metal insert from hardened concrete. The earliest known description of the pull-out test method was reported in 1938 by Skramtajev. In the pull-out test, a 25 mm diameter steel disc on a conical shaped stem is embedded at least 25 mm below the surface of the concrete during casting. A pull bolt is screwed into the stem of the disc and pulled by hydraulic force against a surface mounted reaction ring. The disc is loaded to failure by means of a hand operated portable hydraulic jack and the total force is measured on a gauge attached to the jack.

The pull-out test can be used during construction to estimate the in-situ strength of concrete to help determine whether construction activities such as form removal, application of post-tensioning, early opening to traffic or termination of cold weather protection can proceed. Because compressive strength is usually required to evaluate structural safety, the ultimate pull-out force measured during the in-situ test is converted to an equivalent compressive strength by means of correlation relationship.

### 3.6 Break-off test

The break-off test consists of breaking off an in-situ cylindrical concrete specimen at a failure plane parallel to the finished surface of the concrete. The cylindrical specimen is formed either by inserting a plastic sleeve into fresh concrete or by drilling a core after the concrete has hardened. The break-off stress at failure can then be related to the compressive strength or flexural strength of concrete using a predetermined relationship which relates the concrete strength to the break-off strength for a particular concrete mix.

The break-off method can be used both as quality control and quality assurance tools. The most practical use of the break-off test equipment is for determining the time for safe

form removal and the release time for transferring the force in pre-stressed or post-tensioned members. The main advantage of the break-off test is its ability to measure in-situ compressive strength. The equipment is safe and simple to use and the test is quickly performed and requires only one exposed surface. Test specimens can be obtained by drilling cores, thereby eliminating the need to pre-plan test locations prior to concrete placement. The test is reproducible to an acceptable degree of accuracy and correlates well with the compressive strength of concrete. The major disadvantage of the break-off test is the damage to the concrete member that requires patching. However, this test is considered to be non-destructive because the test member does not have to be removed and replaced.

### **3.7 Tensile bond strength test**

The rehabilitation of concrete commonly requires the removal of deteriorated concrete and repair with patch material and/or an overlay. To ensure long service of the rehabilitated concrete, it is important that the repair materials are well bonded to the underlying concrete. Proper surface preparation of the concrete is an important factor for the success of any repair. The tensile bond strength (pull-off) test is quick, simple and accurate method for determining how well the repair material is bonded to the underlying concrete.

The pull-off test, when used to predict the in-situ compressive strength of concrete, involves bonding a metal disc to the surface of the concrete with a rapid-set epoxy adhesive. After the epoxy has cured the loading device is used to apply a tensile force sufficient to pull the core out in tension. The total load applied divided by the cross-sectional area of the core or the metal disc for uncured sections is a direct measurement of the tensile strength of the concrete. Calibration graphs, based on pull-off tests and cube/cylinder compressive tests, provide a reliable estimate of equivalent cube/cylinder strengths.

This test is important because it is performed in-situ and can be reliably used as a quality control tool. It is very useful for assessing the best procedure to be used for surface preparation for patches or concrete overlays, as well as determining whether a bonding agent is required and the effect of the bonding agent on the bond strength.

### **3.8 Maturity test**

The maturity concept is a useful technique for estimating the strength gain of concrete at early ages. The method accounts for the combined effects of temperature and time on concrete strength development. An increase in the curing temperature can speed up the hydration process which will increase the strength development. Maturity is a function of the product of cur-

ing time and internal concrete temperature. It is then assumed that a given mix at equal maturities will have the same strength, independent of the curing time and temperature histories.

The maturity method has numerous applications in concrete constructions. It has been used successfully to estimate in-situ strength of concrete to assure critical construction operations, such as form removal or the application of pre-stressing or post-tensioning force.

The maturity method is a useful, easily implemented, accurate means of estimating in-situ concrete strength. Due to its simple application with the currently available maturity meters, the maturity method provides a viable means of reducing costs through testing and scheduling. Also, quality assurance costs can be reduced because the number of test cylinders is reduced by using the maturity concept.

### **3.9 Pulse velocity test**

The ultrasonic pulse velocity method can be used for detecting internal structure changes in concrete such as deterioration due to aggressive chemical environment, cracking and changes due to freezing and thawing. By using the pulse velocity method it is also possible to obtain the dynamic modulus of elasticity, Poisson's ratio, thickness of concrete slabs, and estimate the strength of concrete test specimens as well as in-situ concrete.

The pulse velocity method is a truly non-destructive method, as the technique involves the use of sonic waves resulting in no damage to the concrete element being tested. The same sample can be tested again and again, which is very useful for testing concrete undergoing internal structure changes over a long period of time or in case where the early-age strength development is needed.

The pulse velocity method is an excellent means for investigating the uniformity of concrete. The test procedure is simple and the equipment is readily available, portable and it is easy to use on the construction site and as it is in the laboratory.

The pulse velocity method was used for determination of dynamic modulus of elasticity and informative concrete compressive strength of test specimens used in this thesis in order to get specimen parameters prior to testing. The way of gauging is described in the subsection 5.5.

### **3.10 Impact echo method**

The use of acoustics methods is one of the oldest methods used to non-destructively determine flaws in material. Striking an object with hammer and listening to the quality of the

"ringing" sound has long been a useful technique for detecting cracks, voids and delaminations in concrete structures.

When a stress such as an impact is applied suddenly to a solid, the disturbance that is generated travels through the solid as stress waves. The principle of the impact-echo technique is that a transient stress pulse is introduced into a test object by mechanical impact on the surface.

Since the early 1970s, the impact-echo method has been used successfully for the evaluation of concrete piles. A stress pulse is produced by impacting the top surface and the returning echoes can be monitored by an accelerometer mounted on the same surface. The time-domain signal record is used to detect partial or complete discontinuities, such as voids, abrupt changes in cross section, very weak concrete and soil intrusions, as well as approximate location where such irregularities exist.

The impact-echo equipment is very lightweight, portable, easy to operate, and requires access to only one side of the structure. It is one of the few pieces of NDT equipment that can locate flaws as well as accurately determine at what depth the flaws are occurring. Results are achieved very quickly ( $< 10$  s) through the use of portable computer. The biggest disadvantage is the experience required to interpret the frequency results because the various materials that make up concrete generally cause numerous frequency peaks.

### 3.11 Other methods of non-destructive testing

Thorough description of NDT methods is beyond the extent of this master thesis, therefore this subsection includes only list of most of them:

- **Acoustic emission.** Described in detail in the following section.
- **Visual inspection.** Visual features may be related to structural serviceability, material deterioration and signs of distress (e.g. cracks, pop-outs, spalling, disintegration, colour change, weathering, staining surface blemishes and lack of uniformity).
- **Half-cell electrical potential method.** Potential of an embedded reinforcing bar is measured because the concrete functions as an electrolyte. Risk of corrosion of the reinforcement in the immediate region of the test location may be related empirically to the measured potential.
- **Carbonation depth measurement test.** Extent of carbonation can be determined easily by spraying a freshly exposed surface of the concrete with a 1% phenolphthalein solution. The calcium hydroxide is coloured pink while the carbonated portion is uncoloured.

- **Permeability test.** Permeability test measures the ease with which liquids, ions and gases can penetrate into the concrete.
- **Resistivity measurement.** It is an in-situ NDT method to obtain information related to the corrosion hazard of embedded reinforcement with help of resistivity measured by four electrodes which are placed in a straight line or just below the concrete surface at equal spacing.
- **Electromagnetic method.** With cover-meters using eddy current effect, currents in a search coil set up eddy currents in the reinforcement which in turn cause a change in the measured impedance of the search coil. This method enables to locate reinforcing bars and determine their orientation.
- **Radiographic testing method.** Intensity of a beam of X-rays or gamma rays suffers a loss of intensity while passing through a material. Radiography can be used to locate the position of reinforcement bar in reinforced concrete and also estimates can be made of bar diameter and depth below the surface. It can reveal the presence of voids, cracks and foreign materials, the presence or absence of grouting in post-tensioned construction and variation in the density of the concrete.
- **Infrared Thermography.** It records thermal radiation, which is naturally emitted from the concrete, as well as from all other objects. Thermographic testing technique is used for determining concrete subsurface voids, delaminations and other anomalies, e.g. fracturing.
- **Holographic technique.** It is a method of measuring minute surface displacement by examination of the fringe patterns generated when the surface is illuminated by a light beam and photographed under successive loading conditions. This method permits, among others, the examination of crack development.



## 4 Acoustic and electromagnetic emission

The mechanism of acoustic emission (AE) seems to be fully understood, being provided by transient elastic waves due to stress redistribution following fracture initiation/propagation. The origin of the electromagnetic emission (EME) from fracture is not completely clear and different attempts have been made to explain it [8; 9]. It is possible to employ the both abovementioned phenomena for non-destructive diagnostics of building materials or structures during loading.

### 4.1 Acoustic emission

The Acoustic emission itself and the testing with the help of the AE are well described in [10] therefore information given in the subsequent subsections is mainly gained from this source.

#### 4.1.1 Introduction

When a structure is subjected to an external stimulation (change in pressure, load or temperature), localised sources trigger the release of energy in the form of stress waves which propagate to the surface and are recorded by sensors (transducers). With the appropriate equipment and set-up, motions on the order of picometres ( $1 \times 10^{-12}$  m) can be identified. Sources of the AE vary from natural events like earthquakes and rock-bursts to the initiation and growth of cracks, slip and dislocation movements, melting, crystal twinning (twinning is a crystal disorder in which the specimen is composed of distinct domains whose orientations differ but are related in a particular, well-defined way [11]) and phase transformations in metals. In composites, matrix cracking, fibre breakage and debonding contribute to the acoustic emissions. The AE can be also measured and recorded in polymers, wood and concrete, among other materials.

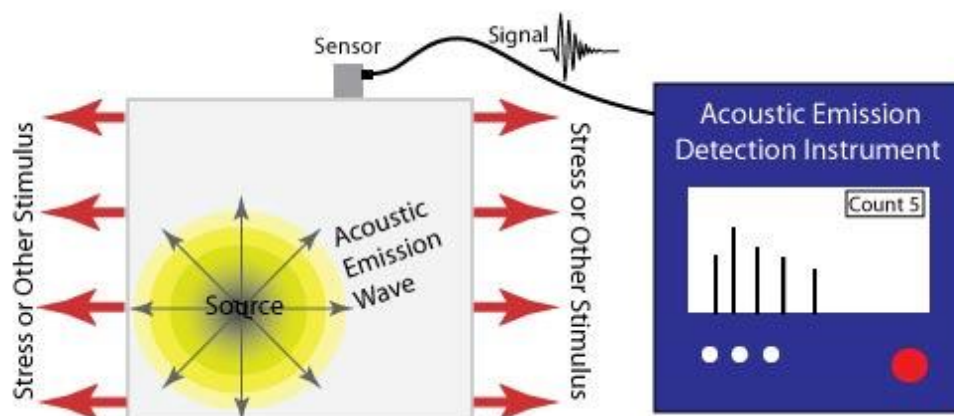


Figure 4-1 : Scheme of acoustic emission testing. Adopted from [10].

Detection and analysis of the AE signals can supply valuable information concerning the origin and importance of a discontinuity in the studied material. Because of the versatility of Acoustic Emission Testing (AET), it has many industrial applications (e.g. assessing structural integrity, testing for leaks, or monitoring weld quality) and is also used extensively as a research tool. Basic set-up for the acoustic emission testing represents Figure 4-1.

The acoustic emission is unlike most other non-destructive testing (NDT) techniques in two aspects. The first difference refers to the origin of the signal. Instead of supplying energy to the object under examination, the AET simply listens for the energy released by the object. The second difference is that the AET deals with dynamic processes, or changes, in a material. This is particularly meaningful because only active features (e.g. crack growth) are highlighted.

Unfortunately, the AE systems can only qualitatively gauge how much damage is contained in a structure. In order to obtain quantitative results about size, depth and overall acceptability of a part, other NDT methods are necessary. Another drawback of the AE stems from loud service environments which contribute extraneous noise to the signals. For successful applications, signal discrimination and noise reduction are crucial.

#### **4.1.2 History**

Although the acoustic emissions can be created in a controlled environment, they can also occur naturally. Therefore, as means of quality control, the origin of the AE is hard to pinpoint. As early as 6,500 BC, potters were known to listen for audible sounds during the cooling of their ceramics, signifying structural failure. The first documented observations of the AE appear to have been made in the 8<sup>th</sup> century by Arabian alchemist who described audible sounds during forging. Many texts in the late 19<sup>th</sup> century referred to the audible emissions made by material such as tin, iron, cadmium and zinc. Experiments done throughout the mid-1900's culminated in the PhD thesis written by Joseph Kaiser (entitled "Results and Conclusions from Measurement of Sound in Metallic Materials under Tensile Stress"). Kaiser's research is generally recognised as the beginning of modern day acoustic emission testing.

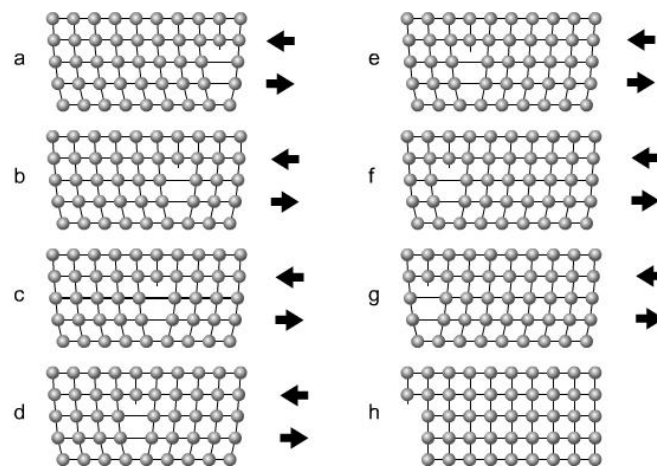
#### **4.1.3 AE sources**

As mentioned in the introduction, the AE can result from the initiation and growth of cracks, slip and dislocation movements, crystal twinning or phase transformations in metals. In any case, acoustic emissions originate with stress. When a stress is exerted on a material, a strain is induced in the material as well (and vice versa). Depending on the magnitude of the stress/strain and the properties of the material, an object may return to its original dimensions

or be permanently deformed after the stress/strain is removed. These two conditions are known as elastic and plastic deformation, respectively.

The most detectible acoustic emissions take place when a loaded material undergoes plastic deformation or when a material is loaded at or near its yield stress. On the microscopic level, as plastic deformation occurs, atomic planes slip past each other through the movement of dislocations (Figure 4-2). These atomic-scale deformations release energy in the form of elastic waves travelling through the object.

When cracks exist, the stress levels present in front of the crack tip can be several times higher than the surrounding area. Therefore, the AE activity will also be observed when the material ahead of the crack tip undergoes plastic deformation (micro-yielding).

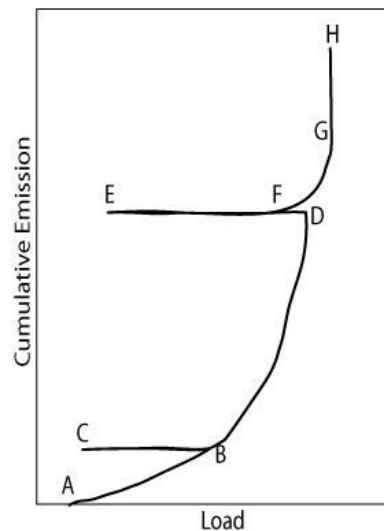


**Figure 4-2 : Example of slip dislocation. Only small force causes dislocation that moves gradually through a crystal grain (a-h). Adopted from [12].**

The amount of energy released by the AE and the amplitude of the waveform are related to the magnitude and velocity of the source event. The amplitude of the emission is proportional to the velocity of crack propagation and the amount of surface area created. Large, discrete crack jumps will produce larger AE signals than cracks that propagate slowly over the same distance.

Detection and conversion of these elastic waves to electrical signals is the basis of the AET. The acoustic emission signals generated under different loading patterns can provide valuable information concerning the structural integrity of a material. Load levels that have been previously exerted on a material do not produce AE activity. In other words, discontinuities created in a material do not expand or move until that former stress is exceeded. This phenomenon, known as Kaiser Effect, can be seen in the load versus AE plot (Figure 4-3). As the object is loaded, acoustic emission events accumulate (segment AB). When the load is removed and reapplied (segment BCB), acoustic emission events do not occur again until the load at point B is exceeded. As the load exerted on the material is increased again (BD),

acoustic emissions are regenerated and stop when the load is removed. However, at point F, the applied load is high enough to cause significant emissions even though the previous maximum load (D) was not reached. This phenomenon is known as the Felicity Effect.



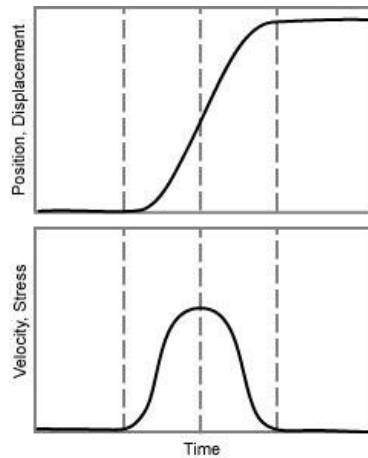
**Figure 4-3 : Basic AE history plot showing Kaiser effect (BCB), Felicity effect (DEF) and emission during hold (GH). Adopted from [10].**

The acoustic emission in concrete specimens under loading by vertical displacement of upper jaw of testing machine was recorded and was used to locate fracture events within specimens. More details about the concrete specimens and the corresponding fracture events locating with help of the AE can be found in the next sections (especially in the section 5, 7 and 8). The sensitivity of an acoustic emission system is often limited by the amount of background noise nearby. Noise in the AET refers to any undesirable signals detected by the sensors. For measurements presented in this thesis, it was necessary to use lower cutting frequency of 3 kHz provided by amplifier AM22 [13] integrated in the experimental set-up that is shown in Figure 4-8. Background noise was caused by testing machine, airborne sound and other low-frequency noises in the testing laboratory.

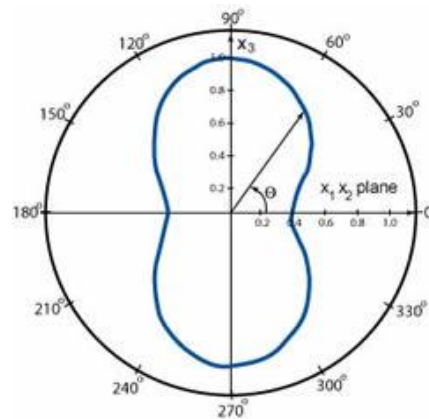
#### 4.1.4 Acoustic waves

A primitive wave released at the AE source is illustrated in Figure 4-4. The displacement waveform is a step-like function corresponding to the permanent change associated with the source process. The analogous velocity and stress waveforms are essentially pulse-like. The width and height of the primitive pulse depend on the dynamics of the source process. Source processes such as microscopic crack jumps and precipitate fractures are usually completed in a fraction of a microsecond ( $1 \times 10^{-6}$  s) or a few microseconds, which explains why the pulse is

short in duration. The amplitude and energy of the primitive pulse vary over an enormous range from submicroscopic dislocation movements to gross crack jumps.



**Figure 4-4 : Primitive AE wave released at a source. Adpoted from [10].**



**Figure 4-5 : Angular dependence of AE radiated from a growing microcrack. Adopted from [10].**

Waves radiates from the source in all direction, often having a strong directionality depending on the nature of the source process, as shown in Figure 4-5. This figure suggests that most of the energy is directed in the 90 and 270° directions, perpendicular to the crack surfaces. The signal that is detected by a sensor is a combination of many parts of the waveform initially emitted. As the AE leaves the source, the waveform travels in a spherically spreading pattern and is reflected off the boundaries of the object. Signals that are in phase with each other as they reach the sensor produce constructive interference which usually results in the highest peak of the waveform being detected. The typical time interval from when the AE wave reflects around the test piece (repeatedly exciting the sensor) until it decays, ranges from the order of 100 microseconds in a highly damped, non-metallic materials to tens of milliseconds ( $1 \times 10^{-3}$  s) in a lightly damped material.

The intensity of an AE signal detected by a sensor is considerably lower that the intensity that would have been observed in the close proximity of the source. This is due to attenuation. There are three main causes of attenuation:

- geometric shape; in plate-like materials, the AE amplitude decays by 30% every time it doubles its distance from the source and in three-dimensional structures, the signal decays by 50%;
- material damping causes that elastic and kinetic energies of the AE wave are absorbed and converted into heat;
- geometric discontinuities (e.g. grain boundaries) and structural boundaries both reflect some of the wave energy that was initially transmitted.

Since source locations are determined by the time required for the wave to travel through the material to a sensor, it is important that the velocity of the propagating waves is accurately determined. For experiments, presented later in this thesis, the velocity of the propagating waves was set to 3925 m/s.

#### 4.1.5 Set-up for the AE measurements

The acoustic emission testing can be performed in the field with portable instruments or in a stationary laboratory setting. Typically, systems contain a sensor(s), a preamplifier, a filter and an amplifier, along with measurement, display and storage equipment (e.g. oscilloscopes, voltmeters and personal computers). AE sensors respond to dynamic motion that is caused by an AE event. This is achieved through transducers which convert mechanical movement into an electrical voltage signal. The transducer element in an AE sensor is almost always a piezoelectric crystal, which is commonly made from a ceramic such as lead zirconate titanate (called PZT). Schematic view of the transducer is shown in Figure 4-6.

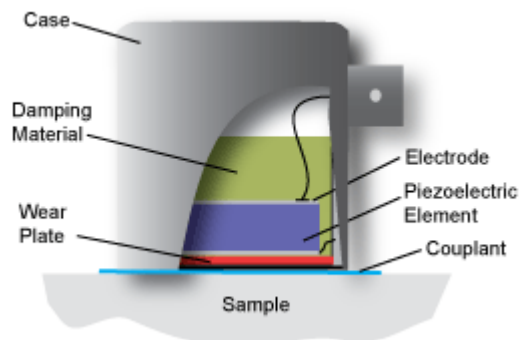


Figure 4-6 : Schematic view of the transducer. Adopted from [10].

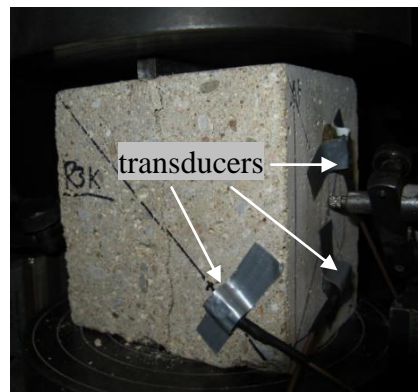


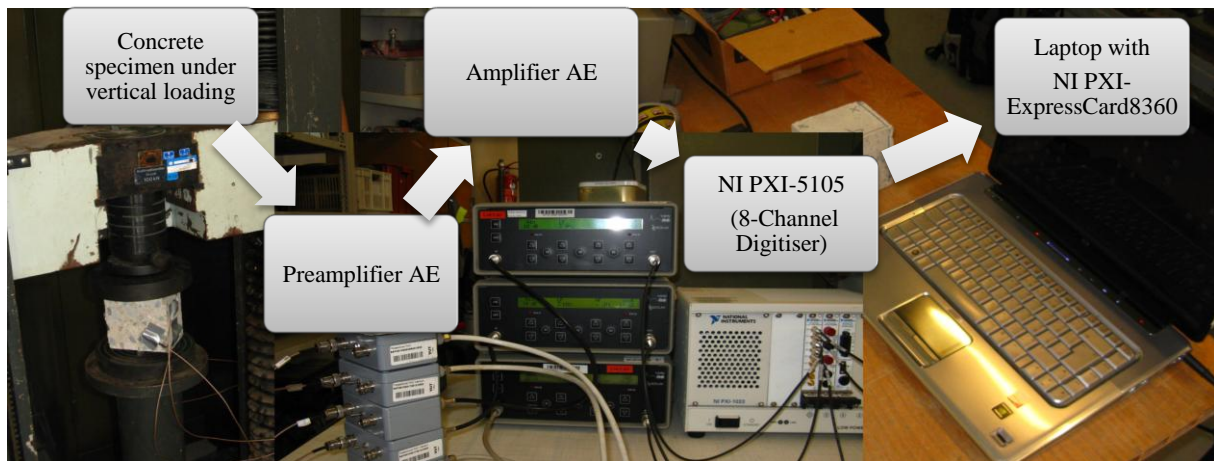
Figure 4-7 : Transducers attached to the surface of the measured concrete block

Transducers (Figure 4-7), used for experiments presented in this thesis, were attached to the concrete surface of specimen with help of beeswax since beeswax provides good mechanical contact between the concrete surface and the transducer and enables easy mounting and removing [14]. Transducers were secured by adhesive tape in order to ensure permanent contact between transducer and beeswax. Experimental set-up used for measurements of the AE is shown in Figure 4-8 which depicts (from the left to the right):

- concrete specimen under test with piezoelectric transducers attached to the surface;
- preamplifier 3S SEDLAK PA31; this preamplifier was chosen for its very low noise and proper bandwidth (20 Hz to 10 MHz [15]);
- amplifier AM22 with lower cutting frequency of 3 kHz and no restrictions of upper frequency [13];

- NI PXI-5105 (8-Channel Digitiser) built in NI PXI-1033 chassis;
- laptop equipped with NI PXI-ExpressCard8630.

Signal is detected by the transducer and send to the preamplifier which boosts the voltage to provide gain and cable drive capability. To minimise interference, a preamplifier is placed close to the transducer. Next, the signal is relayed to the amplifier for elimination of low frequencies (background noise). Following completion of this process, the signal travels to the digitiser that converts signal to a binary code which is sent via NI PXI-ExpressCard8630 to a laptop for analysis and storage. Software LabVIEW developed by National Instruments Corporation (for more information concerning LabVIEW, see manufacturer's website [16]) was used for signal measurement, real-time processing and evaluation [14].



**Figure 4-8 : Experimental set-up for the AE measurements**

Recorded signals are either continuous or burst-type. Each time the threshold voltage is exceeded, the digitiser releases a digital pulse. The first pulse is used to signify the onset of a hit. A hit is used to describe the AE event that is detected by a particular transducer. Pulses will continue to be generated while the signal exceeds the threshold voltage. Once this process has stopped, the hit is finished. The data from the hit is then read into a microcomputer and the onset of hit provided by a particular transducer is used in post-processing for locating of the AE source. Time delays between hits recorded by particular transducers are used to identify position of fracture event within specimen.

Determining the onset of transient signals like AE is very time consuming if the onset is picked manually. Therefore, different approaches based on automatic onset detection algorithms exist. Two approaches, both based on the Akaike Information Criterion (AIC), are presented in this thesis and were used for determination of the AE signal onset. One of the approaches is described in [17] and was led by Joachen H. Kurz, therefore is in this thesis this



approach denoted as KUR method (KUR – are first three letters of Joachen H. Kurz's surname). Another approach described in [18] is denoted as method TWO because it uses two step AIC picker.

## 4.2 Electromagnetic emission

When a structure is subjected to an external stimulation (change in pressure, load or temperature), localised sources trigger the release of energy in the form of electromagnetic field which can be recorded. This phenomenon is denoted as electromagnetic emission (EME). One of the possibilities how to record the formed electromagnetic field is to use a capacitor.

An explanation of the EME origin was related to dislocation phenomena (dislocation is a type of crystallographic defect; one example can be found in Figure 4-2), which however are not able to explain the EME from the fracture in brittle materials where the motion of dislocations can be neglected. The weakness of the "dislocation movement hypothesis" was confirmed in some experiments showing that the EME amplitude increased with the brittleness of the investigated materials.

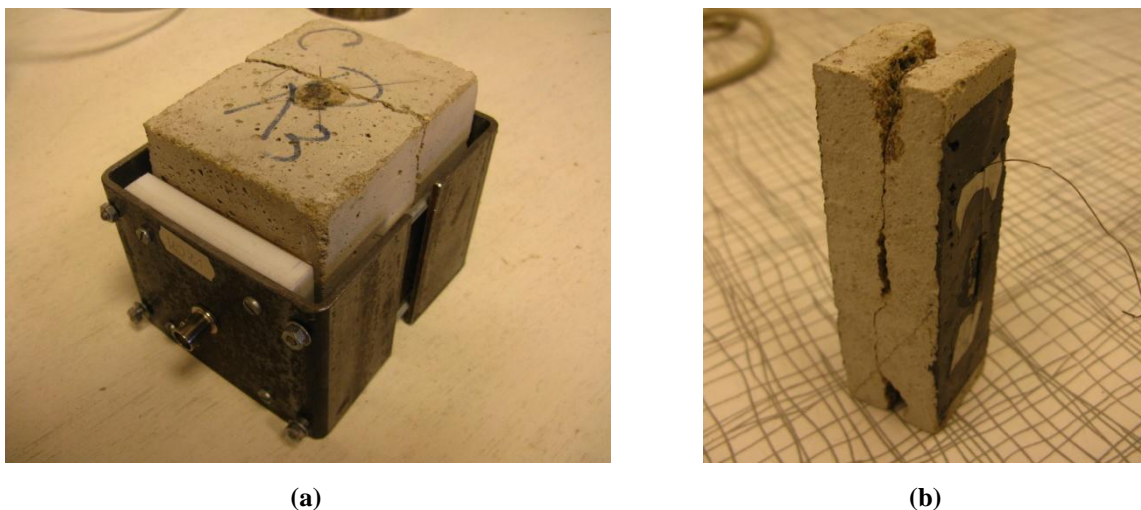
Another EME explanation was initially given in terms of charge separation occurring across the fractures, even if no reasonable explanation is found for each crack face to obtain a net charge [19], where the charge is characteristic of unit of matter that expresses the extent to which it has more or fewer electrons than protons. If an object comprises of many atoms, the net charge is equal to the arithmetic sum, taking polarity into account, of the charges of all the atoms taken together. In a massive sample, this can amount to a considerable quantity of elementary charges. The unit of electrical charge in the International System of Units is coulomb (symbolized C) and 1 C is equal to approximately  $6.24 \times 10^{18}$  elementary charges. It is not unusual for real-world objects to hold charges of many coulombs [20]. More recently, a model preserving the charge neutrality of crack surfaces, where lines of positive ions on both newly created fracture surfaces oscillate around their equilibrium position in opposite phase to the negative ones, was proposed [21].

Regardless the origin of the EME, the electromagnetic field, given by the moving charges, was measured on specimens presented in this thesis. The set-up for measurement of the EME was very similar to the set-up that was used for the AE (see subsection 4.1.5 or Figure 4-8), only the transducers were replaced by plates of capacitor connected to high pass filter with load impedance  $Z_L$  [13]. Two different types of capacitors were used. One was composed of a special adjustable steel bracket with two electrodes, into which the test sample was inserted (Figure 4-9 (a)), and the other was composed of graphite paste applied on the speci-



men surface (Figure 4-9 (b)). In both cases, the dielectric was formed by the concrete specimen. Advantage of steel bracket stems from an improvement of quality of the obtained signal, however, the bracket changes the boundary conditions (bracket is secured by bolts). Graphite paste does not change the boundary conditions, however, the quality of the obtained signal is not very good (due to noise/disturbances by other sources of the electromagnetic field).

Failure of concrete by tensile splitting (most of the failure planes are oriented in the same way as the capacitor plates) is important for the EME measurements because the capacitor plates are capable to record only fracture events (cracks) that are spreading parallel to them. It means that all fracture events spreading perpendicularly to the capacitor plates are not recorded, fracture events spreading parallel to the capacitor plates are entirely recorded and it is not entirely clear what kind of fracture events or how many of them are recorded when the angle between them and capacitor plates lies in interval  $(0^\circ, 90^\circ)$ . It is usually considered, that the signal weakens with cosine of the angle.



**Figure 4-9 : Parallel plate capacitors formed by – (a) adjustable steel bracket, (b) graphite paste**

It is necessary to use an electromagnetic shielding for the EME measurements because the impact of electromagnetic radiation and magnetism negatively affect the recorded EME. The shielding necessitates placing a suitable physical barrier of appropriate material, form and thickness in between the offending source and the designated protected area in order to protect such area from penetration of unwanted signals [22]. Therefore, the testing machine used for experimental recording of combination of acoustic and electromagnetic emission was equipped with the electromagnetic shielding formed of metal box that was enclosing the whole testing machine (Figure 5-9).

## 5 Experimental data

### 5.1 Introduction

As was already noted above the diploma thesis was created in the frame of Czech Science Foundation project GAP104/11/0734 – Utilization of electromagnetic and acoustic emission in research of advanced composite materials for structural applications. The principal investigator of this grant is an employee at the Faculty of Electrical Engineering and Communication Brno University of Technology. He and his research team provided experimental data that are used in this master thesis for comparison with the data obtained from numerical simulations.

### 5.2 Sets of specimens

Loading tests in uniaxial compression were carried out on plain concrete blocks that were grouped into two sets. The set denoted as set One contained two configurations of two specimen shapes: shape A ( $33 \times 99 \times 33$  mm; width  $\times$  breadth  $\times$  height) and shape B ( $50 \times 64 \times 64$  mm). Specimen shape A was tested in two configurations (I and II): I represented loading via direct contact between specimen and jaws of testing machine (Figure 5-1) and II represented loading through two steel prisms with rectangular cross-section ( $6 \times 6$  mm) inserted between the specimen and jaws of testing machine (Figure 5-2). Specimen shape B was available only in the configuration II (Figure 5-3).

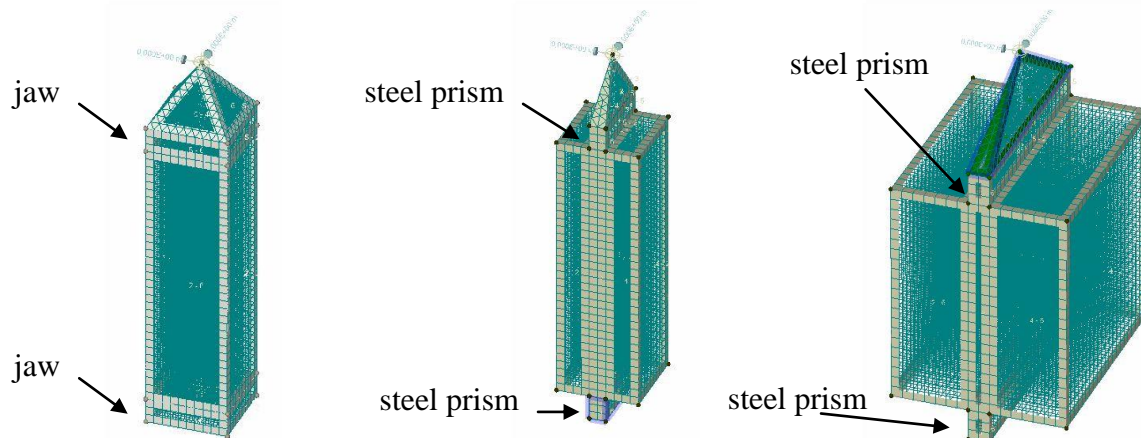


Figure 5-1 : Configuration AI

Figure 5-2 : Configuration AII

Figure 5-3 : Configuration BII

The set denoted as set Two contained three configurations of one specimen shape ( $76 \times 100 \times 100$  mm; width  $\times$  breadth  $\times$  height). Testing configurations were denoted as CC, 1C and 2C: CC represented loading via direct contact between specimen and jaws of testing machine (Figure 5-4), 1C represented loading through one steel prism with rectangular cross-section ( $8 \times 8$  mm) inserted between the specimen and upper jaw of testing machine

(Figure 5-5) and 2C represented loading through two steel prisms with rectangular cross-section ( $8 \times 8$  mm) inserted between the specimen and both jaws of the testing machine (Figure 5-6). Plain concrete blocks belonging to the set Two were extracted from standard beam-shaped testing specimens ( $400 \times 100 \times 100$  mm) as shown in Figure 5-7.

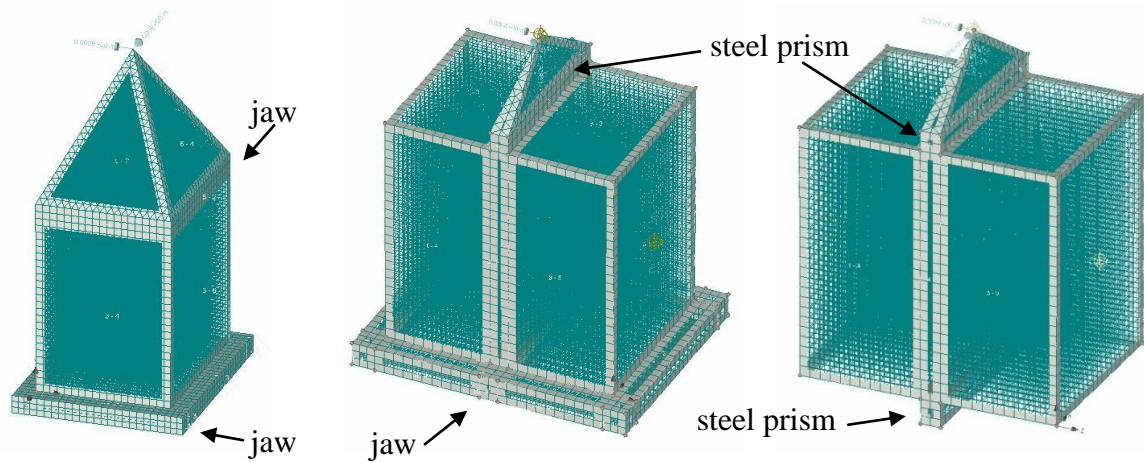


Figure 5-4 : Configuration CC

Figure 5-5 : Configuration 1C

Figure 5-6 : Configuration 2C

Experimental compression tests, during which the acoustic emission was recorded, were conducted on universal material testing machine FPZ-100/1 (Figure 5-8) produced by Heckert (Germany). Material testing machine Fröwag produced by Fröhlich+Wagner GmbH was used for tests where the acoustic and electromagnetic emission were recorded simultaneously because this testing machine was equipped with the electromagnetic shielding formed of metal box that was enclosing the whole testing machine. Shielding is necessary for the EME measurement due to the negative impact of the electromagnetic radiation coming from external sources (e.g. radio frequency).



Figure 5-7 : Sawed standard beam-shaped testing specimen



Figure 5-8 : Material testing machine FPZ-100/1



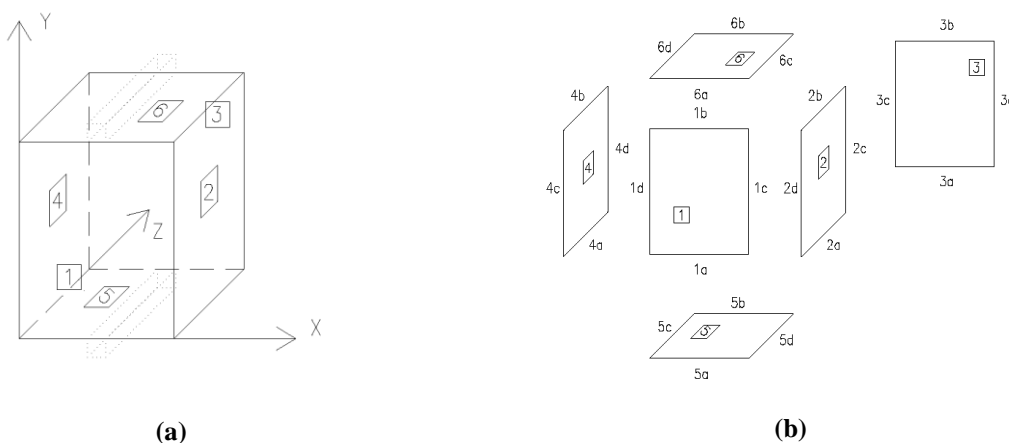
Figure 5-9 : Material testing machine Fröwag

Compressive loading rate of testing machine FPZ-100/1 was set to the lowest possible value of 0.02 mm/min in order to get smooth run of the AE and EME records (too many re-

records at very short period can limit or even restrict locating of fracture events arising in tested specimen).

### 5.3 Parameters of specimens

Dimensions of specimens were stated in the previous section, however the above mentioned dimensions are approximate since the casting of concrete, its shrinkage and subsequent sawing of standard beam-shaped testing specimen bring dimension inaccuracies. Therefore, the specimens were measured prior to all tests by which the author of this thesis assisted. Specimens were precisely measured in order to have precise data for numerical models (even small deviations in models may cause differences in their behaviour). All measured specimens were tabulated and are listed in the Table 5-1 (specimens with two steel prisms) and in the Table 5-2 (specimens with one steel prism) according to the scheme shown in Figure 5-10.



**Figure 5-10 : Scheme of sides and positions of dimensions – (a) Total view, (b) Individual sides**

For easier orientation among the tested concrete blocks, the following nomenclature was used: first two characters were used for type of prescribed concrete mix (R3, R4, R5 or R6, where maximum size of used aggregate is increasing with increasing number behind the letter "R", for detailed information, see Table 5-3) followed by letter that stands for standard beam-shaped testing specimen (set C, I or K, specifying position of specimen during concrete casting) separated by the underscore "\_" with appended roman numeral (I, II, III, IV or V, identifying position on the standard beam-shaped testing specimen before extraction of individual block; Figure 5-7 shows the roman numerals written on specimens) once more separated by the underscore "\_" followed by two characters representing boundary conditions (1C for loading through one steel prism, shown in Figure 5-5, and 2C for loading through two steel prisms, shown in Figure 5-6). Roman numeral was used only for blocks with known position on the standard beam-shaped testing specimen before extraction of individual block.

**Table 5-1 : Dimensions of specimens with 2 steel prisms**

Specimen	Specimen dimensions [mm]											
	Side and position											
Specimen	1a	1b	1c	1d	2a	2b	2c	2d	3a	3b	3c	3d
<b>R3I_2C</b>	75.76	75.78	100.20	100.25	102.08	102.10	100.17	100.31	75.58	75.54	100.15	100.29
<b>R4I_2C</b>	76.80	76.80	100.80	100.80	97.50	97.50	99.77	100.50	76.60	76.60	99.80	99.80
<b>R5I_2C</b>	75.15	75.15	100.14	100.30	99.10	100.70	99.40	100.15	75.50	75.40	99.50	99.50
<b>R6I_2C</b>	76.50	76.50	100.50	100.50	99.60	99.60	99.90	100.90	76.00	76.00	99.60	99.60
Specimen	4a	4b	4c	4d	5a	5b	5c	5d	6a	6b	6c	6d
<b>R3I_2C</b>	102.60	102.23	100.16	100.03	76.00	76.00	102.00	102.00	75.60	75.60	102.51	101.50
<b>R4I_2C</b>	97.50	97.50	99.80	100.30	76.90	76.60	99.90	99.90	76.70	76.80	96.80	97.20
<b>R5I_2C</b>	99.80	101.15	99.50	100.15	75.70	75.70	99.70	99.70	75.40	75.70	101.40	101.40
<b>R6I_2C</b>	99.40	99.90	99.60	100.50	76.00	76.50	99.40	99.50	76.00	76.00	99.80	100.20
Specimen	Mean value [mm]			Standard deviation [mm]			Coefficient of variation [%]			Chosen value for numerical model [mm]		
	Axis			Axis			Axis			Axis		
	x	y	z	x	y	z	x	y	z	x	y	z
<b>R3I_2C</b>	75.73	100.20	102.13	0.15	0.07	0.24	0.2	0.1	0.2	<b>76</b>	<b>100</b>	<b>102</b>
<b>R4I_2C</b>	76.73	100.20	97.98	0.10	0.40	0.96	0.1	0.4	1.0	<b>77</b>	<b>100</b>	<b>98</b>
<b>R5I_2C</b>	75.46	99.83	100.37	0.19	0.36	0.79	0.2	0.4	0.8	<b>76</b>	<b>100</b>	<b>100</b>
<b>R6I_2C</b>	76.19	100.14	99.68	0.23	0.46	0.22	0.3	0.5	0.2	<b>76</b>	<b>100</b>	<b>100</b>

**Table 5-2 : Dimensions of specimens with 1 steel prism**

Specimen	Specimen dimensions [mm]											
	Side and position											
Specimen	1a	1b	1c	1d	2a	2b	2c	2d	3a	3b	3c	3d
<b>R3K_II_1C</b>	77.01	76.92	100.50	100.43	98.72	98.75	99.68	100.41	76.45	76.53	99.56	99.61
<b>R3K_IV_1C</b>	77.14	77.26	100.40	100.69	100.61	100.91	100.66	99.91	77.14	76.97	99.95	100.20
<b>R3K_V_1C</b>	78.69	78.63	100.75	100.64	101.01	101.25	100.00	100.60	80.00	79.86	99.96	99.97
<b>R4K_II_1C</b>	76.00	76.03	100.69	100.62	99.82	100.43	100.49	100.64	75.56	76.00	100.02	99.94
Specimen	4a	4b	4c	4d	5a	5b	5c	5d	6a	6b	6c	6d
<b>R3K_II_1C</b>	99.20	98.80	100.40	99.74	76.56	76.97	98.36	98.21	77.44	76.62	98.60	98.74
<b>R3K_IV_1C</b>	100.61	100.31	100.40	99.89	77.89	76.97	100.34	100.61	77.17	77.13	100.85	100.47
<b>R3K_V_1C</b>	101.35	100.88	100.44	99.76	80.20	79.76	101.15	100.83	78.48	79.80	101.58	100.67
<b>R4K_II_1C</b>	100.01	100.78	100.44	99.84	75.57	75.95	100.31	99.99	76.00	76.01	100.41	100.77
Specimen	Mean value [mm]			Standard deviation [mm]			Coefficient of variation [%]			Chosen value for numerical model [mm]		
	Axis			Axis			Axis			Axis		
	x	y	z	x	y	z	x	y	z	x	y	z
<b>R3K_II_1C</b>	76.81	100.04	98.67	0.27	0.39	0.21	0.4	0.4	0.2	<b>77</b>	<b>100</b>	<b>99</b>
<b>R3K_IV_1C</b>	77.21	100.26	100.59	0.18	0.28	0.16	0.2	0.3	0.2	<b>77</b>	<b>100</b>	<b>100</b>
<b>R3K_V_1C</b>	79.43	100.27	101.09	0.62	0.34	0.24	0.8	0.3	0.2	<b>79</b>	<b>100</b>	<b>101</b>
<b>R4K_II_1C</b>	75.89	100.34	100.32	0.16	0.30	0.28	0.2	0.3	0.3	<b>76</b>	<b>100</b>	<b>100</b>

As an illustration, R3I\_2C denotes specimen with finest aggregate size, standard beam-shaped testing set I without known position on the standard beam-shaped testing specimen before extraction of individual block and loading through two steel prisms. Similarly R3K\_IV\_1C denotes specimen with finest aggregate size, standard beam-shaped testing set K with known position on the standard beam-shaped testing specimen, before extraction of individual block, with value of IV (i.e. fourth block on the specimen counted from the left as shown in Figure 5-7) and loading through one steel prism.

**Table 5-3 : Aggregate size of concrete mix**

Concrete mix	R3	R4	R5	R6
Size of aggregate	0–4 mm	0–8 mm	0–16 mm	0–22 mm

Measured dimensions of specimens in Table 5-1 and Table 5-2 are tabulated according to the scheme shown in Figure 5-10 where the origin of coordinate system was placed in one corner of the specimen and the side lying in the  $x$ - $y$  plane was denoted as side 1, the side lying in  $x$ - $z$  plane was marked as side 5 and so on according to Figure 5-10 (a). Each side was measured four times, two times the width and two times the height denoted as  $a$ ,  $b$  and  $c$ ,  $d$ , respectively (Figure 5-10 (b)). Specimen dimension for each axis direction was measured eight times in total (e.g. width of specimen in the  $x$  direction was measured as 1a, 1b, 3a, 3b, 5a, 5b, 6a and 6b) and therefore, in order to get single value for each axis direction, mean value was calculated according to the Equation 5.1.

$$A_m = \frac{1}{8} \sum_{i=1}^8 a_i \quad (5.1)$$

where  $A_m$  is the mean value and  $a_i$  is width/height of specimen side (e.g. 1a, 1b, 3a and so on). In order to see how the measured dimensions vary, the standard deviation was calculated according to the Equation 5.2.

$$D = \frac{1}{8} \sum_{i=1}^8 |a_i - m(X)| \quad (5.2)$$

where  $a_i$  denotes width/height of specimen side,  $D$  denotes standard deviation and  $m(X)$  represents mean measure of central tendency. Dimensions for numerical models were chosen on the basis of values calculated by Equation 5.1 and 5.2.

The specific material weight of specimens was determined and is listed in Table 5-4. Specimens were weighted and the specimens' material weight was calculated according to the precise dimensions listed in the Table 5-1 and Table 5-2. Calculation procedure is described by the equation below.

$$\gamma = \rho g ; \rho = \frac{m}{V} \quad (5.3)$$



where  $\gamma$  denotes the specific material weight,  $\rho$  is the density of the material,  $g$  is acceleration due to gravity (considered in this thesis as  $10 \text{ m/s}^2$ ),  $m$  is mass and  $V$  is volume of specimen calculated as product of mean values in the  $x$ ,  $y$  and  $z$  direction (obtained from Table 5-1 and Table 5-2).

**Table 5-4 : Specimen specific material weight**

Specimen	Mass	Specific material weight		Specimen	Mass	Specific material weight	
	[kg]	[kg/m <sup>3</sup> ]	[MN/m <sup>3</sup> ]		[kg]	[kg/m <sup>3</sup> ]	[MN/m <sup>3</sup> ]
<b>R3I_2C</b>	1.548	1998	1.998E-02	<b>R3K_II_1C</b>	1.527	2014	2.014E-02
<b>R4I_2C</b>	1.591	2112	2.112E-02	<b>R3K_IV_1C</b>	1.562	2006	2.006E-02
<b>R5I_2C</b>	1.649	2181	2.181E-02	<b>R3K_V_1C</b>	1.623	2016	2.016E-02
<b>R6I_2C</b>	1.681	2211	2.211E-02	<b>R4K_II_1C</b>	1.630	2134	2.134E-02

Strength class of the tested concrete was designed as C20/25 but, as from the experiments follows, the grade of concrete was slightly lower. Conducted tests described in the next two subsections determine relevant mechanical parameters of concrete specimens that are compared with parameters listed in the Eurocode 2 [23].

## 5.4 Compression tests of specimens

Compression tests for all concrete mixes used in this thesis were performed in order to determine compressive strength of specimens ( $f_c$ ; according to ČSN EN 12390-3 [24]) and static modulus of elasticity in compression ( $E_c$ ; according to ČSN ISO 6784 [25]). Dimensions and masses of specimens, maximal imposed load and determined parameters are listed in Table 5-5.

**Table 5-5 : Compression tests of specimens**

	$a$	$b$	$h$	$m$	$F_{\max}$	$f_c$	$E_c$
Concrete mix	[mm]	[mm]	[mm]	[g]	[kN]	[MPa]	[GPa]
<b>R3</b>	76.67	103.90	100.23	1610.10	88.40	11.1	4.34
<b>R4</b>	77.65	97.58	100.09	1612.40	211.07	27.9	8.13
<b>R5</b>	77.72	97.90	100.01	1674.90	257.47	33.8	9.44
<b>R6</b>	76.69	98.27	100.17	1671.60	234.73	31.1	11.66

## 5.5 Ultrasonic pulse velocity method

Ultrasonic pulse velocity method is a truly non-destructive method that enables to set material grade of tested material and its physiomechanical characteristics. The method is based on repetitive transmission of ultrasonic pulses through the tested material and detects propagation speed of ultrasonic waves. This velocity varies with material and changes with its properties. For instance ultrasonic wave pulse velocity in high quality concrete is higher than in the one

with lower quality. To clarify this statement, the ultrasonic wave pulse velocity is partially matter of convention because the pulse path length is not precisely known [26].



Figure 5-11 : Proceq TICO - Ultrasonic testing instrument



Figure 5-12 : Transducers and specimen R3K\_V

TICO Ultrasonic Testing Instrument (Figure 5-11) produced by company Proceq, that invented the original Schmidt concrete test hammer [27], was used for measurements. Proceq describes TICO, in its catalogue [28], as an instrument that determines, indirectly, the modulus of elasticity and concrete strength. The instrument is typically used on site to assess uniformity of concrete and to locate cracks, voids, cavities and defects due to fire and frost. The TICO instrument uses transducers as transmitters and receivers to calculate pulse velocity by measuring transmission time. Two concrete blocks belonging to the set Two (for more information concerning sets, see subsection 5.2) were used for transmission time measurements.

Table 5-6 : Specimens parameters for ultrasonic test

Specimen	Dimensions			Mass	Specific material weight	Passing time of ultrasound			Average propagation speed
	$b$ [mm]	$h$ [mm]	$L$ [mm]	$m$ [g]	$\rho$ [kg/m <sup>3</sup> ]	$t_{L1}$ [μs]	$t_{L2}$ [μs]	$t_{L3}$ [μs]	$v_L$ [m/s]
R3K_V-x	101.1	100.3	79.4	1 623.0	2 016	27.0	26.9	27.2	2 938
R3K_V-z	79.4	100.3	101.1	1 623.0	2 016	34.6	34.0	34.0	2 956
R4K_V-x	98.0	100.0	81.0	1 630.0	2 053	22.7	24.0	23.0	3 488
R4K_V-z	81.0	100.0	98.0	1 630.0	2 053	28.4	29.6	30.3	3 332
Specimen	Dynamic modulus of elasticity in tension and compression			Informative concrete compressive strength		Size criterion			Size coefficient
	$E_{bu} = \rho \cdot v_L^2 \cdot k^2 \cdot 10^{-6}$ [GPa]			$R_{be} = 9.9 \cdot v_{L3}^2 - 56 \cdot v_{L3} + 87.8$ [MPa]		wave length $\lambda_L = v_L / f_u$ [m]	$0.2 \cdot \lambda_L$ [m]	$2 \cdot \lambda_L$ [m]	$k$ [-]
R3K_V-x	14.8			8.7		0.0196	0.0039	0.0392	1.0857
R3K_V-z	14.9			8.8		0.0197	0.0039	0.0394	1.0857
R4K_V-x	21.2			12.9		0.0233	0.0047	0.0465	1.0857
R4K_V-z	19.3			11.1		0.0222	0.0044	0.0444	1.0857



The calibration of TICO instrument has to be performed before every measurement. Calibration rod is essential part of the instrument set and its calibration value is well known and therefore marked on the rod [29]. The transducers are pressed against the rod and, after 5 seconds, the calibration value is automatically stored. Transmission time measurements were performed on R3K\_V and R4K\_V specimens and the recorded values were tabulated in Table 5-6. Transmission times were measured on specimens for two axis directions (denoted in Table 5-6 as "-x", representing ultrasound propagation along  $x$ -axis and as "-z" for propagation along  $z$ -axis; orientation of axes is depicted in Figure 5-10 (a)). Instructions for transmission time measurement can be found in paper [30] and the transducers together with tested specimen are shown in Figure 5-12. Table 5-6 includes all necessary formulae for calculation of dynamic modulus of elasticity in tension and compression (according to ČSN 73 1371 [31]; for more information concerning used formulae, see this standard) and for calculation of informative concrete compressive strength (according to ČSN 73 2011 [32]; for more information concerning used formulae, see this standard).

Eurocode 2 includes table with strength and deformation characteristics for concrete. Part of this table was extracted and can be found in Table 5-7 which additionally shows the design values for concrete strength classes from C12/15 to C35/45. The value of design compressive strength is defined as:

$$f_{cd} = \frac{\alpha_{cc} f_{ck}}{\gamma_C} \quad (5.4)$$

where  $f_{cd}$  is design compressive strength,  $\alpha_{cc}$  is the coefficient taking account of long term effects on the compressive strength ( $\alpha_{cc} = 1.0$ ),  $f_{ck}$  is the characteristic compressive cylinder strength of concrete at 28 days and  $\gamma_C$  is partial safety factor for concrete ( $\gamma_C = 1.5$ )

**Table 5-7 : Strength classes for concrete C12/15 to C35/45**

Strength class	C12/15	C16/20	C20/25	C25/30	C30/37	C35/45
$f_{ck}$ [MPa]	12	16	20	25	30	35
$f_{ck,cube}$ [MPa]	15	20	25	30	37	45
$E_{cm}$ [GPa]	20	24	28	33	38	43
$f_{cd}$ [MPa]	8	10.7	13.3	16.7	20	23.3

Comparing values listed for concrete C20/25 in Table 5-7 with corresponding values in Table 5-5 and Table 5-6 it can be concluded that the compressive strength of concrete specimens is lower than the value listed in Eurocode only for R3 concrete mix. On the other hand, the modulus of elasticity is significantly lower for all tested specimens than the Eurocode presents (lower about two to almost seven times) and therefore special attention should be taken during determination of parameters for material models of numerical simulations.

## **6 Computational software ATENA – Program description and theoretical background**

### **6.1 Introduction**

ATENA is a new generation of the computer program SBETA, offered by Cervenka Consulting Ltd., with integrated pre- post-processing and finite element solution. The Name ATENA is an abbreviation for Advanced Tool for Engineering Nonlinear Analysis [33].

### **6.2 Program description**

The ATENA program, which is determined for nonlinear finite element analysis of structures, offers tools specially designed for computer simulation of concrete and reinforced concrete structure behaviour. ATENA program consists of the solution core and several user interfaces. The solution core offers capabilities for both the 2D and 3D analysis of continuum structures. It has libraries of finite elements, material models and solution methods.

ATENA User Graphic Interface for 2D is a program, which enables access to the ATENA solution core. It is limited to 2D graphical modelling and covers the states of plane stress, plane strain, and rotational symmetry [34].

ATENA User Graphic Interface for 3D is a program, which also enables access to the ATENA solution core. It offers capabilities for variety of structural analysis tasks, such as: stress and failure analysis, transport of heat and humidity, time dependent problems (creep, dynamics) and their interactions. Solution core offers a wide range of 2D and 3D continuum models, libraries of finite elements, material models and solution methods [35].

ATENA program has three main functions:

1. Pre-processing. Input of geometrical objects (concrete, reinforcement, interfaces, etc.), loading and boundary conditions, meshing and solution parameters.
2. Analysis. It makes possible a real time monitoring of results during calculations.
3. Post-processing. Access to a wide range of graphical and numerical results.

### **6.3 Two-dimensional elasticity**

Many problems in elasticity may be treated satisfactorily by a two-dimensional or plane theory of elasticity. There are two general types of problems involved in this plane analysis, plane stress and plane strain. These two types will be defined by setting down certain restrictions and assumptions on the stress and displacement fields. They will also be introduced descriptively in terms of their physical prototypes.

Paper [36] describes the two-dimensional state of stress, illustrated in Figure 6-1, where  $\sigma_x$  and  $\sigma_y$  are normal stresses and  $\tau_{xy}$  and  $\tau_{yx}$  are the shear stresses. Stresses  $\sigma_x$ ,  $\sigma_y$  and  $\tau_{xy}$  are independent and can be written as:

$$\{\sigma\} = \begin{Bmatrix} \sigma_x \\ \sigma_y \\ \tau_{xy} \end{Bmatrix} \quad (6.1)$$

From these stresses the maximum and minimum normal stresses, the principal stresses, in the two-dimensional plane are:

$$\sigma_1 = \frac{\sigma_x + \sigma_y}{2} + \sqrt{\left(\frac{\sigma_x - \sigma_y}{2}\right)^2 + \tau_{xy}^2} = \sigma_{max} \quad (6.2)$$

$$\sigma_2 = \frac{\sigma_x + \sigma_y}{2} - \sqrt{\left(\frac{\sigma_x - \sigma_y}{2}\right)^2 + \tau_{xy}^2} = \sigma_{min} \quad (6.3)$$

and the principle angle is

$$\tan 2\theta_p = \frac{2\tau_{xy}}{\sigma_x - \sigma_y} \quad (6.4)$$

The principal stresses and their directions are shown in the Figure 6-2.

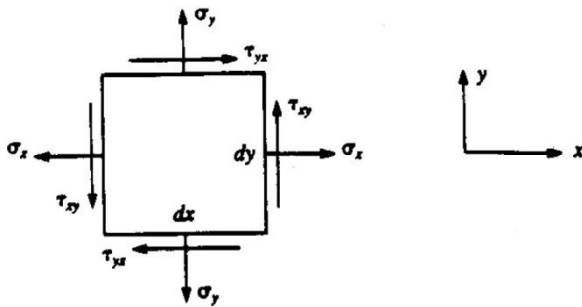


Figure 6-1 : Two-dimensional state of stress. Adopted from [36].

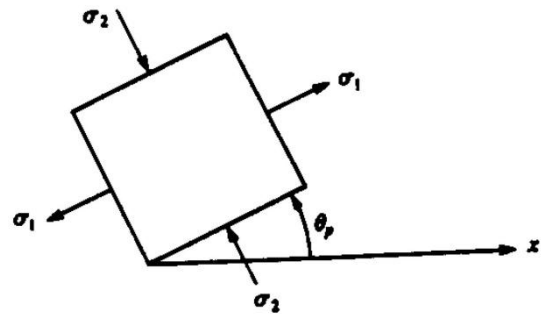


Figure 6-2 : Principal stresses and their directions. Adopted from [36].

The general two-dimensional state of strain at some point in a structure is represented by the infinitesimal element (Figure 6-3),  $dx dy$ , where  $u$  and  $v$  are the displacement in the  $x$  and  $y$  direction at point A, respectively, and lines AC and AB have been extended and displaced.

The normal or (ex-tensional or longitudinal) strains are, under the assumption of small deformations, defined as:

$$\varepsilon_x = \frac{\partial u}{\partial x}; \quad \varepsilon_y = \frac{\partial v}{\partial y} \quad (6.5)$$

and the shear strain is:

$$\gamma_{xy} = \frac{\partial u}{\partial y} + \frac{\partial v}{\partial x} \quad (6.6)$$

These can be written as the strain vector:

$$\{\varepsilon\} = \begin{Bmatrix} \varepsilon_x \\ \varepsilon_y \\ \gamma_{xy} \end{Bmatrix} \quad (6.7)$$

The basic partial differential equations for plane elasticity including body and inertia forces are:

$$\frac{\partial \sigma_x}{\partial x} + \frac{\partial \sigma_{xy}}{\partial y} + X = \rho \frac{\partial^2 u}{\partial t^2} \quad (6.8)$$

$$\frac{\partial \sigma_{yx}}{\partial x} + \frac{\partial \sigma_y}{\partial y} + Y = \rho \frac{\partial^2 v}{\partial t^2} \quad (6.9)$$

where  $X$  and  $Y$  denote the body forces per unit volume in the  $x$  and  $y$  directions, respectively, and  $\rho$  is the density of the material and  $t$  is time.

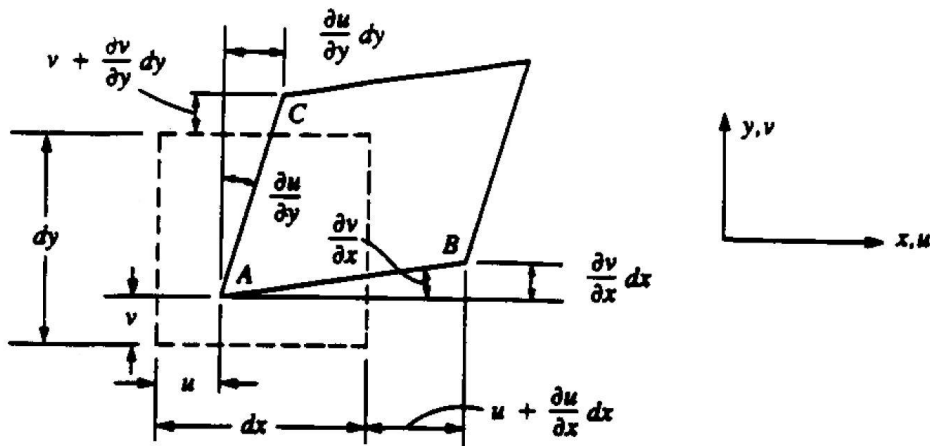


Figure 6-3 : Infinitesimal element at a point of the structure. Adopted from [36].

### 6.3.1 Plane stress

Plane stress is defined to be a state of stress in which the normal stress,  $\sigma_z$ , and the shear stresses,  $\sigma_{xz}$  and  $\sigma_{yz}$ , directed perpendicular to the  $x$ - $y$  plane are assumed to be zero.

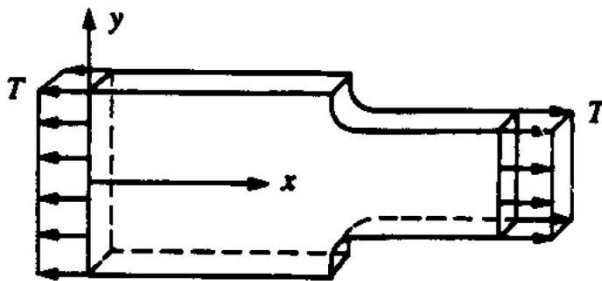


Figure 6-4 : Plate with fillet. Adopted from [36].

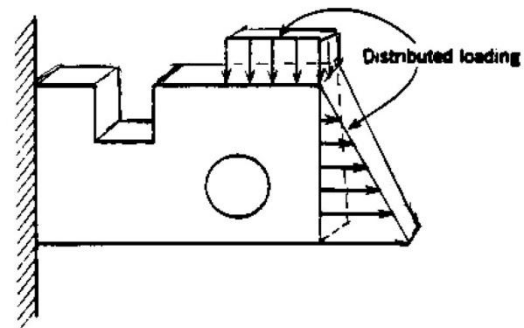


Figure 6-5 : Plate with hole. Adopted from [36].

The geometry of the body is essentially that of a plate with one dimension much smaller than the others. The loads are applied uniformly over the thickness of the plate and act

in the plane of the plate (Figure 6-4 and Figure 6-5). The plane stress condition is the simplest form of behaviour for continuum structures and represents situations frequently encountered in practice.

Typical loading and boundary conditions for plane stress problems in two-dimensional elasticity:

- a) Loadings may be point forces or distributed forces applied over the thickness of the plate.
- b) Supports may be fixed points or fixed edges or roller supports.

For isotropic materials (e.g. uncracked concrete) and assuming:

$$\sigma_z = \tau_{xz} = \tau_{yz} = 0 \quad (6.10)$$

and

$$\gamma_{xz} = \gamma_{yz} = 0 \quad (6.11)$$

yields

$$\{\sigma\} = [D] \{\varepsilon\} \quad (6.12)$$

where

$$[D] = \frac{E}{1-\nu^2} \begin{bmatrix} 1 & \nu & 0 \\ \nu & 1 & 0 \\ 0 & 0 & \frac{1-\nu^2}{2} \end{bmatrix} \quad (6.13)$$

in which [D] is the stiffness (stress/strain) matrix (or constitutive matrix),  $E$  is the modulus of elasticity and  $\nu$  is Poisson's ratio.

The strains in plane stress then are

$$\{\varepsilon\} = [C] \{\sigma\} \quad (6.14)$$

or

$$\begin{Bmatrix} \varepsilon_x \\ \varepsilon_y \\ \gamma_{xy} \end{Bmatrix} = \frac{1}{E} \begin{bmatrix} 1 & -\nu & 0 \\ -\nu & 1 & 0 \\ 0 & 0 & 2(1+\nu) \end{bmatrix} \begin{Bmatrix} \sigma_x \\ \sigma_y \\ \sigma_{xy} \end{Bmatrix} \quad (6.15)$$

where  $[C]^{-1} = [D]$ . Also

$$\varepsilon_y = \frac{1}{E} (-\nu)(\sigma_x + \sigma_y) \quad (6.16)$$

### 6.3.2 Plane strain

Plane strain is defined to be a state of strain in which the strain normal to the x-y plane,  $\varepsilon_z$ , and the shear strain  $\gamma_{xz}$  and  $\gamma_{yz}$ , are assumed to be zero.

In plane strain, one deals with a situation in which the dimension of the structure in which the dimension of the structure in one direction, say the z-coordinate direction, is very large in comparison with the dimensions of the structure in the other two directions (x and y coordinate axes), the geometry of the body is essentially that of a prismatic cylinder with one dimension much larger than the others. The applied forces act in the x-y plane and do not vary in the z direction, i.e. the loads are uniformly distributed with respect to the large dimension and act perpendicular to it. Some important practical applications of this representation occur in the analysis of dams, tunnels, and other geotechnical works. Also such small-scale problems as bars and rollers compressed by forces normal to their cross section are amenable to analysis in this way.

For isotropic materials (e.g. uncracked concrete) and assuming:

$$\varepsilon_z = \gamma_{xz} = \gamma_{yz} = 0 \quad (6.17)$$

and

$$\tau_{xz} = \tau_{yz} = 0 \quad (6.18)$$

yields

$$\{\sigma\} = [D] \{\varepsilon\} \quad (6.19)$$

where

$$[D] = \frac{E}{(1+\nu)(1-2\nu)} \begin{bmatrix} 1-\nu & \nu & 0 \\ \nu & 1-\nu & 0 \\ 0 & 0 & \frac{1-2\nu}{2} \end{bmatrix} \quad (6.20)$$

with

$$\sigma_z = \frac{E}{1+\nu} \left[ \frac{\nu}{1-2\nu} (\varepsilon_x + \varepsilon_y) \right] \quad (6.21)$$

It is worth pointing out that the SBeta material model used in ATENA 2D is modelled in the state of plane stress and that the 3D Non Linear Cementitious 2 material model is modelled in 2D space either in the state of plane stress or in the state of plane strain. For more information concerning both material models, see the subsection 6.5.

## 6.4 Three-dimensional elasticity

Multi-axial stress and strain states of the linearity between stress and strain can be written as:

$$\{\sigma\} = [D]\{\varepsilon\} \quad (6.22)$$

where

$$\{\sigma\} = \begin{Bmatrix} \sigma_x \\ \sigma_y \\ \sigma_z \\ \tau_{xy} \\ \tau_{yz} \\ \tau_{zx} \end{Bmatrix}, \{\varepsilon\} = \begin{Bmatrix} \varepsilon_x \\ \varepsilon_y \\ \varepsilon_z \\ \gamma_{xy} \\ \gamma_{yz} \\ \gamma_{zx} \end{Bmatrix}, [D] = \begin{bmatrix} D_{11} & D_{12} & \dots & D_{16} \\ D_{21} & D_{22} & \dots & D_{26} \\ \vdots & \vdots & \ddots & \vdots \\ D_{61} & D_{62} & \dots & D_{66} \end{bmatrix} \quad (6.23)$$

The strain-stress relations for an isotropic material are:

- Normal strains

$$\varepsilon_x = +\frac{\sigma_x}{E} - \nu \frac{\sigma_y}{E} - \nu \frac{\sigma_z}{E} \quad (6.24)$$

$$\varepsilon_y = -\nu \frac{\sigma_x}{E} + \frac{\sigma_y}{E} - \nu \frac{\sigma_z}{E} \quad (6.25)$$

$$\varepsilon_z = -\nu \frac{\sigma_x}{E} - \nu \frac{\sigma_y}{E} + \frac{\sigma_z}{E} \quad (6.26)$$

- Shear strains

$$\gamma_{xy} = \frac{1}{G} \tau_{xy}, \gamma_{yz} = \frac{1}{G} \tau_{yz}, \gamma_{zx} = \frac{1}{G} \tau_{zx} \quad (6.27)$$

where  $\nu$  is the Poisson's ratio and the shear modulus  $G$  is defined by [37]:

$$G = \frac{E}{2(1+\nu)} \quad (6.28)$$

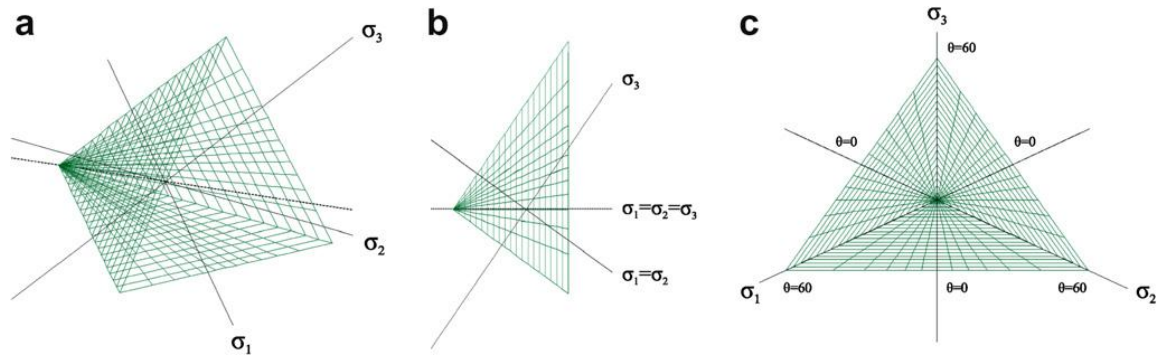
## 6.5 Material model

For simulations was chosen the 3D Non Linear Cementitious 2 material model because, as already follows from its name, it can be used in ATENA 3D as well. This allows proper comparison between 2D and 3D simulations and that is the reason why the SBeta material model, recommended in [34] for 2D concrete, was used only for parametric studies described later in the text. Subsection 6.5, 6.6 and 6.7 presents selected parts of ATENA Theory manual [38].

### 6.5.1 3D Non Linear Cementitious 2

The 3D Non Linear Cementitious 2 material model is described in [38] as fracture-plastic model that combines constitutive models for tensile (fracturing) and compressive (plastic) behaviour (Equation 6.29). The fracture model is based on the classical orthotropic smeared crack formulation and crack band model. It employs Rankine failure criterion (Equation 6.31; Figure 6-6), exponential softening, and it can be used as rotated or fixed crack model. The hardening/softening plasticity model is based on Menétrey-William failure surface (Figure 6-7). The model uses return mapping algorithm for the integration of constitutive equations. Special attention is given to the algorithm for the combination of the two models (Figure 6-8). The combined algorithm is based on a recursive substitution, and it allows for the two models to be developed and formulated separately. The algorithm can handle cases when failure surfaces of both models are active, but also when physical changes such as crack closure occur. The model can be used to simulate concrete cracking, crushing under high confinement, and

crack closure due to crushing in other material directions. The functionality of 3D models in 2D (plane stress, plane strain, axial symmetry) is automatically provided by the program.



**Figure 6-6 : Rankine failure surface represented in Haigh-Westergaard coordinates – (a) 3D failure surface, (b) Rendulic plane (meridians) and (c) deviatoric plane (deviatoric section). Adopted from [39].**

The material model formulation is based on the strain decomposition into elastic  $\varepsilon_{ij}^e$ , plastic  $\varepsilon_{ij}^p$  and fracturing  $\varepsilon_{ij}^f$  components

$$\varepsilon_{ij} = \varepsilon_{ij}^e + \varepsilon_{ij}^p + \varepsilon_{ij}^f \quad (6.29)$$

The new stress state is then computed by the formula:

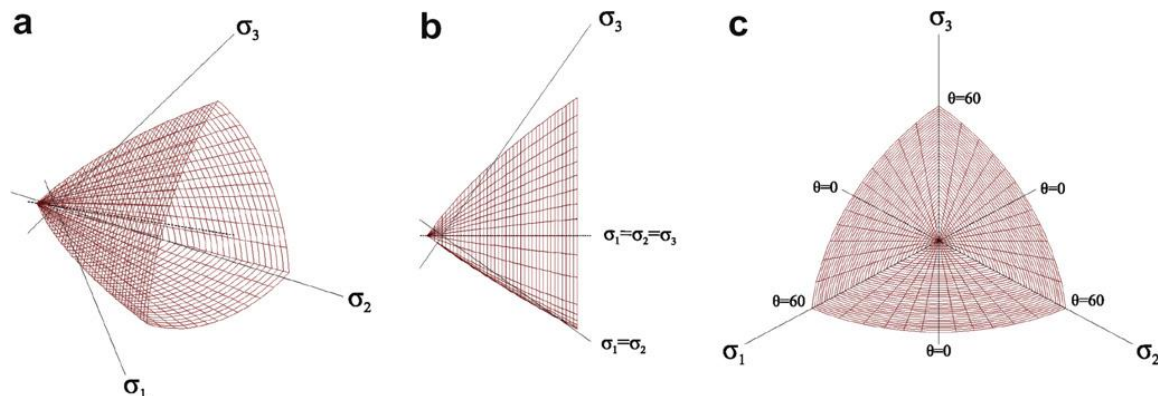
$$\sigma_{ij}^n = \sigma_{ij}^{n-1} + E_{ijkl}(\Delta\varepsilon_{kl} - \Delta\varepsilon_{kl}^p - \Delta\varepsilon_{kl}^f) \quad (6.30)$$

where the increments of plastic strain  $\Delta\varepsilon_{ij}^p$  and fracturing strain  $\Delta\varepsilon_{ij}^f$  must be evaluated based on the used material models.

Rankine criterion is used for concrete cracking

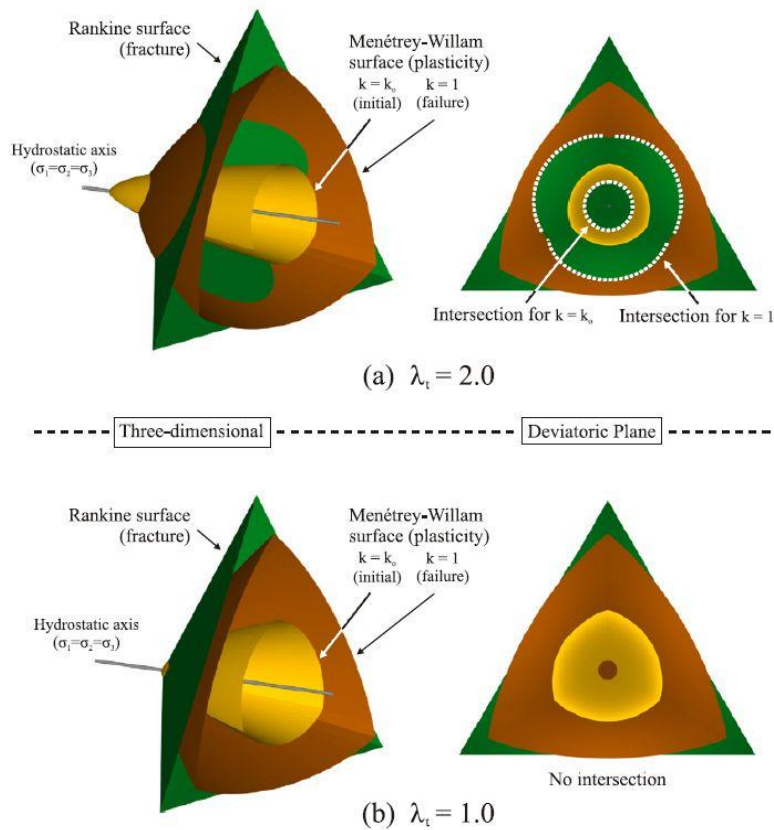
$$F_i^f = \sigma_{ii}^t - f_{ti}^t \leq 0 \quad (6.31)$$

It is assumed that strains and stresses are converted into the material directions, which in the case of rotated crack model correspond to the principal directions and in the case of fixed crack model are given by the principal directions at the onset of cracking. Therefore,  $\sigma_{ii}^t$  identifies the trial stress and  $f_{ti}^t$  tensile strength in the material direction  $i$ . Prime symbol denotes quantities in the material directions.



**Figure 6-7 : Menétrey-Willam failure criterion represented in Haigh-Westergaard coordinates – (a) 3D failure surface, (b) Rendulic plane and (c) deviatoric plane. Adopted from [39].**





**Figure 6-8 :** (a) Intersection of Rankine and Menétreay-Willam failure surfaces for  $\lambda_t = 2$  and (b) no intersection for  $\lambda_t = 1$ . Adopted from [39].

### 6.5.2 SBeta

The formulation of constitutive relations of this model is considered in the plane stress state. A smeared approach is used to model the material properties, such as cracks or distributed reinforcement. This means that material properties defined for a material point are valid within a certain material volume, which is in this case associated with the entire finite element. The constitutive model is based on the stiffness and is described by the equation of equilibrium in a material point:

$$\mathbf{s} = \mathbf{D}\mathbf{e}, \quad \mathbf{s} = \{\sigma_x, \sigma_y, \tau_{xy}\}^T, \quad \mathbf{e} = \{\varepsilon_x, \varepsilon_y, \gamma_{xy}\}^T \quad (6.32)$$

Where  $\mathbf{s}$ ,  $\mathbf{D}$  and  $\mathbf{e}$  are, a stress vector, a material stiffness matrix and a strain vector, respectively. The stress and strain vectors are composed of the stress components of the plane stress state  $\sigma_x$ ,  $\sigma_y$ ,  $\tau_{xy}$ , Figure 6-9, and the strain components  $\varepsilon_x$ ,  $\varepsilon_y$ ,  $\gamma_{xy}$ , Figure 6-10, where  $\gamma_{xy}$  is the engineering shear strain. The strains are common for all materials. The stress vector  $\mathbf{s}$  and the material matrix  $\mathbf{D}$  can be decomposed into the material components due to concrete and reinforcement as:

$$\mathbf{s} = \mathbf{s}_c + \mathbf{s}_s, \quad \mathbf{D} = \mathbf{D}_c + \mathbf{D}_s \quad (6.33)$$

The stress vector  $\mathbf{s}$  and both component stress vectors  $\mathbf{s}_c$ ,  $\mathbf{s}_s$  are related to the total cross section area. The concrete stress  $\mathbf{s}_c$  is acting on the material area of concrete  $A_c$  which is approximately set equal to the cross section of the composite material  $A_c \approx A$  (the area of concrete occupied by reinforcement is not subtracted). The matrix  $\mathbf{D}$  has a form of the Hooke's law for either isotropic or orthotropic material. For more details about material stiffness matrices, see subsection 6.5.7.

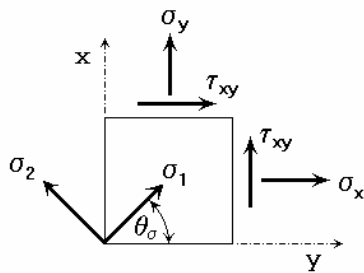


Figure 6-9 : Components of plane stress state. Adopted from [38].

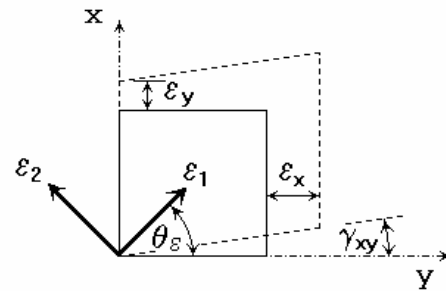


Figure 6-10 : Components of strain state. Adopted from [38].

### 6.5.3 Parameters of constitutive model

Material parameters are computed according to formulae listed in the table below [38]. Some parameters are derived from concrete cube strength  $f'_{cu}$  and program ATENA asks for that value during formation of new material.

Table 6-1 : Default formulae of material parameters

Parameter:	Formula:
Cylinder strength	$f'_c = -0.85f'_{cu}$
Tensile strength	$f'_t = 0.24f'_{cu}{}^{\frac{2}{3}}$
Initial elastic modulus	$E_c = (6000 - 15.5f'_{cu})\sqrt{f'_{cu}}$
Poisson's ratio	$\nu = 0.2$
Softening compression	$w_d = -0.0005 \text{ mm}$
Type of tension softening	1 – exponential, based on $G_f$
Compressive strength in cracked concrete	$c = 0.8$
Tension stiffening stress	$\sigma_{st} = 0$
Shear retention factor	variable
Tension-compression function type	linear
Fracture energy	$G_f = 0.000025f'_t{}^{ef} \text{ [MN/m]}$
Orientation factor for strain localization	$\gamma_{max} = 1.5$

### 6.5.4 Smearred cracks

Crack band model is described in [40] as basic constitutive model in ATENA based on the smeared crack concept and the damage approach. Concrete without cracks is considered isotropic while concrete with cracks is orthotropic. The material axes of cracked concrete, the orthotropy axes, can be defined by two models: rotated or fixed cracks.

ATENA Theory manual [38] describes two available models of smeared cracks, fixed and rotated crack model. In both models the crack is formed when the principal stress exceeds the tensile strength.

### 6.5.5 Fixed crack model

In the fixed crack model the crack direction is given by the principal stress direction at the moment of the crack initiation. During further loading this direction is fixed and represents the material axis of the orthotropy.

The principal stress and strain directions coincide in the uncracked concrete, because of the assumption of isotropy in the concrete component. After cracking the orthotropy is introduced. The weak material axis  $m_1$  is normal to the crack direction, the strong axis  $m_2$  is parallel with the cracks.

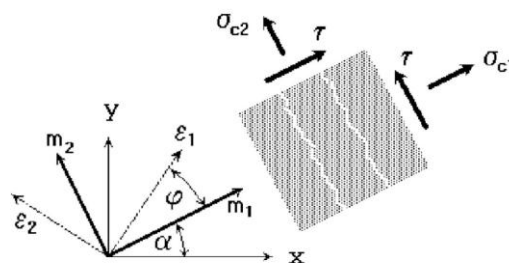


Figure 6-11: Fixed crack model. Stress and strain state. Adopted from [38].

In a general case the principal strain axes  $\varepsilon_1$  and  $\varepsilon_2$  rotate and need not to coincide with the axes of the orthotropy  $m_1$  and  $m_2$ . This produces a shear stress on the crack face as shown in Figure 6-11. The stress components  $\sigma_{c1}$  and  $\sigma_{c2}$  denote, respectively, the stresses normal and parallel to the crack plane and, due to shear stress, they are not the principal stresses.

### 6.5.6 Rotated crack model

In the rotated crack model, the direction of the principal stress coincides with the direction of the principal strain. Thus, no shear strain occurs on the crack plane and only two normal stress components must be defined, as shown in Figure 6-12.

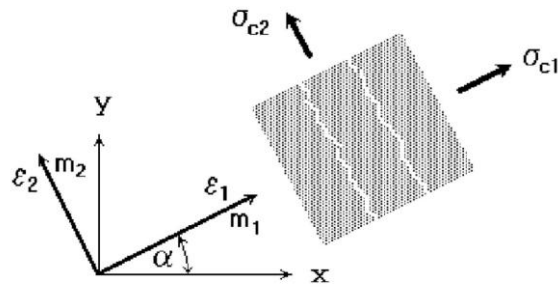


Figure 6-12 : Rotated crack model. Stress and strain state. Adopted from [38].

If the principal strain axes rotate during the loading the direction of the cracks rotates too. In order to ensure the coaxiality of the principal strain axes with the material axes the tangent shear modulus  $G_t$  is calculated as:

$$G_t = \frac{\sigma_{c1} - \sigma_{c2}}{2(\varepsilon_1 - \varepsilon_2)} \quad (6.34)$$

Paper [41] describes numerical simulations performed in ATENA 2D. Described numerical simulations were conducted on specimens with geometry similar to the geometry of specimens used in this master thesis. Three different material models were used: SBeta, 3D Non Linear Cementitious 2 and Microplane. The specimen geometry is shown in Figure 6-13 on the left and represents concrete specimen loaded in compression by increment of vertical displacement. Two steel prisms were inserted between jaws of testing machine and that is exactly the same case as in the configuration II (set One) or 2C (set Two) used in this thesis (for details concerning sets, see subsection 5.2).

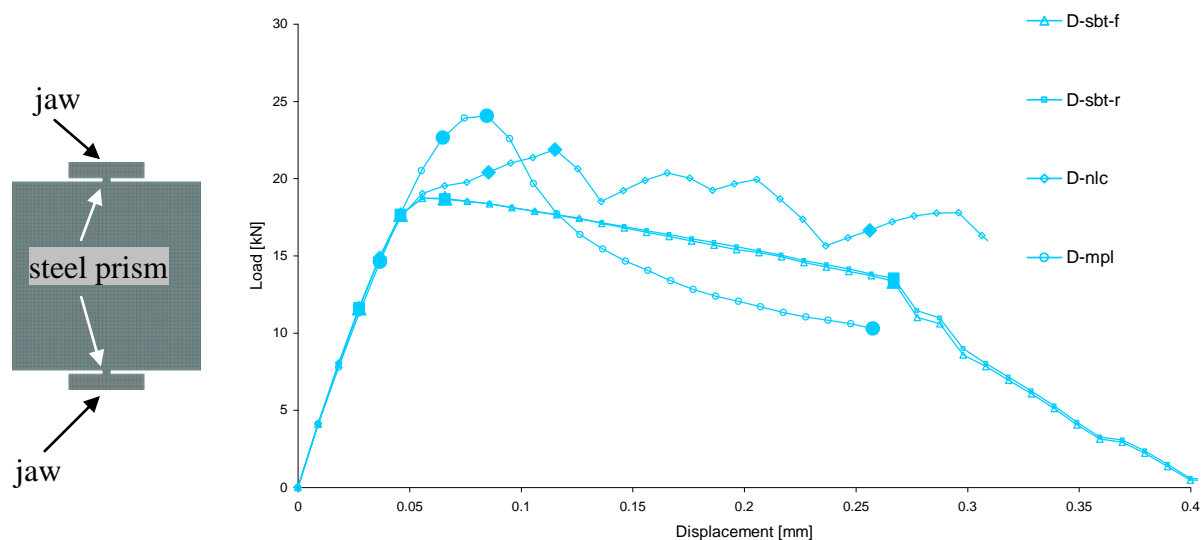


Figure 6-13 : Fixed vs. rotated crack model - scheme of specimen and its L–D curves. Adopted from [41].

As it can be observed in Figure 6-13, there is no difference in the shape of load–displacement curves obtained from simulations performed with the SBeta material model ei-

ther as fixed crack model (denoted as D-sbt-f in Figure 6-13) or as rotated crack model (denoted as D-sbt-r in Figure 6-13). Therefore, this parameter should not play role in simulations with specimens in the configuration II or 2C. The reason for this fact is probably the failure of specimen due to tensile splitting together with uniaxial compression (the direction of the cracks does not rotate).

### 6.5.7 Material stiffness matrices

Material stiffness matrix for uncracked concrete has the form of an elastic matrix of the isotropic material. It is written in the global coordinate system  $x$  and  $y$ .

$$\mathbf{D}_c = \frac{E}{1-\nu^2} \begin{bmatrix} 1 & \nu & 0 \\ \nu & 1 & 0 \\ 0 & 0 & \frac{1-\nu}{2} \end{bmatrix} \quad (6.35)$$

where  $E$  is the concrete elastic modulus derived from the equivalent uniaxial law. The Poisson's ratio  $\nu$  is constant.

For the cracked concrete the matrix has the form of the elastic matrix for the orthotropic material. The matrix is formulated in a coordinate system  $m_1, m_2$ , Figure 6-11 and Figure 6-12, which is coincident with the crack direction. This local coordinate system is referred to the superscript L used later in text. The direction 1 is normal to the crack and the direction 2 is parallel with the crack. The definition of the elastic constants for the orthotropic material in the plane stress state follows from the compliance relation:

$$\begin{Bmatrix} \varepsilon_1 \\ \varepsilon_2 \\ \gamma \end{Bmatrix} = \begin{bmatrix} \frac{1}{E_1} & -\frac{\nu_{21}}{E_2} & 0 \\ -\frac{\nu_{12}}{E_1} & \frac{1}{E_2} & 0 \\ 0 & 0 & \frac{1}{G} \end{bmatrix} \begin{Bmatrix} \sigma_1 \\ \sigma_2 \\ \tau \end{Bmatrix} \quad (6.36)$$

Firstly, it is good to eliminate the orthotropic Poisson's ratios for the cracked concrete because they are commonly not known. For the elimination the symmetry relation  $\nu_{12}E_2 = \nu_{21}E_1$  is used. Therefore, in Equation 6.36 there are only three independent elastic constants  $E_1, E_2, \nu_{21}$ . Assuming that  $\nu_{21} = \nu$  is the Poisson's ratio of the uncracked concrete and using the symmetry relation, it is obtained:

$$\nu_{12} = \frac{E_1}{E_2} \nu \quad (6.37)$$

The stiffness matrix  $\mathbf{D}_c^L$  is found as the inverse of the compliance matrix.

$$\mathbf{D}_c^L = H \begin{bmatrix} \xi & \nu\xi & 0 \\ \nu\xi & 1 & 0 \\ 0 & 0 & G \end{bmatrix}, \quad \xi = \frac{E_1}{E_2}, \quad H = E_1(1 - \xi\nu^2) \quad (6.38)$$

In the above relation  $E_2$  must be nonzero. If  $E_2$  is zero and  $E_1$  is nonzero then an alternative formulation is used with the inverse parameter  $1/\zeta = E_2/E_1$ . In the case that both elastic moduli are zero, the matrix  $\mathbf{D}_c^L$  is set equal to the null matrix. The matrix  $\mathbf{D}_c^L$  is transformed into the global coordinate system using the transformation matrix  $\mathbf{T}_\varepsilon$ .

$$\mathbf{D}_c = \mathbf{T}_\varepsilon^T \mathbf{D}_c^L \mathbf{T}_\varepsilon \quad (6.39)$$

## 6.6 Nonlinear equations

In general, there exist many variants on nonlinear analysis depending on how many nonlinear effects are accounted for. ATENA Theory manual [38] provides overview of terms commonly used for structural nonlinear analysis and specifies those that are implemented in ATENA.

It is important to realise that the whole structure does not have to be analysed using a full nonlinear formulation and thus it is possible to use a simplified (or even linear) formulation in many cases. Whether the inaccuracies due to a simplified formulation are acceptable or not is a matter of engineering knowledge and practise.

Linear formulation (the simplest one) is characterised by the following assumptions:

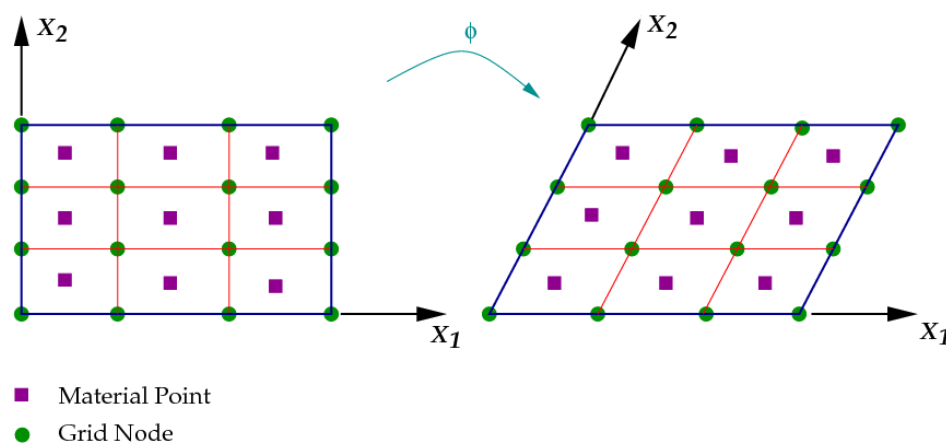
- the constitutive equations are linear, i.e. the generalised form of Hooke's law is used;
- the geometric equations are linear thus the quadratic terms are neglected, i.e. during analysis the shape and position of the structure is neglected;
- both the loading and boundary conditions are conservative, i.e. they are constant throughout the whole analysis irrespective the structural deformation, time etc.

Linear constitutive equations are usually employed for a material which is far from its failure point (usually up to 50% of its maximum strength). Geometric equations can be considered linear if deflections of a structure are much smaller than its dimensions. This must be satisfied not only for the whole structure but also for its parts. It is important to realise that a linear solution is permissible only in the case of small strains.

Despite the fact that for vast majority of structures linear simplifications are quite acceptable there are structures where it is necessary to take in account some kind of nonlinear behaviour. The resulting governing equations are then much more complicated and normally they do not have a closed form solution. Consequently some nonlinear iterative solution scheme must be used.

Nonlinear analysis classified according to a type of nonlinear behaviour:

- **Material nonlinearity.** This is the most common case for ordinary reinforced concrete structures. Because of serviceability limitations, deformations are relatively small.
- **Geometric nonlinearity.** Deformations (either displacement only or both displacements and rotations) are large. The equilibrium equations must be used on the deformed shape of the structure however the relative deformations (strains) are still small. The complete form of the geometric equations, including quadratic terms, has to be employed but constitutive equations are linear. This group of nonlinear analysis includes most stability problems.
- Combined **material** and **geometric nonlinearity.** It is usually not possible to suddenly apply the total value of load but it is necessary to integrate increments (or loading increments) in time. This is the most accurate and general approach, but unfortunately, it is also the most complicated.



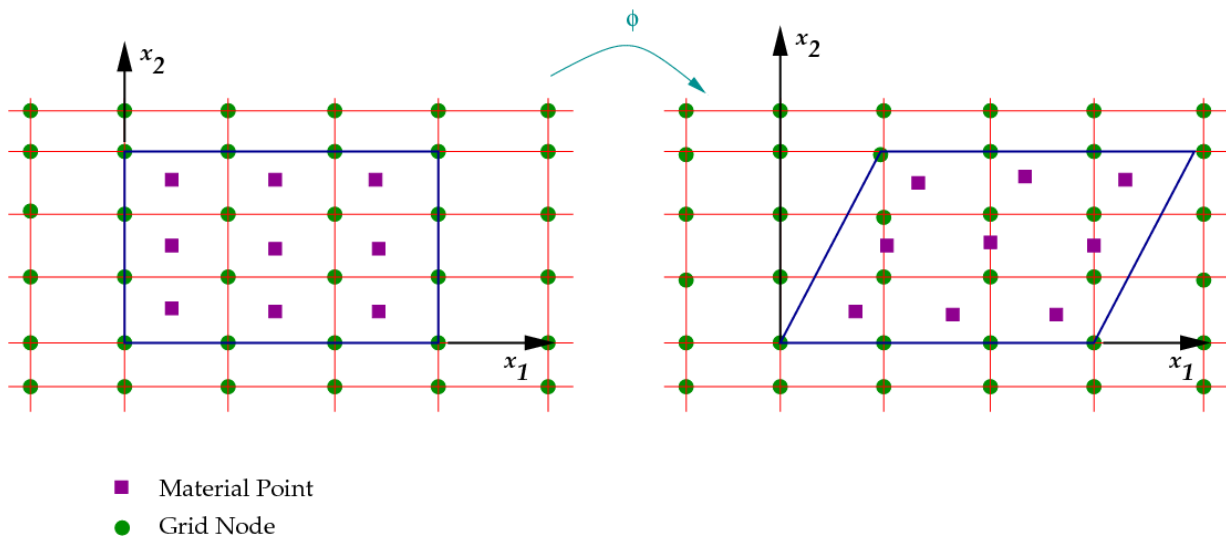
**Figure 6-14 : Lagrangian mesh. Adopted from [42].**

There are 2 basic possibilities how to formulate the general structure behaviour based on its deformed shape:

- **Lagrange formulation.** The behaviour of infinitesimal particles of volume  $dV$  is the main point of interest. Volume is dependent on a loading level applied and, consequently, on the amount of current deformations. This method is usually used to calculate civil engineering structures. It is possible to visualise the Lagrange formulation in terms of the corresponding meshes. The Lagrangian mesh is shown in Figure 6-14 as mesh drawn on the body which deforms together with the body. Both the nodes and the material points change position as the body deforms, however, the position of the material points relative to the nodes remain fixed.

- **Euler formulation.** The essential idea of Euler's formulation is to study the "flow" of the structural material through infinitesimal and fixed volumes of the structure. This is the favourite formulation for fluid analysis, analysis of gas flow etc. where large material flows exist. It is possible to visualise the Euler formulation in terms of the corresponding meshes. The Euler mesh is shown in Figure 6-15 as "background" mesh. The body flows through the mesh as it deforms. The nodes remain fixed and the material points move through the mesh. The position of a material point relative to the nodes varies with the motion.

The Lagrangian formulation is better for structural analysis. Two forms of the Lagrangian formulation are possible. The governing equations are either written with respect to the undeformed original configuration at time  $t = 0$  or with respect to the most recent deformed configuration at time  $t$ . The former case is referred to as the Total Lagrangian formulation (TL) while the latter one is called the Updated Lagrangian formulation (UL). It is difficult to decide which formulation is better because both have their advantages and drawbacks. Usually it depends on a particular structure being analysed and which one to use is a matter of engineering judgement.



**Figure 6-15 : Eulerian mesh. Adopted from [42].**

ATENA uses UL formulation and supports the highest, i.e. 3<sup>rd</sup> level of nonlinear behaviour. Combined material and geometric nonlinearity was used for all simulations described in this thesis.



## 6.7 Solution of nonlinear equations

The methods for solution of a set of nonlinear equations, which are implemented in ATENA, are described in this subsection. All methods have to solve a set of linear algebraic equations in the form:

$$\mathbf{A}\underline{x} = \underline{b} \quad (6.40)$$

where  $\mathbf{A}$ ,  $\underline{x}$ ,  $\underline{b}$  stands for a global structural matrix and vectors of unknown variables and right hand side of the problem, respectively.

### 6.7.1 Linear solvers – Cholesky decomposition

Two types of solvers are supported in ATENA; direct and iterative. Direct solver is recommended for smaller problems or problems that are ill-posed. On the other hand, iterative solvers are typically more efficient to solve well-posed large 3D analyses.

The well-known Cholesky decomposition is used as a direct solver. The matrix  $\mathbf{A}$  is decomposed into:

$$\mathbf{A} = \mathbf{L}\mathbf{D}\mathbf{U} \quad (6.41)$$

where  $\mathbf{L}$ ,  $\mathbf{U}$  is lower and upper triangular matrix, respectively, and  $\mathbf{D}$  is diagonal matrix.

Equation 6.40 is then solved in two steps:

$$\underline{v} = \mathbf{L}^{-1}\underline{b} \quad (6.42)$$

$$\underline{x} = (\mathbf{D}\mathbf{U})^{-1}\underline{v} \quad (6.43)$$

ATENA embraces many iterative solvers but from practical point of view only a few of them are recommended. Each of them typically consists of two routines, one for "preparation" of the solution and the other for the solution itself, i.e. "execution" phase. The former routine is particularly important for the case of preconditioned iterative solvers. This is where a preconditioning matrix is created. The most efficient preconditioning routines are based on incomplete Cholesky decomposition. The preconditioning matrix  $\mathbf{A}'$  is decomposed in the same way as in Equation 6.41, i.e.

$$\mathbf{A}' = \mathbf{L}'\mathbf{D}'\mathbf{U}' \quad (6.44)$$

Comparing  $\mathbf{A}$  and  $\mathbf{A}'$ , it can be written:

$$\text{for } a_{ij} \neq 0; \quad a'_{ij} = a_{ij} \quad (6.45)$$

$$\text{for } a_{ij} = 0; \quad a'_{ij} \neq a_{ij} \quad (6.46)$$

The incomplete Cholesky decomposition is carried out in the same way as complete Cholesky decomposition (Equation 6.41), however, entries in  $\mathbf{A}$  which were originally zero and became nonzero during the factorisation are ignored, i.e. they stay zero even after the factorisation.

### 6.7.2 Nonlinear solvers – Full Newton-Raphson method

Full Newton-Raphson (FNR) method uses the concept of incremental step by step analysis which leads to the following set of nonlinear equations:

$$\mathbf{K}(\underline{p}) \Delta \underline{p} = \underline{q} - f(\underline{p}) \quad (6.47)$$

where  $\underline{q}$  is the vector of total applied joint load,

$f(\underline{p})$  is the vector of internal joint forces,

$\Delta \underline{p}$  is the deformation increment due to loading increment,

$\underline{p}$  are the deformations of structure prior to load increment,

$\mathbf{K}(\underline{p})$  is the stiffness matrix relating loading increments to deformation increments.

The right hand side of Equation 6.47 represents out-of-balance forces during a load increment, i.e. the total load level after applying the loading increment minus internal forces at the end of the previous load step. Generally, the stiffness matrix is deformation dependent, i.e. a function of  $\underline{p}$ , but this is usually neglected within a load increment in order to preserve linearity. In such case the stiffness matrix is based on the value of  $\underline{p}$  pertaining to the level prior to the load increment. The Equation 6.47 is nonlinear because of the nonlinear properties of the internal forces:

$$f(k\underline{p}) \neq kf(\underline{p}) \quad (6.48)$$

and nonlinearity in the stiffness matrix:

$$\mathbf{K}(\underline{p}) \neq \mathbf{K}(\underline{p} + \Delta \underline{p}) \quad (6.49)$$

where  $k$  is an arbitrary constant.

The set of equations represents the mathematical description of structural behaviour during one step of the solution. Rewriting of Equation 6.47 for the  $i$ -th iteration within a distinct loading increment gives:

$$\mathbf{K}(\underline{p}_{i-1}) \Delta \underline{p}_i = \underline{q} - f(\underline{p}_{i-1}) \quad (6.50)$$

All the quantities for the  $(i-1)$ -th iteration have already been calculated during previous solution steps. Now it is necessary to solve problem for  $\underline{p}_i$  at load level  $\underline{q}$  using:

$$\underline{p}_i = \underline{p}_{i-1} + \Delta \underline{p}_i \quad (6.51)$$

As pointed out earlier, Equation 6.50 is nonlinear and therefore it is necessary to iterate until some convergence criterion is satisfied. The following possibilities are supported in ATENA:

$$\sqrt{\frac{\Delta \underline{p}_i^T \Delta \underline{p}_i}{\underline{p}_i^T \underline{p}_i}} \leq \varepsilon_{\text{rel. displ}} \quad (6.52)$$

$$\sqrt{\frac{(\underline{q}-\underline{f}(\underline{p}_{i-1}))^T(\underline{q}-\underline{f}(\underline{p}_{i-1}))}{\underline{f}(\underline{p}_i)^T \underline{f}(\underline{p}_i)}} \leq \varepsilon_{\text{rel.force}} \quad (6.53)$$

$$\sqrt{\frac{\Delta \underline{p}_i^T (\underline{q}-\underline{f}(\underline{p}_{i-1}))}{\underline{p}_i^T \underline{f}(\underline{p}_i)}} \leq \varepsilon_{\text{rel.energy}} \quad (6.54)$$

$$\sqrt{\frac{\max(\underline{q}^k-\underline{f}^k(\underline{p}_{i-1}))\max(\underline{q}^k-\underline{f}^k(\underline{p}_{i-1}))}{\max(\underline{f}^k(\underline{p}_i))\max(\underline{f}^k(\underline{p}_i))}} \leq \varepsilon_{\text{abs.force}} \quad (6.55)$$

where  $k$  marks  $k$ -th component of the specified vector. The Equation 6.52 checks the norm of deformation changes during the last iteration whereas the Equation 6.53 checks the norm of the out-of-balance forces. The Equation 6.54 checks out-of-balance energy and the last Equation 6.55 checks out-of-balanced forces in terms of maximum components. The values of convergence limits  $\varepsilon$  are set by default to 0.01 for the first 3 criteria and 0.0001 for the last one. The Figure 6-16 shows the FNR method.

### 6.7.3 Nonlinear solvers – Modified Newton-Raphson Method

The most time consuming part of solution of Equation 6.50 is the stiffness matrix recalculation  $\mathbf{K}(\underline{p}_{i-1})$  at each iteration. In many cases, this is not necessary, and it is possible to use matrix  $\mathbf{K}(\underline{p}_0)$  from the first iteration of the step. This is the basic idea of the so-called Modified Newton-Raphson (MNR) method. It produces very significant time saving, but on the other hand, it also exhibits worse convergence of the solution procedure. The MNR method is mathematically expressed as:

$$\mathbf{K}(\underline{p}_{i-1}) \simeq \mathbf{K}(\underline{p}_0) \quad (6.56)$$

The Figure 6-17 shows MNR method. Comparing Figure 6-16 and Figure 6-17 it is apparent that the MNR method does not converge as fast as FNR method. On the other hand, a single iteration costs less computing time because it is necessary to assemble and eliminate the stiffness matrix only once. In practice a careful balance of the two methods is usually adopted in order to produce the best performance for a particular case. It is recommended to start a solution with the FNR method and later, i.e. near extreme points, switch to the MNR method to avoid divergence.

Newton-Rapson methods (FNR; MNR) were used for all simulations described in this thesis. According to [43], it is recommended to use these methods because they are the only solution scheme which allows the analyst to specify an exact load level at which the stresses

and deflections are studied. Consequently they are particularly suitable for design of a practical structure allowing for various nonlinearities and under a set of fixed loads, such as the design loads.

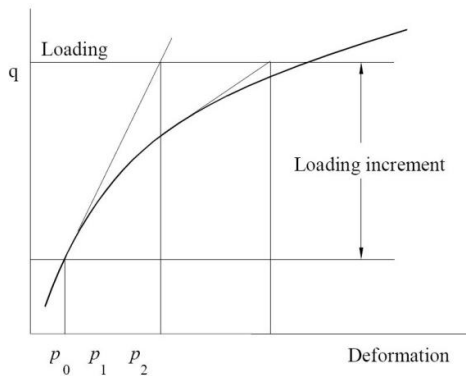


Figure 6-16 : Full Newton-Raphson method. Adopted from [13].

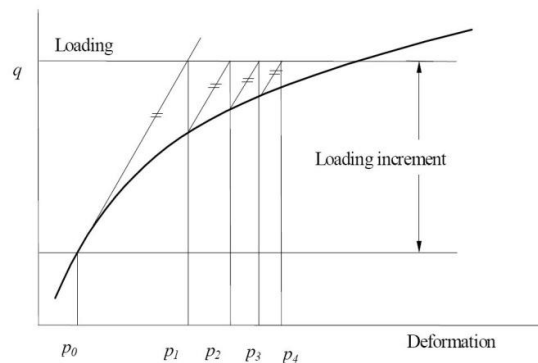


Figure 6-17 : Modified Newton-Raphson method. Adopted from [13].

### 6.7.4 Nonlinear solvers – Arc-length method

For the reason that the Arc-length method was not used for any simulation described in this thesis, this subsection brings only brief description of this method. The main idea of Arc-length method is well explained by its name, arc length. The primary task is to observe complete load–displacement relationship rather than applying a constant loading increment as it is in the Newton-Raphson method. Hence this method fixes not only the loading but also the displacement conditions at the end of a step. There are many ways of fixing these issues but one of the most common is to establish the length of the loading vector and displacement changes within the step. The Figure 6-18 shows the scheme of the Arc-length method. For more information, see e.g. ATENA Theory manual [38] or paper [43].

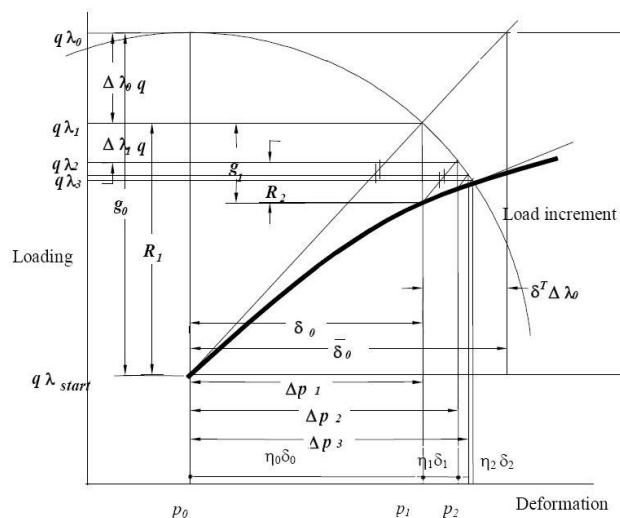


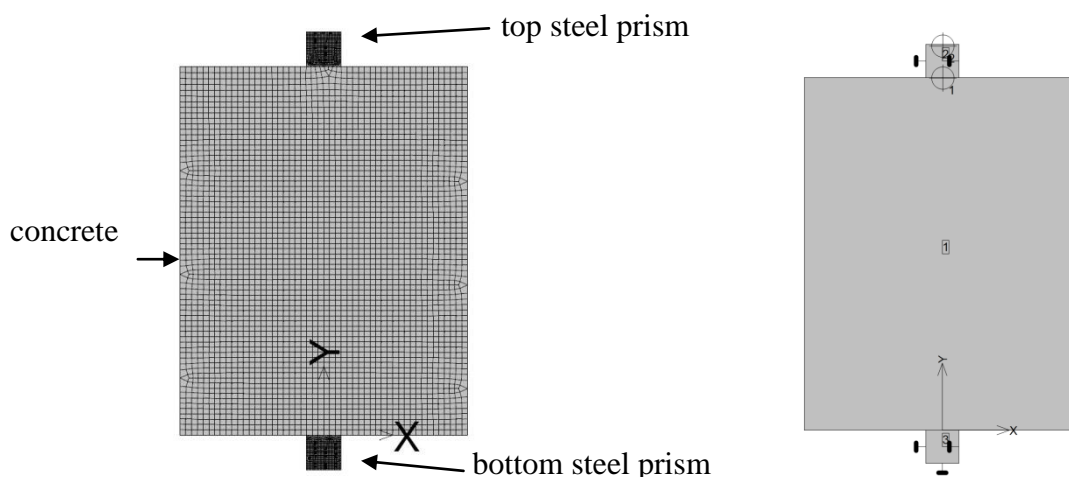
Figure 6-18 : The Arc-length method. Adopted from [13].

## 7 Simulations in ATENA 2D

Initiative idea how to simulate the conducted experiments was to create numerical 2D model of the experiment in ATENA 2D. The main aim of the 2D study was to find out if the 2D analysis is capable to capture fracture events arising in the tested concrete blocks. The reason for such decision was based on the knowledge that 2D analysis takes only fraction of computational power, necessary for analysis, in comparison with 3D analysis (of course, this is valid for models that have same/similar boundary conditions, mesh size, material model etc.). It is clear that number of mesh nodes in 2D case is relatively low (comparing same mesh size) and therefore it should reduce the computational time. Disadvantage of such analysis is lack of third dimension and therefore it can happen that we lose some important outputs or behaviours of our modelled problem. This section and the following section 8 present results of 2D and 3D simulations, respectively.

### 7.1 Parametric study

Parametric study of mesh refinement was performed in order to investigate how "sensitive" are the results of numerical simulations to element mesh size. The goal of the parametric study of material model was to select appropriate material model for post-processing. For these purposes the model of concrete cube loaded by two steel loading prisms was used (Figure 7-1). In order to get value of loading force and displacement, two monitors were used.



**Figure 7-1 : Specimen with 2 steel loading prisms**

**Figure 7-2 : Monitors and boundary conditions**

Figure 7-2 shows location of monitor no.1 and no.2, recording magnitude of vertical displacement and applied force, respectively. Bottom loading prism was fixed in all directions and the upper one was fixed only in the direction of  $x$ -axis and set free along  $y$ -axis because the loading by increment of vertical displacement was carried out along this axis. There were

used 30 incremental steps each with value of  $5 \times 10^{-6}$  m and the Newton-Raphson solution method was applied in all analysis steps, see subsection 6.7 for more details.

Dimensions of the concrete part were the same as for the configuration BII, i.e.  $50 \times 64 \times 64$  mm (in the direction of:  $x$ -axis  $\times$   $y$ -axis  $\times$  thickness of macro-element). Steel loading prisms had rectangular base  $6 \times 6$  mm (in the direction of:  $x$ -axis  $\times$   $y$ -axis) and thickness of 64mm which corresponds to the thickness of macro-element.

**Table 7-1 : Relevant parameters of material models**

	Material model		
	SBeta	3D Non Linear Cementitious 2	Plane Stress Elastic Isotropic; Plane Strain Elastic Isotropic
Elastic modulus $E$ [MPa]	20 000	20 000	210 000
Poisson's ratio $\nu$ [-]	0.200	0.200	0.300
Specific material weight $\rho$ [MN/m <sup>3</sup> ]	2.230E-02	2.230E-02	7.850E-02
Tensile strength $f_t$ [MPa]	2.052	2.052	
Compressive strength $f_c$ [MPa]	-21.250	-21.250	
Specific fracture energy $G_f$ [MN/m]	5.130E-05	5.130E-05	
Crack model	Fixed	Fixed	
Critical compressive displacement $w_d$ [m]	-5.000E-04	-5.000E-04	

Applied material model for concrete part was either Sbeta or 3D Non Linear Cementitious 2, both with default values calculated by the program, for concrete with cube strength  $f'_{cu} = 25$  MPa. Value of elastic modulus and special material weight was modified according to the material parameters specified in paper [44] which describes material parameters for the specimen set One. Material model used for steel prisms was either Plane Stress Elastic Isotropic or Plane Strain Elastic Isotropic, both with specific material weight  $\rho = 7.85 \times 10^{-2}$  MN/m<sup>3</sup> corresponding to plain mild steel. All relevant parameters of material models are listed in Table 7-1.

**Table 7-2 : Macro-element mesh settings for SBeta specimens**

Specimen	Mesh type	FE mesh				Mesh parameters	
		Element size [mm]			Element shape smoothing	No. of nodes	No. of elements
		Concrete part	Top steel prism	Bottom steel prism			
<b>SBeta_es10_2x2</b>	Quadrilaterals	1.0	0.2	0.2	Yes	5623	5407
<b>SBeta_es10_7x10</b>	Quadrilaterals	1.0	0.7	1.0	Yes	3743	3597
<b>SBeta_es10_8x8</b>	Quadrilaterals	1.0	0.8	0.8	Yes	3773	3624
<b>SBeta_es10_8x10</b>	Quadrilaterals	1.0	0.8	1.0	Yes	3743	3597
<b>SBeta_es10_10x10</b>	Quadrilaterals	1.0	1.0	1.0	Yes	3719	3575

### 7.1.1 Mesh connectivity

Impact of mesh connectivity along border between macro-elements was studied using model SBeta\_es10 (where SBeta denotes the SBeta material model available in ATENA 2D and expression "es" is abbreviation for element size followed by number expressing element size in tenths of millimetre). In all cases Plane Stress Elastic Isotropic material model was used for loading prisms in order to keep the same material state for concrete and steel part (the SBeta material is always considered in the plane stress state, for more details, see subsection 6.5.2).

**Table 7-3 : Generated mesh for SBeta\_es10\_2x2 and 8x10 specimens**

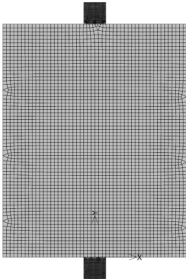
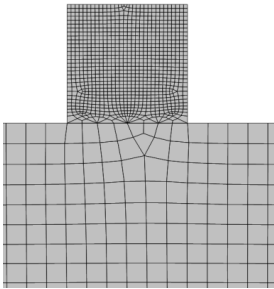
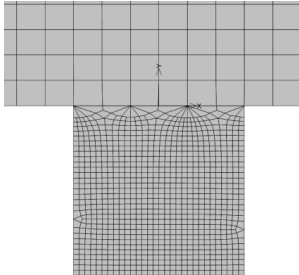
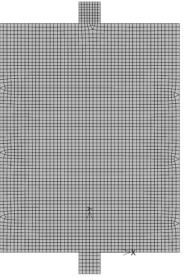
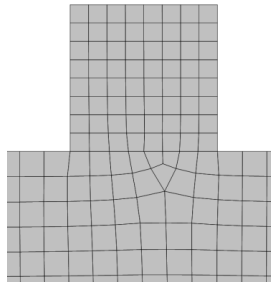
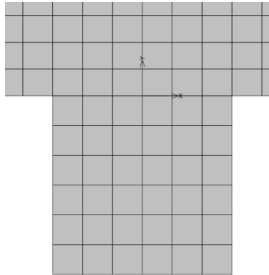
Whole specimen	Magnified upper part	Magnified bottom part
 <p>SBeta_es10_2x2</p>		
 <p>SBeta_es10_8x10</p>		

Table 7-2 shows variants of specimen where only mesh size of top and bottom steel prism is varying. In order to avoid sharp angles in elements, element shape smoothing was used. Examples of generated mesh for Sbeta\_es10\_2x2 and Sbeta\_es10\_8x10 specimens are shown in Table 7-3 (numeral appended to the expression SBeta\_es10\_ represents FE mesh size of upper loading steel prism in tenths of millimetre (= single or double digit number) separated by the symbol "x" and followed by numeral representing FE mesh size of bottom loading steel prism in tenths of millimetre (= single or double digit number)); for examples of all used configurations see Appendix A 1. The FE mesh size was not chosen arbitrarily never-

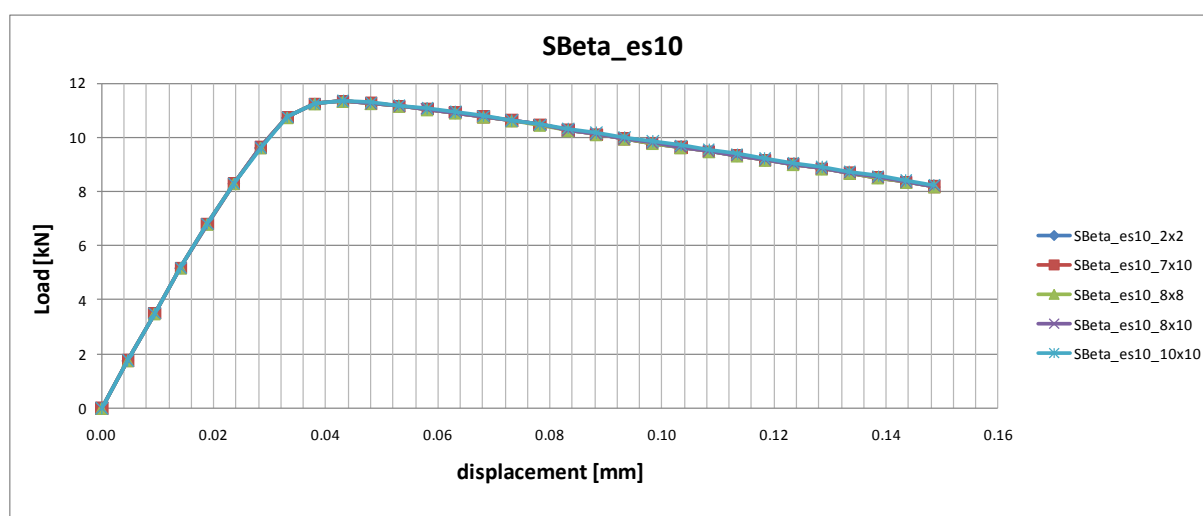
theless in such a way that the mesh connection between elements presented smooth transition (i.e. no large distortions were presented).

Table 7-4 shows information concerning all performed analyses related to mesh connectivity. One analysis took approximately half of a day and had size about 80 MB. Load imposed by vertical displacement of upper loading prism had its peak for all specimens identically at 9<sup>th</sup> analysis step.

**Table 7-4 : Analysis information for SBeta\_es10 specimens**

Specimen	Elapsed CPU time for all steps		No. of computed steps	Max. Load at step no.	Average CPU time per step		File size [kB]
	[s]	[hours:minutes:seconds]			[s]	[hours:minutes:seconds]	
<b>SBeta_es10_2x2</b>	43 384	12:03:04	30	9	1446	0:24:06	95 213
<b>SBeta_es10_7x10</b>	28 789	7:59:49	30	9	960	0:15:59	79 713
<b>SBeta_es10_8x8</b>	41 260	11:27:40	30	9	1375	0:22:55	80 430
<b>SBeta_es10_8x10</b>	36 049	10:00:49	30	9	1202	0:20:01	79 724
<b>SBeta_es10_10x10</b>	43 099	11:58:19	30	9	1437	0:23:56	80 209

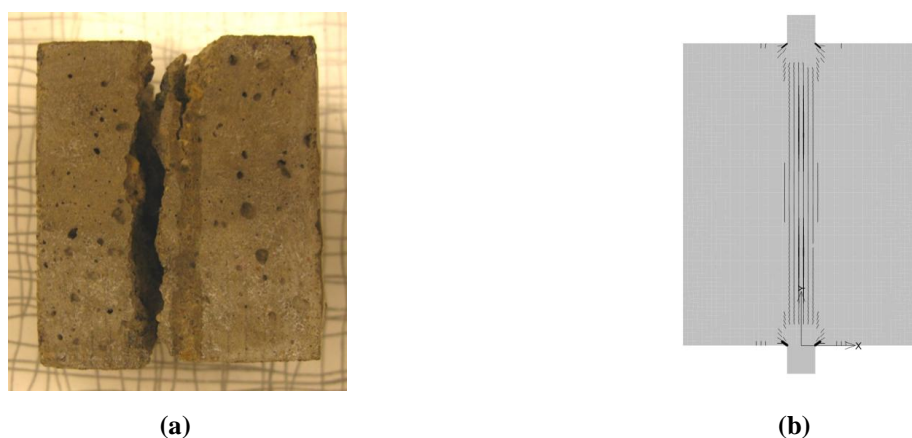
In the post-processing, data recorded from monitors were imported with help of macros, used in Load Results workbook, created in software Microsoft Excel (for more details about created macros, see subsection 9.2.1). Data were plotted on the graphs where the horizontal axis indicates displacement of upper loading prism and the vertical axis shows the imposed load. From the Figure 7-3 it can be observed that the imposed load reaches a peak (11.3 kN) at displacement of approximately 0.04 mm and then starts to decline. The explanation for this decline is the fact that the concrete in compression fails by tensile splitting as can be observed in Figure 7-4 for real concrete specimen (a) or for numerical model (b).



**Figure 7-3 : SBeta\_es10 load–displacement curves**



By deeper observation of Figure 7-3 it is possible to see that all curves are perfectly overlapping, therefore, it can be concluded that load–displacement (L–D) curve is independent on mesh connectivity.



**Figure 7-4 : Failure by tensile splitting – (a) Real concrete specimen BII, (b) Numerical model SBeta\_es10\_10x10**

Another output compared in post-processing was the Crack width representing the calculated total crack opening displacement within the crack band. ATENA text output offers COD (Crack opening displacement) which is denoted in the graphic output as Crack width (this thesis uses tag Crack width because most ATENA users are working with graphic output). Crack width at peak point of L–D curve was tabulated. According to values listed in Table 7-5 it is noticeable that there are two groups of maximal Crack widths. First group is represented by one specimen with finest and one with coarsest loading prism mesh size and the average of maximal Crack width in these specimens is about 0.00269 mm. The remaining three specimens with the average of maximal Crack width about 0.00329 mm are members of the second group. It is evident that the maximal Crack width is not directly proportional to the mesh refinement and the same behaviour can be observed on crack patterns listed in the Appendix A 2 (example of crack pattern is shown in Figure 7-4 (b)).

**Table 7-5 : Crack width SBeta\_es10**

Specimen	Load step no.	Max. Crack width (in elements)	
		[m]	[mm]
SBeta_es10_2x2	9	2.713E-06	0.00271
SBeta_es10_7x10	9	3.312E-06	0.00331
SBeta_es10_8x8	9	3.325E-06	0.00333
SBeta_es10_8x10	9	3.243E-06	0.00324
SBeta_es10_10x10	9	2.657E-06	0.00266

To summarise, this study examined the role of mesh connectivity and found out that the mesh refinement of loading prisms does not affect shape of L–D curve, in other words it

does not affect load imposed by displacement. Mesh refinement has impact on maximal Crack width therefore it was made a decision to use the same or at least very similar mesh size for specimen body and the adjacent loading prisms in further studies. It should be noted that the mesh refinement of loading prisms slightly affects the shape of mesh of concrete part (due to the connectivity) and therefore the maximal Crack width can not be considered as a decisive parameter but merely as a guideline.

### 7.1.2 FE mesh size (density)

Mesh size is important parameter that can influence simulations results. In general too little elements reduce the computational time and unfortunately the precision of results as well. Too many elements increase rapidly computational time sometimes even without any gain on results precision. For the above mentioned reasons a selection of proper mesh size is a bit tricky and needs at least basic investigation.

In this thesis, parametric study of mesh size on twenty-one specimens was performed. Simulations were labelled in the same manner as in the previous subsection, irrespective that fact, the tagging is explained once more in order to get better understanding of the labels. The label consists of expression representing material model used for concrete part (SBeta denotes the SBeta material model and NLC2 denotes the 3D Non Linear Cementitious 2, both available in ATENA 2D; if the label NLC2 is followed by "sa" or "se" expression then the expression denotes material modelled in the state of plane strain or plain stress, respectively; for information concerning plane strain/stress see subsection 6.3) separated by the underscore "\_" with appended expression "es" ("es" is abbreviation for element size) followed by double digit number expressing FE mesh size of concrete part in tenths of millimetre, once more separated by the underscore "\_" with appended numeral representing FE mesh size of upper loading steel prism in tenths of millimetre (= single or double digit number) separated by the symbol "x" and followed by numeral representing FE mesh size of bottom loading steel prism in tenths of millimetre (= single or double digit number).

As an illustration, NLC2se\_es18\_15x15 denotes specimen with the 3D Non Linear Cementitious 2 material model modelled in the state of plane stress, FE mesh size of concrete part is 1.8 mm and FE mesh size of upper and lower loading steel prism is identically 1.5 mm. Material model for loading prisms was either Plane Stress Elastic Isotropic or Plane Strain Elastic Isotropic depending on the material state used for concrete part (the SBeta material is always considered in the plane stress state).

**Table 7-6 : Macro-element mesh settings for used specimens**

Specimen	Mesh type	FE mesh			Element shape smoothing	Mesh parameters	
		Element size [mm]				No. of nodes	No. of elements
		Concrete part	Top steel prism	Bottom steel prism			
NLC2_es03_3x3	Quadrilaterals	0.3	0.3	0.3	Yes	40 133	39 668
NLC2_es04_4x4	Quadrilaterals	0.4	0.4	0.4	Yes	21 283	20 928
NLC2_es05_5x5	Quadrilaterals	0.5	0.5	0.5	Yes	13 565	13 286
NLC2_es06_5x6	Quadrilaterals	0.6	0.5	0.6	Yes	10 379	10 143
NLC2_es08_8x8	Quadrilaterals	0.8	0.8	0.8	Yes	5 761	5 582
NLC2_es14_15x15	Quadrilaterals	1.4	1.5	1.5	Yes	1 929	1 828
NLC2_es18_15x15	Quadrilaterals	1.8	1.5	1.5	Yes	1 177	1 094
SBeta_es03_3x3	Quadrilaterals	0.3	0.3	0.3	Yes	40 133	39 668
SBeta_es04_4x4	Quadrilaterals	0.4	0.4	0.4	Yes	21 283	20 928
SBeta_es05_5x5	Quadrilaterals	0.5	0.5	0.5	Yes	13 565	13 286
SBeta_es06_5x6	Quadrilaterals	0.6	0.5	0.6	Yes	10 379	10 143
SBeta_es08_8x8	Quadrilaterals	0.8	0.8	0.8	Yes	5 761	5 582
SBeta_es14_15x15	Quadrilaterals	1.4	1.5	1.5	Yes	1 929	1 828
SBeta_es18_15x15	Quadrilaterals	1.8	1.5	1.5	Yes	1 177	1 094

Table 7-6 shows variants of specimens used in this parametric study. As can be observed from the Table 7-6, the denser mesh the higher number of nodes/elements is necessary to generate. With increasing number of nodes/elements increases file size that is listed in Table 7-7. File size varies between several tens of MB (specimens with coarsest mesh size of concrete part) and several hundreds of MB (specimens with finest mesh size of concrete part).

Table 7-7 shows information concerning all performed analyses related to study of mesh size. One analysis took from several hours (specimens with coarsest mesh size of concrete part) till several days (specimens with finest mesh size of concrete part) and all analyses were computed on Dell Precision T5500 workstation (12 cores). Load imposed by vertical displacement of upper loading prism had not its peak for all specimens identically nevertheless once at 8<sup>th</sup>, six times at 9<sup>th</sup>, eight times at 10<sup>th</sup>, twice at 11<sup>th</sup>, once at 12<sup>th</sup> and once at 13<sup>th</sup> analysis step. This fact shows that imposed load is mesh size dependent because all the simulations were loaded at all steps by equally large displacement. One can notice that Table 7-7 includes empty rows by specimens NLC2sa\_es03\_3x3 and NLC2se\_es03\_3x3. These rows are empty because of ATENA 2D incapability to compute simulations with so many mesh elements (39 668). Error warnings shown in Figure 7-6 occurred during calculation initialisation of these specimens. For the same reason, specimen SBeta\_es03\_3x3 was possible to calculate only till 29<sup>th</sup> analysis step. Example of generated mesh for material model with the label XX\_es05\_5x5 (XX = SBeta or 3D Non Linear Cementitious 2) is shown in Table 7-8 ; for

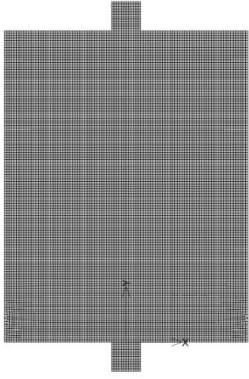
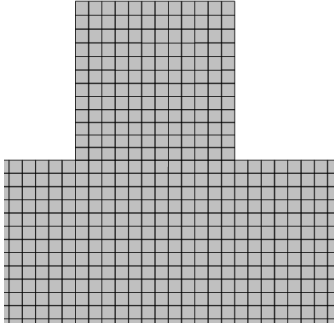
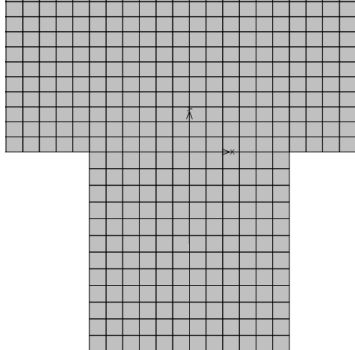
examples of all used configurations see Appendix A 3. The FE mesh size for all model parts was not chosen arbitrarily but in accordance with decision that was made at the end of previous subsection (to use the same or at least very similar mesh size for specimen body and adjacent loading prisms).

**Table 7-7 : Analysis information for used specimens**

Specimen	Elapsed CPU time for all steps		No. of computed steps	Max. Load at step no.	Average CPU time per step		File size [kB]
	[s]	[hours:minutes:seconds]			[s]	[hours:minutes:seconds]	
NLC2sa_es03_3x3	-	-	0	-	-	-	10 192
NLC2se_es03_3x3	-	-	0	-	-	-	10 192
NLC2sa_es04_4x4	241 044	66:57:24	30	10	8035	2:13:54	569 096
NLC2se_es04_4x4	265 489	73:44:49	30	9	8850	2:27:29	451 825
NLC2sa_es05_5x5	98 029	27:13:49	30	10	3268	0:54:27	353 520
NLC2se_es05_5x5	203 456	56:30:56	30	10	6782	1:53:01	289 743
NLC2sa_es06_5x6	88 057	24:27:37	30	10	2935	0:48:55	275 418
NLC2se_es06_5x6	193 508	53:45:08	30	10	6450	1:47:30	223 636
NLC2sa_es08_8x8	16 667	4:37:47	30	9	556	0:09:15	154 403
NLC2se_es08_8x8	52 284	14:31:24	30	10	1743	0:29:02	125 481
NLC2sa_es14_15x15	44 761	12:26:01	30	11	1492	0:24:52	54 743
NLC2se_es14_15x15	15 079	4:11:19	30	13	503	0:08:22	43 249
NLC2sa_es18_15x15	6 083	1:41:23	30	10	203	0:03:22	33 650
NLC2se_es18_15x15	8 269	2:17:49	30	11	276	0:04:35	27 512
SBeta_es03_3x3	142 327	39:32:07	29	9	4908	1:21:47	770 272
SBeta_es04_4x4	92 088	25:34:48	30	9	3070	0:51:09	426 863
SBeta_es05_5x5	66 173	18:22:53	30	9	2206	0:36:45	279 360
SBeta_es06_5x6	86 661	24:04:21	30	8	2889	0:48:08	217 071
SBeta_es08_8x8	49 373	13:42:53	30	9	1646	0:27:25	121 915
SBeta_es14_15x15	51 341	14:15:41	30	12	1711	0:28:31	46 202
SBeta_es18_15x15	39 348	10:55:48	30	10	1312	0:21:51	29 503

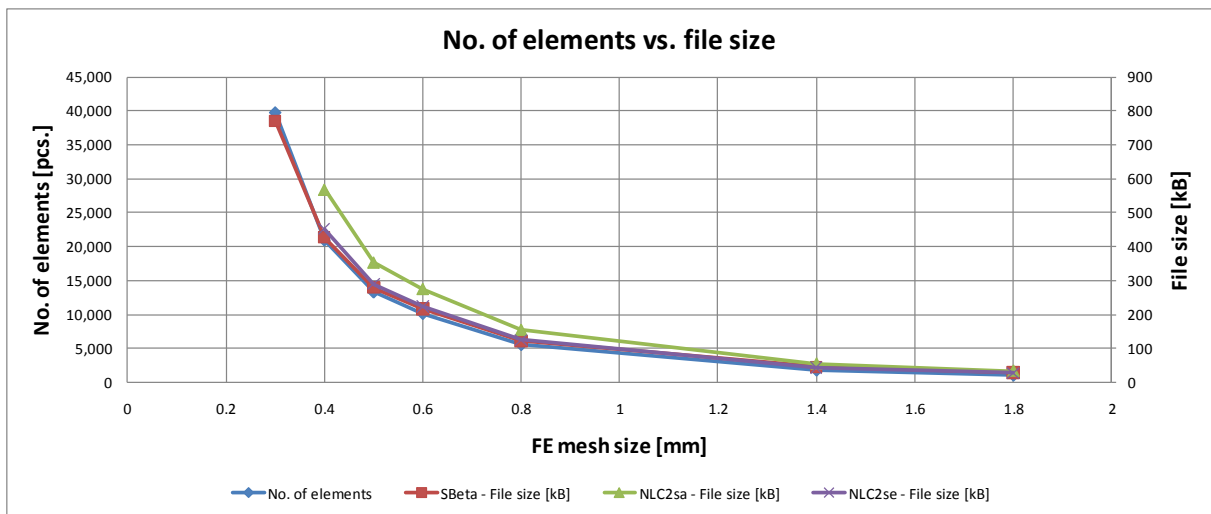
FE mesh size of concrete part, number of mesh elements and file size were taken from Table 7-6 and Table 7-7 and plotted on the graph shown in Figure 7-5. In the graph the horizontal axis indicates FE mesh size of concrete part, the vertical axis on the left shows number of mesh elements and the vertical axis on the right represents file size. It can be observed that number of mesh elements and file size are growing exponentially with respect to the finite element size of the concrete part. Considering that the plotted curves are overlapping it can be concluded that the rise in number of mesh elements is directly proportional to the rise in file size.

**Table 7-8 : Generated mesh for XX\_es05\_5x5 specimen**

Whole specimen	Magnified upper part	Magnified bottom part
 <p data-bbox="300 734 459 768">XX_es05_5x5</p>		

XX = SBeta or 3D Non Linear Cementitious 2 material model

In the post-processing, the data recorded from monitors were imported with help of macros, used in Load Results workbook, created in software Microsoft Excel (for more details about created macros, see subsection 9.2.1). Data were plotted on the graphs where the horizontal axis indicates displacement of upper loading prism and the vertical axis shows the imposed load. Figure 7-7 shows the L–D curves for SBeta specimens. If we exclude two simulations with coarsest mesh size of concrete part (SBeta\_es18\_15x15 and SBeta\_es14\_15x15), it is possible to observe that simulation results are very much alike. Imposed load reaches a peak (between 10 and 11 kN) at displacement of approximately 0.04 mm and then starts to decline. The reason for this decline was explained in the previous subsection and is not going to be repeated again for any of subsequent graphs.



**Figure 7-5 : Number of elements versus file for used specimens**

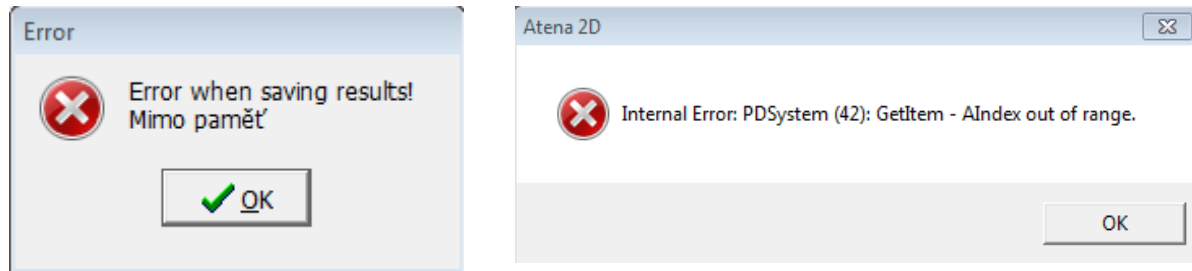


Figure 7-6 : Error warnings during execution of NLC2\_es03\_3x3 simulations

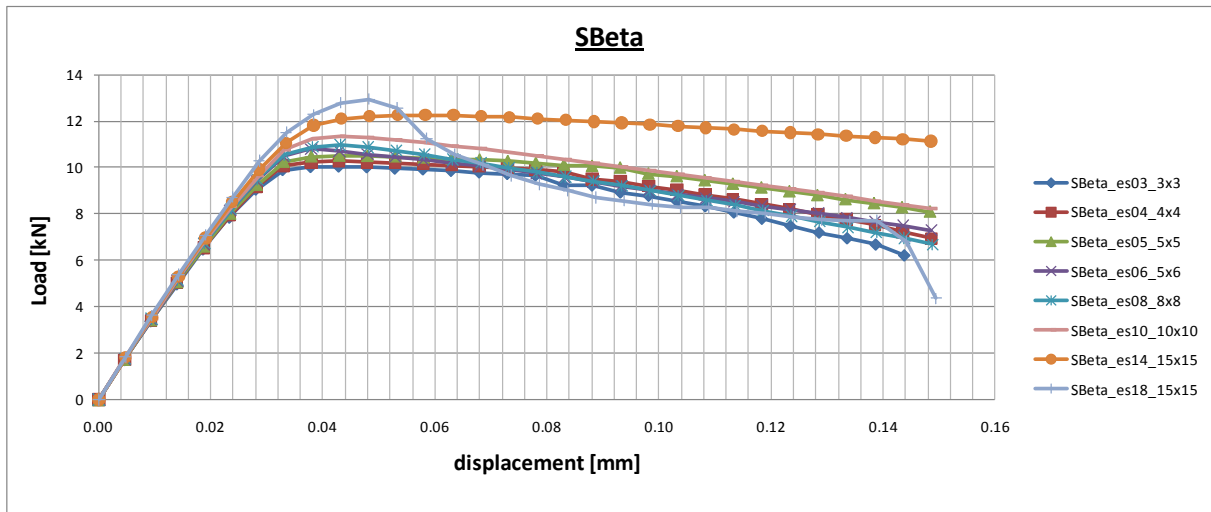


Figure 7-7 : Load–displacement curves for SBeta specimens

Subsequent Figure 7-8 shows L–D curves for NLC2sa specimens. As can be seen the simulation NLC2sa\_es04\_4x4 shows steeper decline than the remaining simulations. Imposed load reaches a peak (15 kN) at displacement just about 0.05 mm (with the exception of NLC2sa\_es08\_8x8 – displacement roughly 0.04 mm and imposed load close to 14kN; NLC2sa\_es14\_15x15 – displacement just about 0.05 mm and imposed load close to 16kN). On the whole, L–D curves do not differ very much.

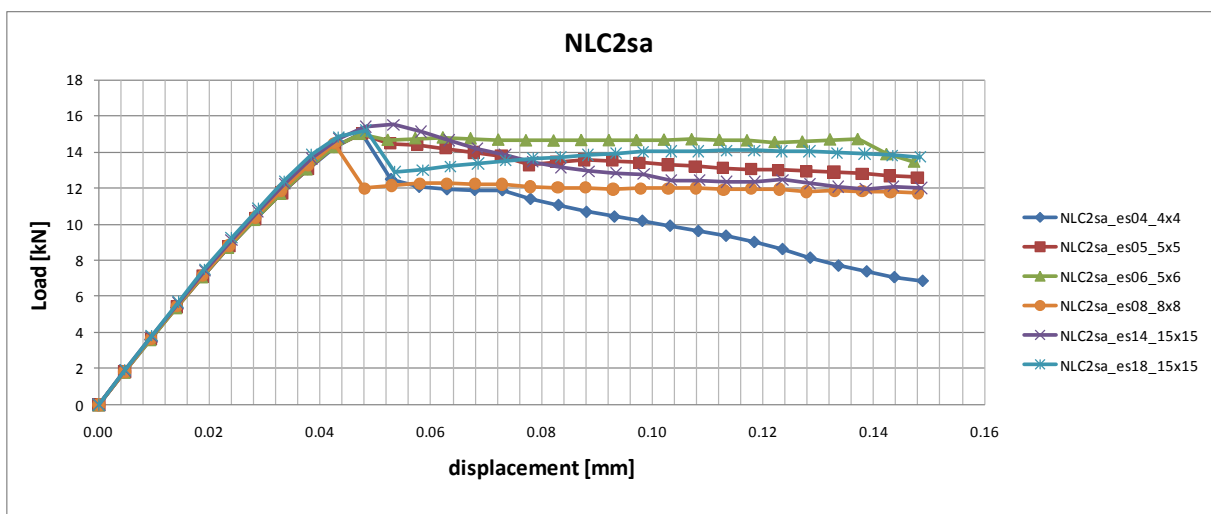


Figure 7-8 : Load–displacement curves for NLC2sa specimens

L–D curves for NLC2se specimens are displayed in Figure 7-9. It is convenient to exclude two simulations with coarsest mesh size of concrete part (NLC2se\_es18\_15x15 and NLC2se\_es14\_15x15) because these simulations have significantly different L–D curve shapes and finer mesh should give more precise results. Remaining simulations slightly differ in the L–D curve shapes after they reach the imposed load peak (around 11 kN; displacement roughly 0.05 mm).

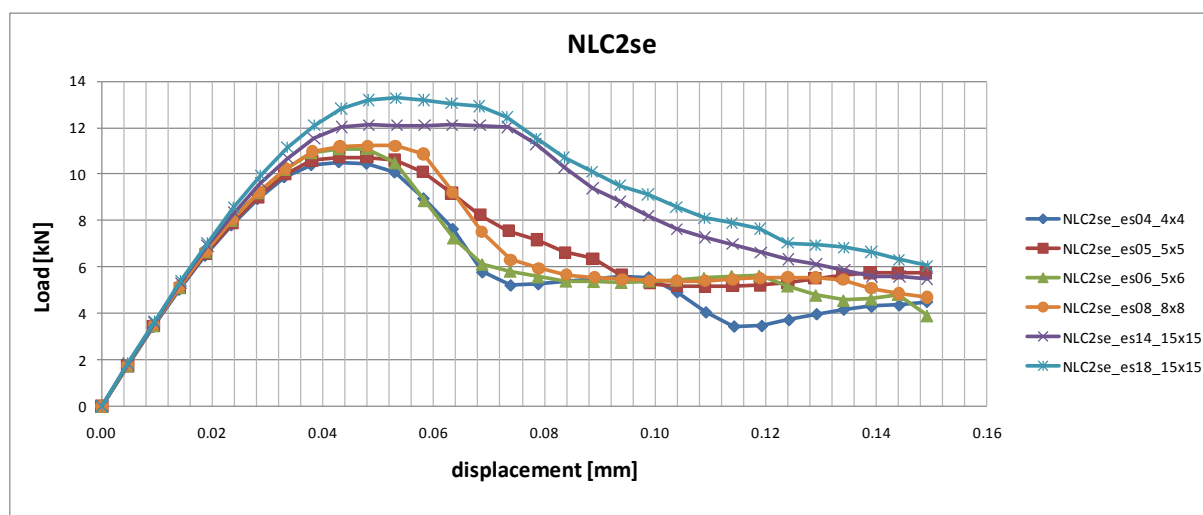


Figure 7-9 : Load–displacement curves for NLC2se specimens

Crack width and Principal Fracture Strain (PFS) were other outputs compared in post-processing, representing calculated total crack opening displacement and principal fracturing strain within finite element (for more details about principal fracturing strain, see subsection 6.5.1), respectively. The material model SBeta offers only Crack width output therefore Table 7-9 contains just maximal Crack width in elements at peak point of L–D curve and one step after peak point. It can be observed that maximal Crack width grows with increasing element size and therefore the Crack width is dependent on the FE mesh density. Crack patterns listed in the Appendix A 4 or examples of crack pattern for SBeta\_es04\_4x4 and SBeta\_es08\_8x8 (Table 7-11) confirm the dependency on the FE mesh.

Table 7-9 : Crack width SBeta specimens

Specimen	Load step no. (peak)	Max. Crack width(in elements)		Load step no. (after peak)	Max. Crack width(in elements)	
		[m]	[mm]		[m]	[mm]
SBeta_es03_3x3	9	4.727E-07	0.00047	10	7.446E-07	0.00074
SBeta_es04_4x4	9	4.940E-07	0.00049	10	5.409E-06	0.00541
SBeta_es05_5x5	9	2.331E-06	0.00233	10	3.918E-06	0.00392
SBeta_es06_5x6	8	3.981E-06	0.00398	9	5.868E-06	0.00587
SBeta_es08_8x8	9	8.444E-07	0.00084	10	4.504E-06	0.00450
SBeta_es14_15x15	12	5.053E-06	0.00505	13	6.198E-06	0.00620
SBeta_es18_15x15	10	6.239E-06	0.00624	11	2.306E-05	0.02306

The 3D Non Linear Cementitious 2 material model offers as Crack width output as PFS output. Maximal Crack width and maximal PFS (both in elements) at peak point of L–D curve and one step after peak point are listed in Table 7-10. In the case of PFS, difference between maximal PFS among specimens with different FE mesh size of concrete part is smaller than in the case of Crack width. As an example, difference in maximal PFS at peak point of L–D curve between NLC2sa \_es04\_4x4 and NLC2sa \_es05\_5x5 is 1.307 (larger maximal PFS is numerator, lesser is denominator and the quotient is the obtained difference) and for Crack width is 1.607 (same rule as for PFS). This fact is generally true for most of listed specimens (= difference in PFS among specimens is smaller than in Crack width). Additionally, maximal Crack width for NLC2se \_es06\_5x5 has value larger of more than two orders of magnitude in comparison with remaining specimens and on the contrary, PFS for this specimen does not have such divergence. For above mentioned reasons and because PFS is dimensionless quantity (unit of Crack width is metre) it was made a decision to preferably use PFS output in order to describe and locate cracks in specimens in further studies.

**Table 7-10 : Crack width and PFS NLC2 specimens**

Specimen NLC2	Load step no. (peak)	Max. Crack width (in elements)		Max. PFS (in elements)	Load step no.	Max. Crack width (in elements)		Max. PFS (in elements)
		[m]	[mm]	[-]		[m]	[mm]	[-]
sa_es03_3x3	-	-	-	-	-	-	-	-
se_es03_3x3	-	-	-	-	-	-	-	-
sa_es04_4x4	10	2.476E-07	0.00025	6.188E-04	11	2.037E-05	0.02037	2.617E-02
se_es04_4x4	9	8.688E-07	0.00087	1.519E-03	10	1.093E-06	0.00109	2.370E-03
sa_es05_5x5	10	4.045E-07	0.00040	8.086E-04	11	4.569E-06	0.00457	9.026E-03
se_es05_5x5	10	7.456E-07	0.00075	1.621E-03	11	9.285E-07	0.00093	2.395E-03
sa_es06_5x6	10	5.948E-07	0.00059	9.908E-04	11	4.548E-06	0.00455	7.517E-03
se_es06_5x6	10	1.356E-04	0.13560	6.160E-03	11	2.416E-04	0.24160	1.116E-02
sa_es08_8x8	9	6.500E-08	0.00007	4.265E-05	10	2.057E-05	0.02057	1.302E-02
se_es08_8x8	10	1.314E-06	0.00131	8.248E-04	11	1.683E-06	0.00168	1.290E-03
sa_es14_15x15	11	4.655E-06	0.00466	3.313E-03	12	7.824E-06	0.00782	5.557E-03
se_es14_15x15	13	1.352E-06	0.00135	7.382E-04	14	1.600E-06	0.00160	9.323E-04
sa_es18_15x15	10	4.413E-06	0.00441	2.385E-03	11	2.646E-05	0.02646	7.791E-03
se_es18_15x15	11	1.765E-06	0.00177	1.036E-03	12	3.021E-06	0.00302	1.773E-03

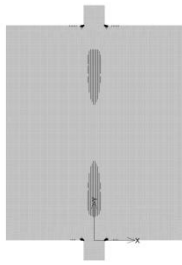
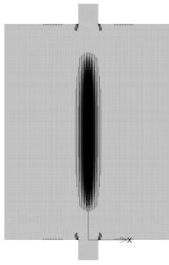
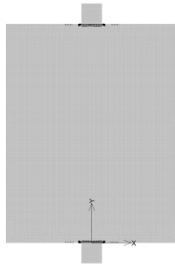
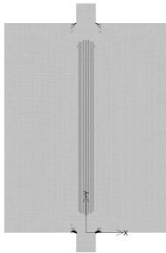
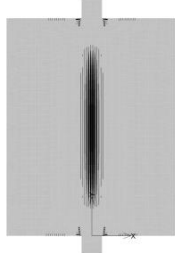
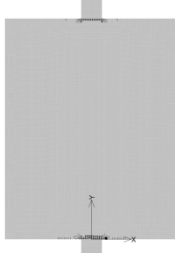
To sum up the above, this study examined the role of the mesh density and found out that the element size of concrete part affects results of imposed load. Furthermore, mesh refinement has impact on maximal Crack width and maximal PFS but the impact on maximal PFS is smaller, therefore it was made a decision to use preferably PFS output in further studies.



### 7.1.3 Material model

For a study of the material model influence, the specimens described in the previous subsection were used. The labelling was preserved thus the legend can be found in the previous subsection and is not introduced again. Table 7-11 shows crack pattern for two different FE mesh sizes. It is obvious at first glance that crack pattern among materials differs a lot, especially NLC2se (3D Non Linear Cementitious 2 material model modelled in the state of plain stress) has almost no cracks indicating tensile splitting and thus the model NLC2se was stated as inappropriate for the modelling of the experimentally observed failure phenomenon. Deeper observation of other examples listed in the Appendix A 4 shows that SBeta and NLC2sa indicate similarities in range of failure, primarily among models with FE mesh size of concrete part equal to 0.5 or 0.6 mm (\_es05\_5x5 or \_es06\_5x5) and therefore mainly these models were used for comparison of cracks location where computed crack related outputs are compared with failure related events recorded by the acoustic emission (AE). Detailed information concerning the AE can be found in the subsection 4.1.

**Table 7-11 : Crack pattern for \_es04\_4x4 and \_es08\_8x8 specimens**

Loading step no.9 (peak)	Loading step no.10 (peak)	Loading step no.9 (peak)
 <p>SBeta_es04_4x4</p>	 <p>NLC2sa_es04_4x4</p>	 <p>NLC2se_es04_4x4</p>
Loading step no.8 (peak)	Loading step no.10 (peak)	Loading step no.10 (peak)
 <p>SBeta_es06_5x6</p>	 <p>NLC2sa_es06_5x6</p>	 <p>NLC2se_es06_5x6</p>

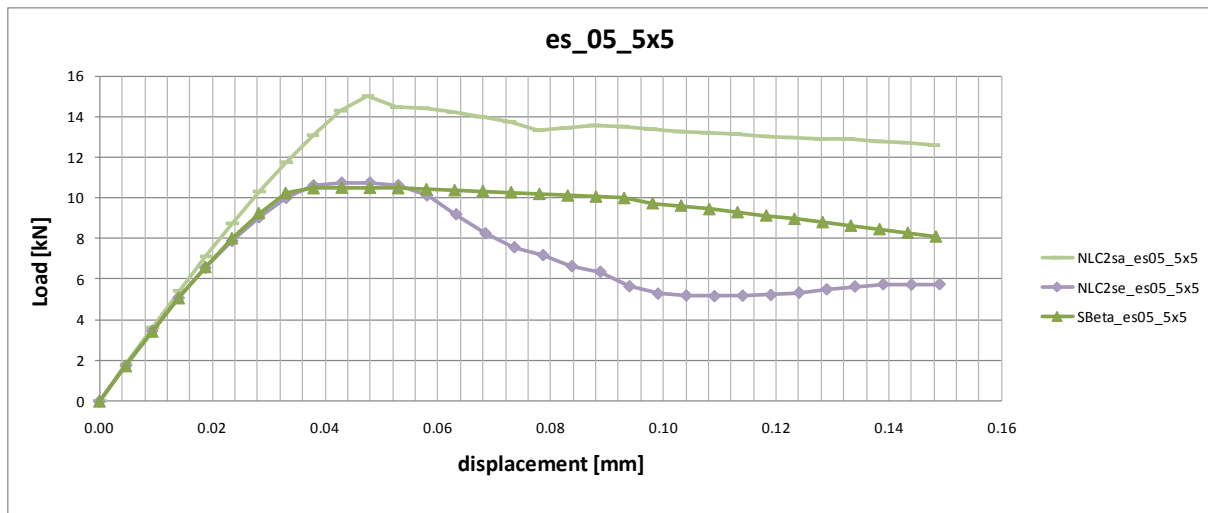


Figure 7-10 : Load–displacement curves for \_es\_05\_5x5 specimens

The figure Figure 7-10 shows a trend that can be observed in all other figures listed in the Appendix A 5. From the trend it follows, that the L–D curves for SBeta and NLC2se materials reach imposed load peak at same value but they descend differently. SBeta has very flat curve that does not come down so rapidly as NLC2se curve. The NLC2sa material has imposed load peak reaching value about four thirds of value common for SBeta and NLC2se materials and its peak is followed by sharp, short jump changing into flat descending part of curve. The stiffness of models for descending part of curve seems to be too high for concrete specimen loaded by two steel prisms which are causing that specimen fails by tensile splitting which is accompanied by rapid, long fall of imposed load as shown in Figure 7-11. Such fall, but not so rapid, was exhibited only by NLC2 material models. As mentioned before, NLC2se was stated as inappropriate for modelling of tensile splitting (no cracks indicating tensile splitting) therefore NLC2sa was stated as more suitable for simulations of tensile splitting than NLC2se or SBeta.

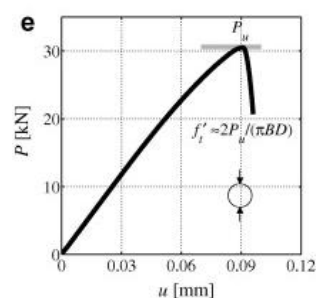
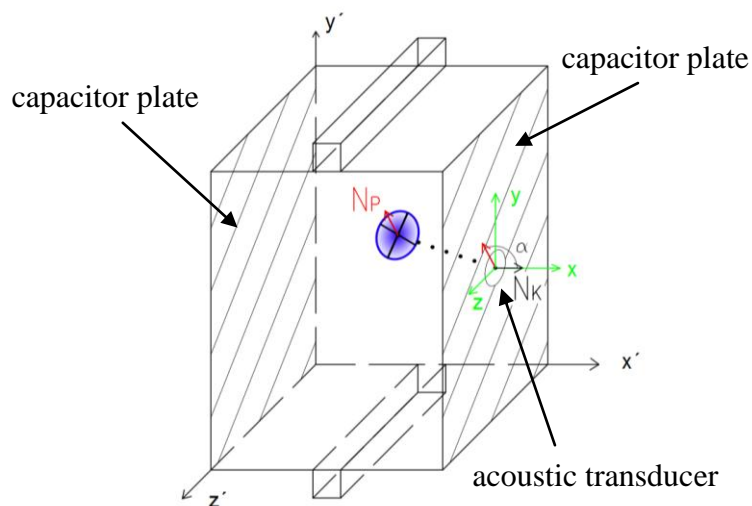


Figure 7-11 : Example of load–displacement curve for splitting test. Adopted from [45].

## 7.2 Failure location in 2D (AE + EME)

Experimental tests performed on the specimens in configuration BII (Figure 5-3) recorded acoustic and electromagnetic emissions that are accompanying fracture events during loading of the specimens. Fracture events trigger the release of energy in the form of acoustic waves (AE) and electromagnetic field (EME). Combination of the AE and EME provides data that can be used for location of fracture events. Experimental data were recorded by dual channel apparatus (one channel for the AE, one for the EME). This subsection compares experimental data with results obtained from numerical simulations using models described and commented in the previous subsection.

In the experiment, there was only one acoustic transducer placed in the middle of one specimen side (Figure 7-12). Parallel plate capacitor, essential component for the EME measurements, consisted of two parallel plates and dielectric (formed by the concrete specimen) in between. Disadvantage of the EME measurements is the fact that the capacitor plates are capable to record only fracture events (cracks) that are spreading parallel to them. It means that all fracture events spreading perpendicularly to the capacitor plates are not recorded, fracture events spreading parallel to the capacitor plates are entirely recorded and it is not entirely clear what kind of fracture events or how many of them are recorded when the angle between them and capacitor plates lies in interval  $(0^\circ, 90^\circ)$ . Figure 7-12 shows the specimen BII surrounded by two capacitor plates (hatched parts).

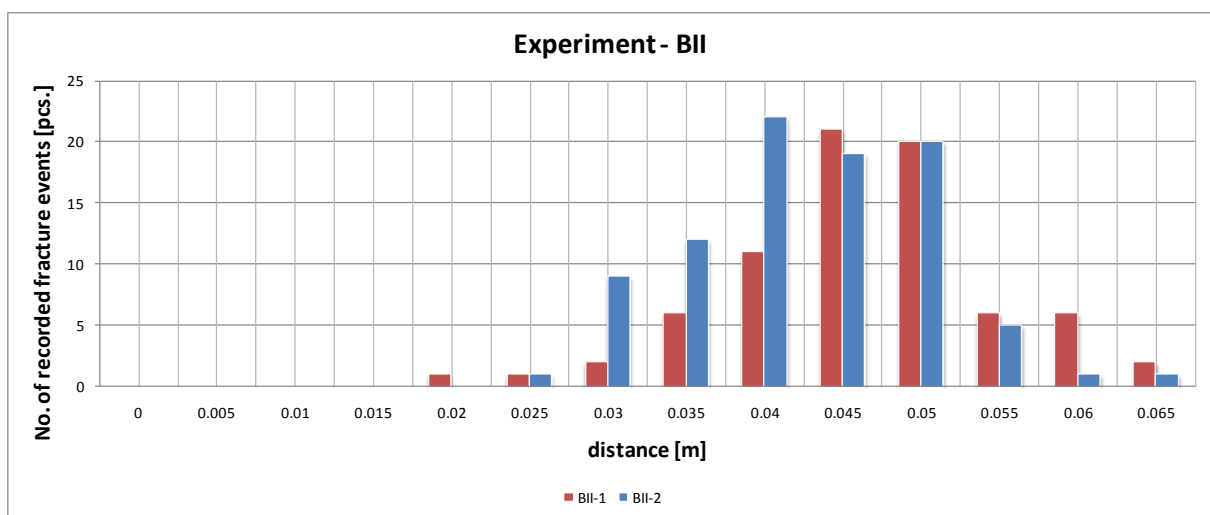


**Figure 7-12 : Scheme of specimen BII showing the determination of the spatial angle  $\alpha$  between the normal vector of a plane of a forming crack and the normal vector of the capacitor's plate**

Location of fracture events was based on a principle that the EME propagates with the speed of light (approximately 300,000,000 m/s) and the AE propagates slower (3,925 m/s;

measured on concrete specimens used in this thesis). The time lag between onset of the EME signal and the AE signal enables to calculate the distance (marked in Figure 7-12 with dotted line) between the centre of fracture event and acoustic transducer. This form of location has one major disadvantage. The calculated distance does not include information concerning the direction therefore it was possible to locate fracture events only on concentric hemispheres (in 3D space) or concentric semicircles (in 2D space) with the centre at acoustic transducer. In other words, it is impossible to precisely locate fracture events, it is only possible to set the diameter (= calculated distance) of hemisphere (3D) or semicircle (2D) and say that the fracture event is located somewhere on the surface (hemisphere) or on the circumference (semicircle).

The calculated distances for two tested specimens in the configuration BII are shown in Figure 7-13. Horizontal axis shows the intervals including distances between the centre of fracture events and acoustic transducer (the displayed number indicates the upper endpoint of the interval, e.g. 0.035 represents distances in interval (0.03, 0.035], 0.04 represents interval (0.035, 0.04] and so on; intervals are tabulated in Table 7-12) and the vertical axis shows the number of recorded fracture events. Total number of recorded fracture events was 76 for specimen BII-1 and 90 for specimen BII-2. As can be observed, the most of fracture events are concentrated in intervals 0.04, 0.045 and 0.05.



**Figure 7-13 : Histogram for BII specimens showing distance between fracture event and acoustic transducer**

Data already computed and imported for parametric studies, which were analysed in the previous subsection, were used for post-processing. Additionally, to the already loaded data, Integration point (IP) coordinates were imported, again, with help of macros used in Load Results workbook created in software Microsoft Excel (for more details about created

macros, see subsection 9.2.1). Another Excel workbook named Filtered PFS was utilised to assign IP coordinates to the corresponding PFS in order to be able to locate principal fracture strains. PFS at each integration point were filtered by various threshold filter values (ranging between  $1 \times 10^{-4}$  and  $1 \times 10^{-9}$ ) in order to investigate the sensitivity of the examined experimental method. Values exceeding a chosen threshold were taken into account as fracture event. Subsequently, distance between the acoustic transducer and fracture event (represented by PFS) was calculated as vector length according to the formula given below.

$$\|\mathbf{d}\| = \sqrt{(x_T - x_P)^2 + (y_T - y_P)^2} \quad (7.1)$$

where  $\|\mathbf{d}\|$  is the length or magnitude or norm of the vector  $\mathbf{d}$ ,

$x_T$  is the transducer position in the  $x$  direction,

$x_P$  is the PFS position in the  $x$  direction,

$y_T$  is the transducer position in the  $y$  direction,

$y_P$  is the PFS position in the  $y$  direction.

Obtained distances were classified into intervals and the intervals together with their representative values (= values shown on horizontal axis in the graph) can be found in Table 7-12. Quantities of fracture events in the individual intervals were subsequently divided by the total number of fracture events. This step brings the possibility to compare computed data with the experimental one because the obtained relative frequency is independent on number of events (of course, this is only true if the number of events is not too low; at least several tens are necessary) and the trend, representing how the fracture events are distributed, can be shown.

**Table 7-12 : Intervals for classification of distances between the centre of fracture events and acoustic transducer**

Interval	(0,0.005]	(0.005,0.01]	(0.01,0.015]	(0.015,0.02]	(0.02,0.025]
Value on the horizontal axis in the graph	0.005	0.01	0.015	0.02	0.025
Interval	(0.025,0.03]	(0.03,0.035]	(0.035,0.04]	(0.04,0.045]	(0.045,0.05]
Value on the horizontal axis in the graph	0.03	0.035	0.04	0.045	0.05
Interval	(0.05,0.055]	(0.055,0.06]	(0.06,0.065]		
Value on the horizontal axis in the graph	0.055	0.06	0.065		

As from the parametric studies follows (described in the previous subsection), the most suitable material model for numerical simulation should be NLC2sa with FE mesh size of concrete part equal to 0.5 or 0.6 mm ( $_{es05\_5x5}$  or  $_{es06\_5x5}$ ), therefore three specimens (NLC2sa  $_{es04\_4x4}$ , NLC2sa  $_{es05\_5x5}$  and NLC2sa  $_{es06\_5x6}$ ) were chosen for comparison of their PFS location with the experimental location of fracture events. The PFS outputs were processed for 10<sup>th</sup> (= peak point of L–D curve) and 11<sup>th</sup> analysis step and distances cal-

culated for these steps were plotted against relative frequencies on the graphs where the horizontal axis indicates intervals including distances and the vertical axis shows the relative frequency.

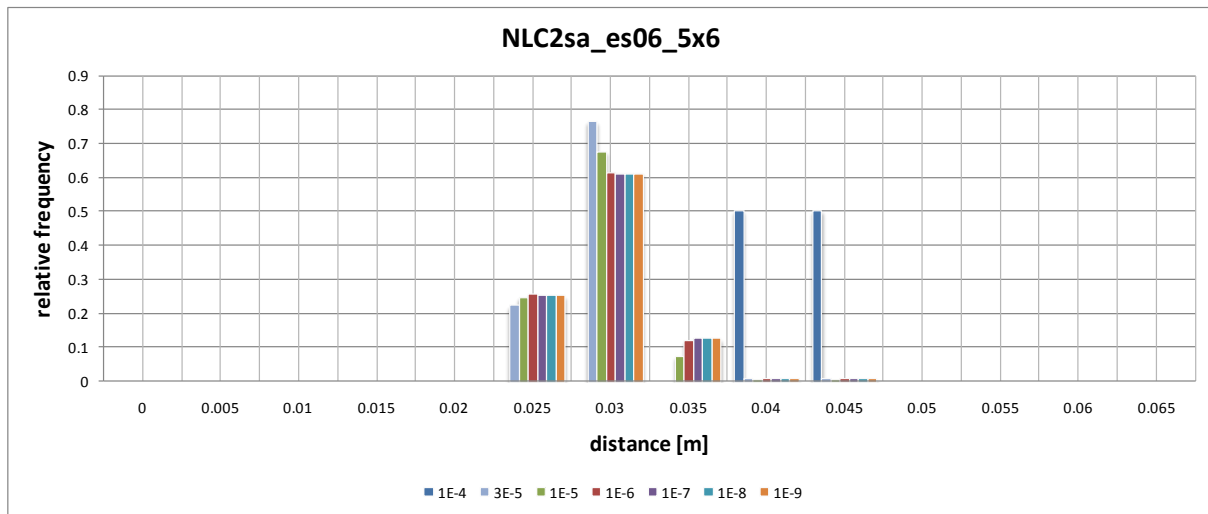


Figure 7-14 : Distances filtered by various filters – NLC2sa\_es06\_5x6 specimen

In order to find out how the threshold filter values for PFS influence the relative frequencies, relative frequencies for specimen NLC2sa\_es06\_5x6 were plotted against distances including applied filters (ranging between  $1 \times 10^{-4}$  and  $1 \times 10^{-9}$ ) on the graph in Figure 7-14. As can be observed the most of fracture events are concentrated in interval 0.03 what is in contrast with experimental histogram in Figure 7-13 where the most of fracture events are concentrated around interval 0.045. Only filter 1E-4 seems to have fracture events placed around interval 0.045, however, from the Table 7-13, showing applied filter values, it follows that the number of fracture events is only 12 and that is too low to trust the trend.

Table 7-13 : Filters applied to NLC2sa\_es06\_5x6 specimen

	Applied filter						
	1E-4	3E-5	1E-5	1E-6	1E-7	1E-8	1E-9
No. of fracture events	12	1250	2410	3053	3096	3096	3096

The specimen NLC2sa\_es05\_5x5 was chosen for presentation of results that are displayed in Figure 7-15 (histograms for other specimens can be found in the Appendix A 6). Histogram supports the fact already observed in Figure 7-14 that the most of fracture events are concentrated in interval 0.03 what is in contrast with experimental histogram. Figure 7-16 shows that there is almost no difference between relative frequencies when the FE mesh size of concrete part changes. Results are shown for 10<sup>th</sup> analysis step (peak point of L–D curve) and other results for 11<sup>th</sup> analysis step can be found in the Appendix A 6 showing practically the same behaviour.

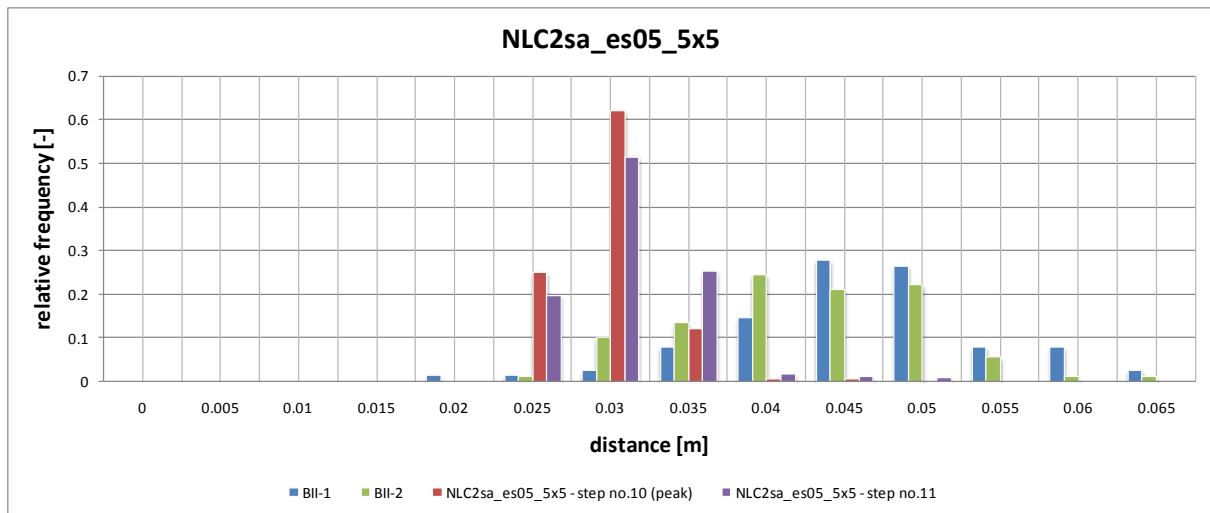


Figure 7-15 : Distances of fracture events for specimen NLC2sa\_es05\_5x5

### 7.3 Conclusion

The conclusion to this whole section is that the 2D simulations are not capable to capture fracture events because the failure occurs in 3D space and 2D simplification does not adequately count with the third dimension. In other words, 2D representation is something like a slice cut out from 3D object and therefore the calculated distances between the acoustic transducer and the centre of fracture event are loaded by error causing shift in distance in which is the highest occurrence of fracture events. It is obvious that the 3D simulations have to be conducted in order to be able to compare experimental fracture events with the computed PFS. The next section deals with 3D simulations.

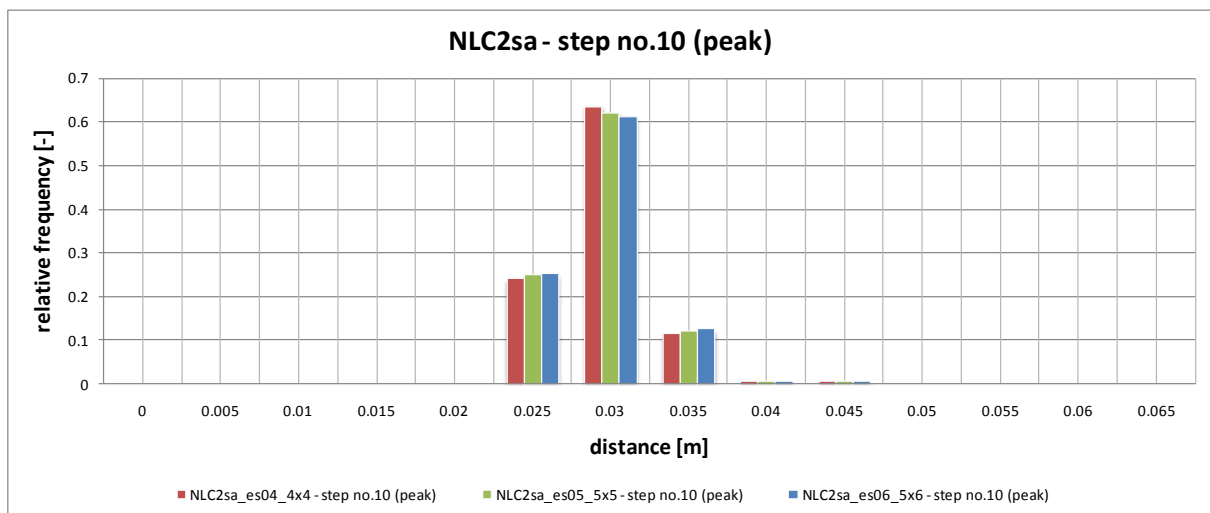


Figure 7-16 : Distances of fracture events for specimens NLC2sa at step no.10 (peak point of L-D curve)

## 8 Simulations in ATENA 3D

The reason for the simulations in 3D space was the fact (already described in the previous section) that 2D simulations are not capable to adequately capture fracture events arising in the configurations used for experimental specimens. Numerical models were created in the software ATENA 3D which is a three-dimensional version of the software ATENA 2D.

Geometry, boundary conditions and way of loading of experimental specimens used for simulations in this section are described sufficiently in the section 5. This section ,8 , includes description of numerical models representing experimental specimens.

Import of results of all simulations performed in ATENA 3D to software Microsoft Excel was realised through Import of data workbook (described in detail in the subsection 9.2.2). Subsequently, the imported data were post-processed in the Fracture strain 3D workbook (described in detail in the subsection 9.2.3).

Unless stated otherwise, FE size for all 3D simulations was set to 3 mm (set One) and 4mm (set Two), based on the mesh studies presented in ATENA Example Manual [46], and the used linear finite element mesh type was tetrahedron for the loading pyramid and brick for the rest of the model. Linear finite elements are low-order polynomial shape function elements with nodes placed at the element corners only.

It is important to note, that all simulations conducted in ATENA 3D are denoted with prefix "3D" (e.g. 3D\_BII denotes results of numerical simulation performed on the specimen configuration BII in ATENA 3D). Specimens without prefix "3D" are the experimental ones (e.g. BII denotes experimental results of the configuration BII). The simulation labels consist of prefix "3D" separated by the underscore "\_" with appended label for the configuration (e.g. AI, R4K\_III\_CC (described in detail in the subsection 5.3)), separated by the underscore "\_" with appended expression "step" followed by number (= single or double digit number) representing the  $i$ -th analysis step and once more separated by the underscore "\_" with appended expression that represents an applied filter (e.g. 1E-4) on the values of analysed PFS. It is important to note that the label do not have to include all above mentioned expression (e.g. 3D\_BII).

As an illustration 3D\_BII\_step15\_5E-5 denotes the specimen of configuration BII conducted in ATENA 3D, the results were taken from the 15<sup>th</sup> analysis step and the PFS at each integration point were filtered by threshold filter value  $5 \times 10^{-5}$ .



All load–displacement (L–D) curves were plotted on the graphs where the horizontal axis indicates displacement in the middle of the bottom surface of the upper loading prism and the vertical axis shows the imposed load.

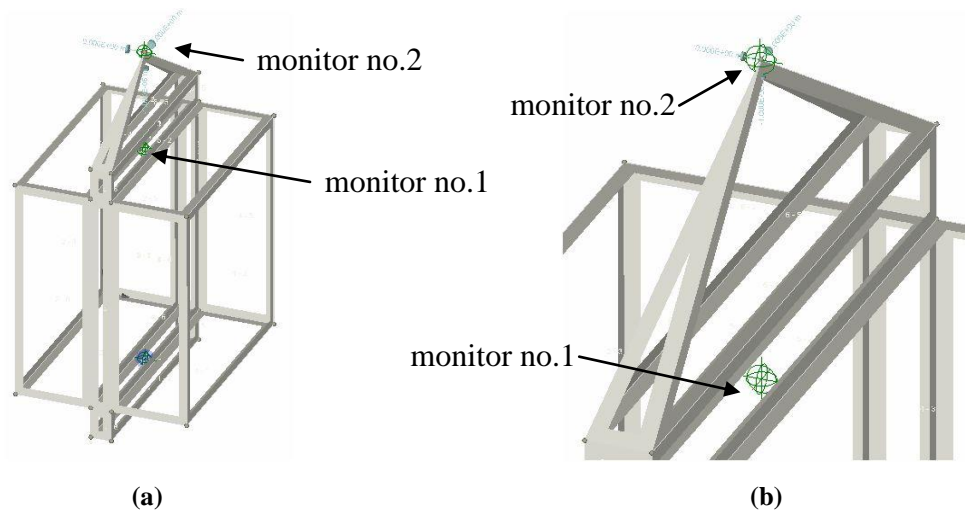
In order to keep this master thesis concise, only brief description of conducted simulations is provided in this section. And that is done in spite of the fact, that these simulations were the most time consuming activity.

## 8.1 Specimen set One

Simulations performed on the set One included three different configurations AI, AII and BII that are described in the section 5 and pictured in Figure 5-1, Figure 5-2 and Figure 5-3, respectively. Basic information concerning this study was published in paper [51].

Figure 8-1 shows location of monitor no.1 and no.2, recording magnitude of the vertical displacement of the loading prism and the applied force, respectively. In the models, the bottom jaw of testing machine was fixed in all directions, the upper one was fixed axially in a single point of the loading pyramid simulating the upper testing machine jaw (AI) and the bottom loading prism was fixed in all directions and the upper one was fixed in one point similarly to the mentioned case (AII and BII). The loading by increment of vertical displacement in the apex of the loading pyramid was carried out along  $y$ -axis (orientation of axes is depicted in Figure 5-10 (a)). The loading pyramid (Figure 8-1 (b)) was used to enable recording of the magnitude of applied force (i.e reaction to the imposed displacement increment) without need of integration of this force over certain area, because the displacement increment was applied directly to a point (i.e. the apex of loading pyramid). There were used 20 incremental steps (AII and BII) or 40 incremental steps (AI) each with value of  $1 \times 10^{-5}$  m and the Newton-Raphson solution method was applied in all analysis steps.

Applied material model for the concrete part of the model was the 3D Non Linear Cementitious 2 with default values calculated by the program for concrete with cube strength  $f'_{cu} = 25$  MPa. Value of elastic modulus and special material weight was modified according to the material parameters specified in paper [44] which describes material parameters for the specimen set One. 3D Elastic Isotropic material model with elastic modulus  $E = 210$  GPa corresponding to plain mild steel was used for steel loading prisms and jaws of testing machine. The same material model was used for the loading pyramid, but with thousand times higher elastic modulus (i.e.  $E = 210\,000$  GPa) in order to be sure that the loading pyramid is stiffer than the rest of model and is therefore able to keep the simulated upper jaw of testing machine planar. All relevant parameters of the material models are listed in Table 8-1.



**Figure 8-1 : Monitors and prescribed displacement of set One – (a) Total view, (b) Magnified upper part of specimen**

**Table 8-1 : Relevant parameters of material models**

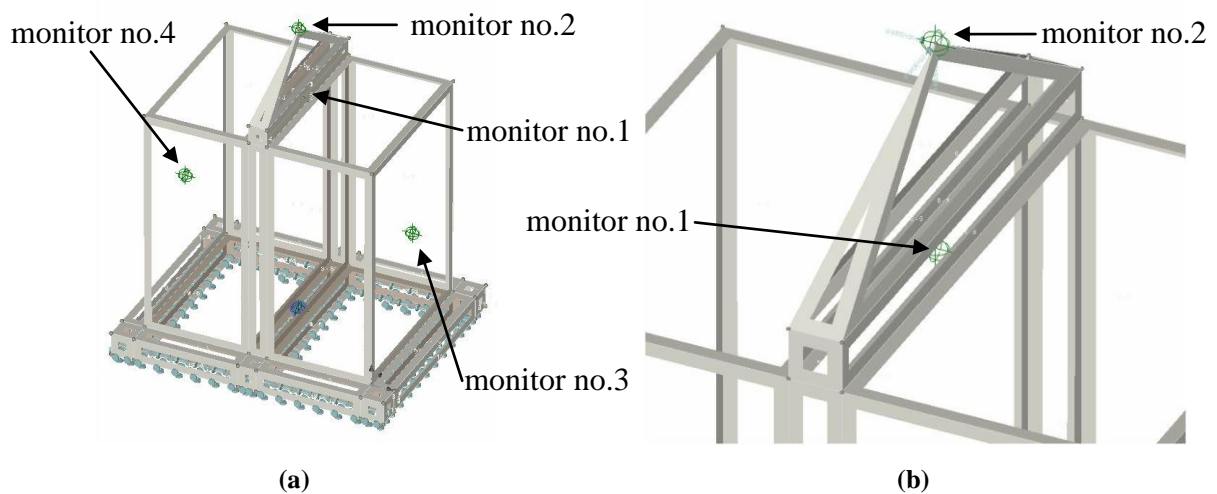
	Material model		
	3D Non Linear Cementitious 2	3D Elastic Isotropic (jaw of testing machine, loading prism)	3D Elastic Isotropic (loading pyramid)
Elastic modulus $E$ [MPa]	20 000	210 000	210 000 000
Poisson's ratio $\nu$ [-]	0.200	0.300	0.300
Specific material weight $\rho$ [MN/m <sup>3</sup> ]	2.230E-02	7.850E-02	7.850E-02
Tensile strength $f_t$ [MPa]	2.052		
Compressive strength $f_c$ [MPa]	-21.250		
Specific fracture energy $G_f$ [MN/m]	5.130E-05		
Fixed crack model coefficient	0.5		
Critical compressive displacement $w_d$ [m]	-5.000E-04		

## 8.2 Specimen set Two

Simulations performed on the set Two included three different configurations CC, 1C and 2C that are described in the section 5 and pictured in Figure 5-4, Figure 5-5 and Figure 5-6, respectively.

Figure 8-2 shows location of monitor no.1, 2, 3 and 4 recording magnitude of vertical displacement, applied force, horizontal displacement (displacement perpendicular to the specimen side) of a specimen side lying in the  $x$ - $y$  plane and horizontal displacement of the opposite side, respectively. In the models, the bottom jaw of testing machine was fixed in all directions, the upper one was fixed axially in a single point of the loading pyramid simulating the upper testing machine jaw (CC), the bottom jaw of testing machine was fixed in all direc-

tions, the upper one was fixed axially in a single point of the loading pyramid simulating the upper testing machine jaw (1C) and the bottom loading prism was fixed in all directions and the upper one was fixed in one point similarly to the mentioned cases (2C). The loading by increment of vertical displacement in the apex of loading pyramid was carried out along  $y$ -axis (orientation of axes is depicted in Figure 5-10 (a)). The loading pyramid (Figure 8-2 (b)) was used to record magnitude of applied force without need of integration of this force over certain area, because the force was applied directly to a point (i.e. the apex of loading pyramid). There were used 80 incremental steps each with value of  $1 \times 10^{-5}$  m and the Newton-Raphson solution method was applied in all analysis steps.



**Figure 8-2 : Monitors and prescribed displacement of set Two – (a) Total view, (b) Magnified upper part of specimen**

Applied material model for concrete part was the 3D Non Linear Cementitious 2 with default values calculated by the program for concrete with cube strength  $f'_{cu} = 25$  MPa (Unless stated otherwise). Value of elastic modulus and specific material weight was modified according to the material parameters specified in paper [44], unless stated otherwise. 3D Elastic Isotropic material model with elastic modulus  $E = 210$  GPa corresponding to plain mild steel was used for steel loading prisms and jaws of testing machine. The same material model as in specimen set One was used for the loading pyramid. Unless stated otherwise, all relevant parameters of the material models are listed in the Table 8-1.

### 8.3 Failure location in 3D (AE + EME)

The failure location analysis details in 2D are described in the subsection 7.2. The post-processing of the results in 3D is described in detail in the subsection 9.2.3 and therefore is not given here. The time lag between onset of the EME signal and the AE signal enables to

calculate the distance (marked in Figure 7-12 with dotted line) between the centre of fracture event and acoustic transducer. The calculated distances for the tested specimens are shown in the following graphs. Horizontal axis shows the intervals including distances between centre of fracture events and acoustic transducer (the displayed number indicates the upper endpoint of the interval, e.g. 0.035 represents distances in interval (0.03, 0.035], 0.04 represents interval (0.035, 0.04] and so on; intervals are tabulated in Table 7-12) and the vertical axis shows the relative frequency of the recorded fracture events.

### 8.3.1 Configuration BII

Figure 8-3 shows comparison of L–D curves of simulations conducted in ATENA 2D and 3D for configuration BII. This confirms the hypothesis stated in the subsection 7.1 that the 3D Non Linear Cementitious 2 material model in the state of plane strain (denoted as NLC2sa) is more suitable for simulations of tensile splitting than NLC2se or SBeta material model because the shape of NLC2sa curve is very similar to the shape of 3D\_BII curve. The same behaviour can be observed on L–D curves for other simulations listed in the Appendix A 7.

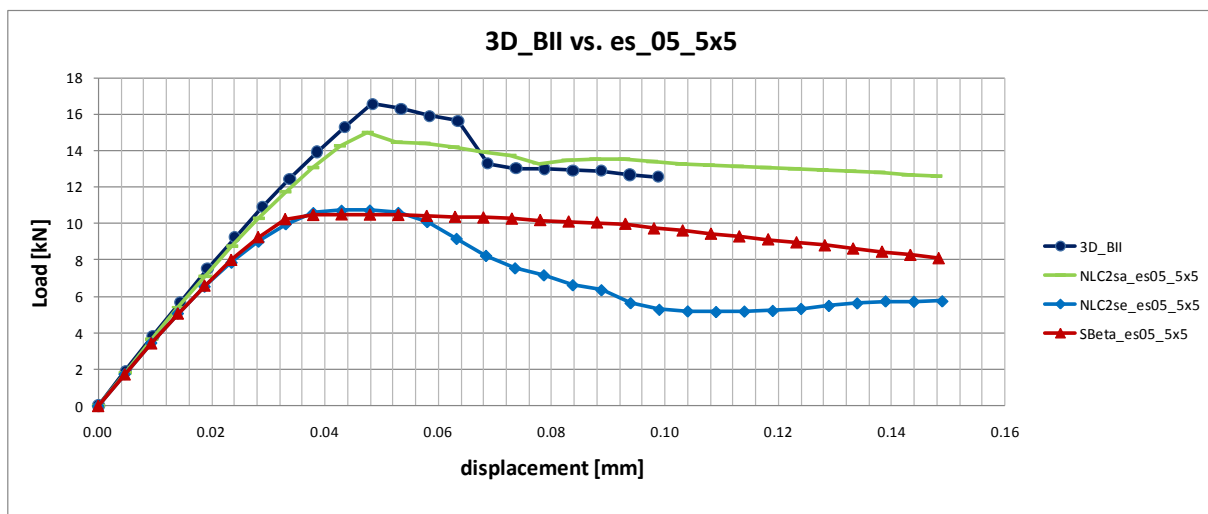


Figure 8-3 : Load–displacement curves – 3D\_BII vs. es\_05\_5x5

The PFS outputs were processed for 10<sup>th</sup> (= peak point of L–D curve), 11<sup>th</sup>, 13<sup>th</sup> and 15<sup>th</sup> analysis step and distances calculated for these steps were plotted against relative frequencies on the graphs where the horizontal axis indicates intervals including distances and the vertical axis shows the relative frequency. The best results were obtained from the simulation 3D\_BII\_step15\_5E-5, as can be observed in Figure 8-4, because its curve corresponds most closely to the curve of experimental results BII-2. The graphs for 10<sup>th</sup> (= peak point of L–D curve), 11<sup>th</sup> and 13<sup>th</sup> analysis step can be found in the Appendix A 8.

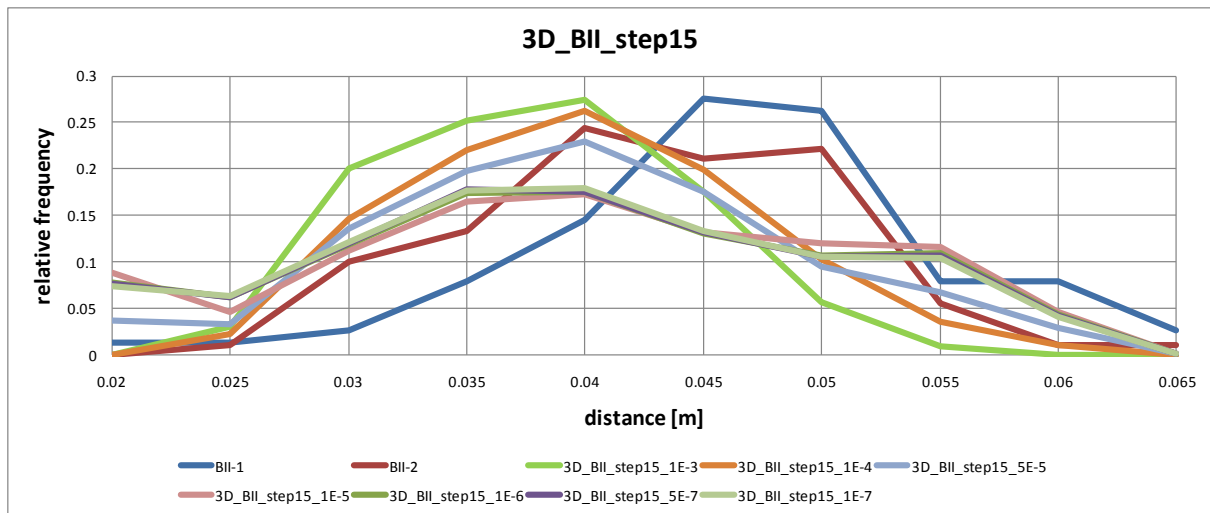


Figure 8-4 : Distances of fracture events – 3D\_BII\_step15

Figure 8-5 shows distances of fracture events for simulation 3D\_BII\_5E-5 at different analysis steps and one can observe that the results of numerical simulations are closer to the experimental results than in the case of numerical simulations performed in ATENA 2D (described in the subsection 7.2). The hypothesis that the 2D simulations are not capable to capture fracture events, because the failure occurs in 3D space and 2D simplification does not adequately count with the third dimension, was confirmed. However, still the same trend as in the 2D case can be observed, but exhibited in much lower manner, i.e the simulated data are shifted to the further distances (right).

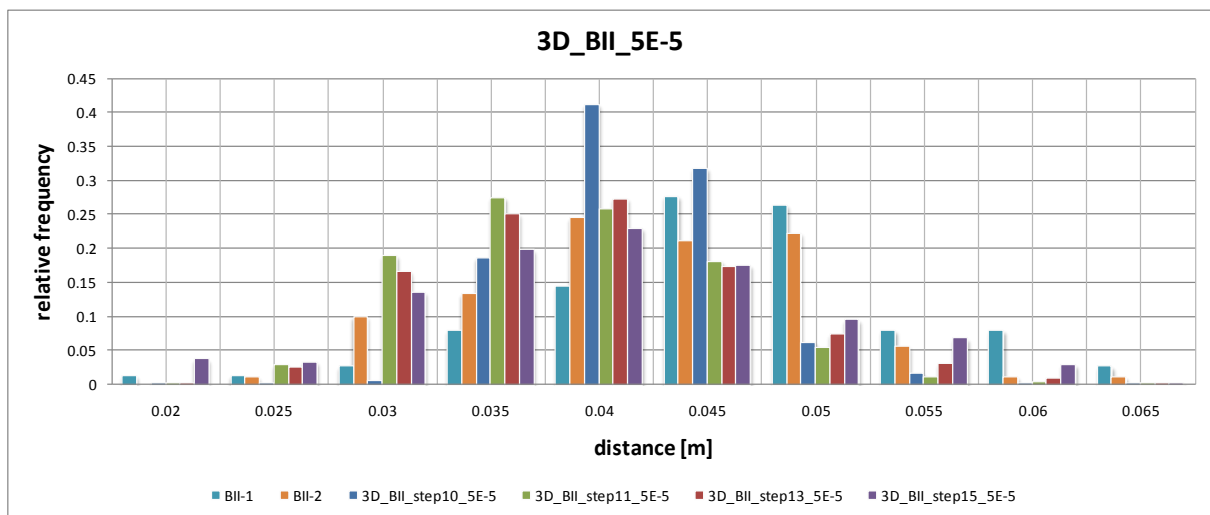


Figure 8-5 : Distances of fracture events – 3D\_BII\_5E-5

### 8.3.2 Configuration AI

Figure 8-6 shows comparison of L–D curves for the specimen set One. The peak points of L–D curves were: 26<sup>th</sup>, 12<sup>th</sup> and 10<sup>th</sup> for the configuration AI, AII and BII, respectively.

The PFS outputs were processed for 10<sup>th</sup>, 16<sup>th</sup>, 20<sup>th</sup> and 26<sup>th</sup> (= peak point of L–D curve) analysis step. The best results were obtained from the simulation 3D\_AI\_step16\_1E-6, as can be observed in Figure 8-7, because its curve corresponds most closely to the curve of experimental results AI-2. The graphs for 10<sup>th</sup>, 20<sup>th</sup> and 26<sup>th</sup> (= peak point of L–D curve) analysis step can be found in the Appendix A 9.

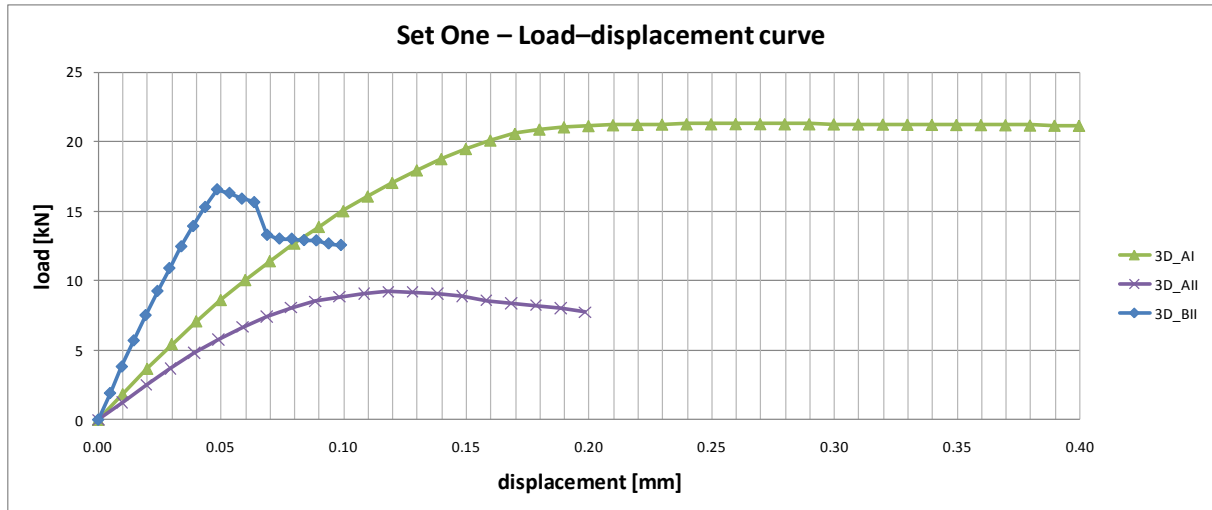


Figure 8-6 : Load–displacement curves – Set One

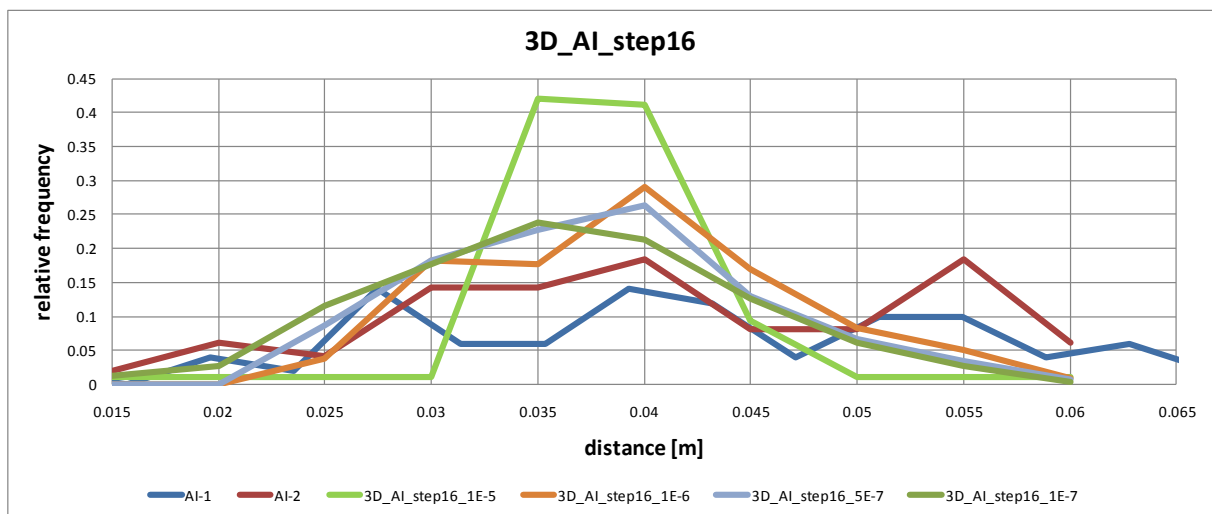


Figure 8-7 : Distances of fracture events – 3D\_AI\_step16

### 8.3.3 Configuration AII

The PFS outputs were processed for 11<sup>th</sup>, 12<sup>th</sup> (= peak point of L–D curve), 15<sup>th</sup> and 17<sup>th</sup> analysis step. Probably the most corresponding simulation was 3D\_AII\_step17\_1E-4, as can be observed in Figure 8-8, but the difference between curves obtained from experimental test and the simulated ones is quite large. The reason for such deviation can be, for example, strong background noise during the experimental test because the AE measurement is very

sensitive to the background noise. The graphs for 11<sup>th</sup>, 12<sup>th</sup> (= peak point of L–D curve) and 15<sup>th</sup> analysis step can be found in the Appendix A 10.

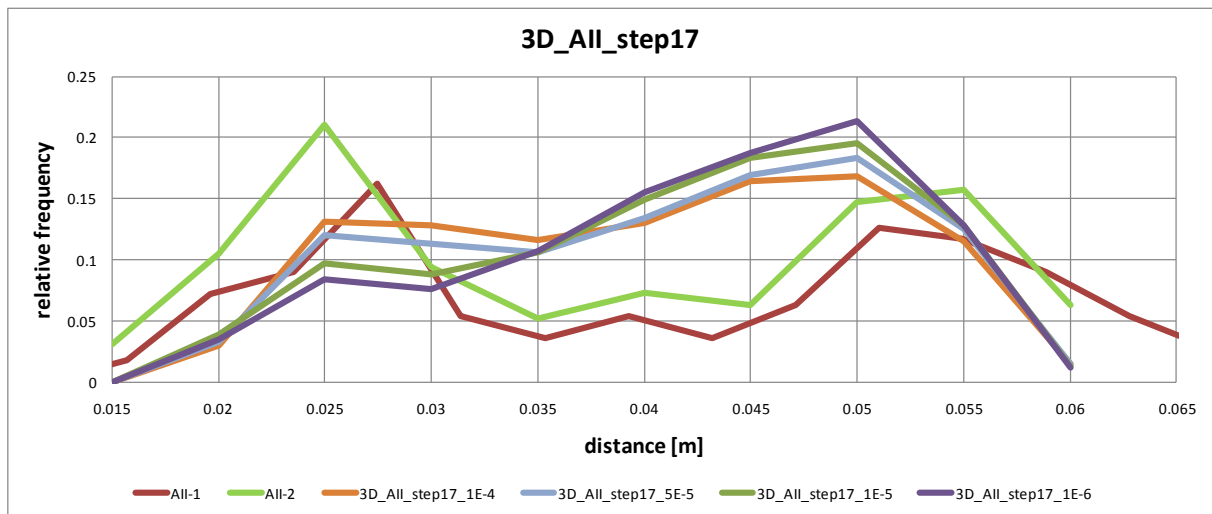


Figure 8-8 : Distances of fracture events – 3D\_AII\_step17

### 8.3.4 Conclusion

The conclusion to this whole subsection is that the 3D simulations are capable to capture fracture events and show good agreement between the experimental results and the simulated ones. The best agreement can be observed for the specimens in configuration AI and BII. The approximate size of the smallest experimentally detectable fracture events was determined as principal fracture strain of magnitude  $5 \times 10^{-5}$  (BII) or  $1 \times 10^{-6}$  (AI).

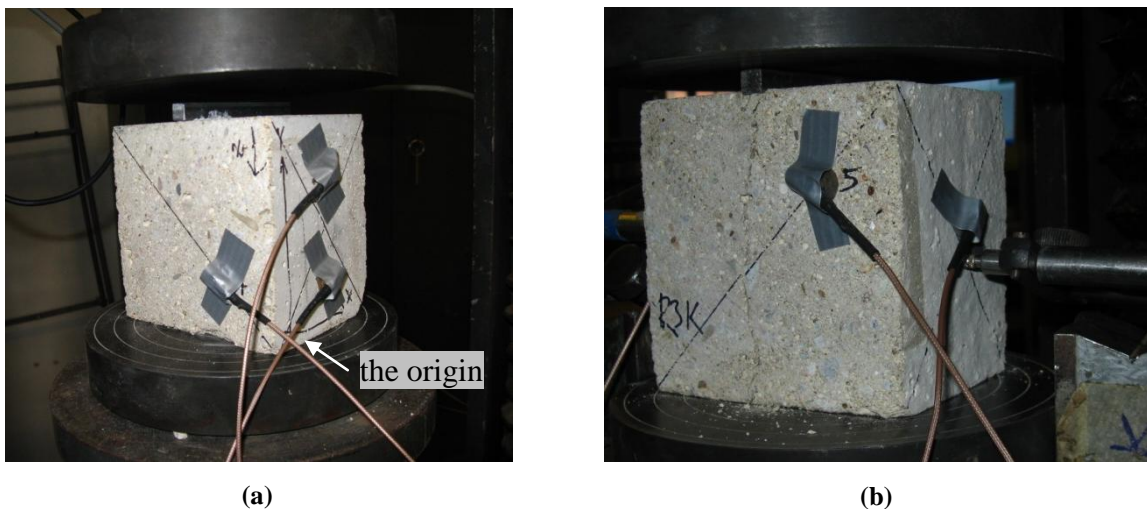


Figure 8-9 : Transducers positions – (a) "Front" view, (b) "Rear" view

The experimenters made a decision, based on the results of the above presented numerical simulations, to perform experimental tests on the specimens in configuration similar to BII recording only acoustic emission. The reason for this decision was to investigate location of fracture events without restriction caused by EME (i.e. the capacitor plates are capable



to record only fracture events that are spreading parallel to them; for more details, see subsection 4.2 or 7.2). In total, 5 acoustic transducers were placed at predefined positions on the specimen surface (Figure 8-9 shows positions of all 5 transducers; labels "Front" and "Rear" are related to the origin of the coordinate system which can be observed in Figure 5-10 (a) or Figure 8-9 (a) where "Front" denotes the view on specimen when the origin of the coordinate system is visible and "Rear" when not).

## 8.4 Failure location in 3D (AE)

This subsection includes numerical simulations concerning only acoustic emission measurements and further studies on the combination of acoustic and electromagnetic emission are in preparation.

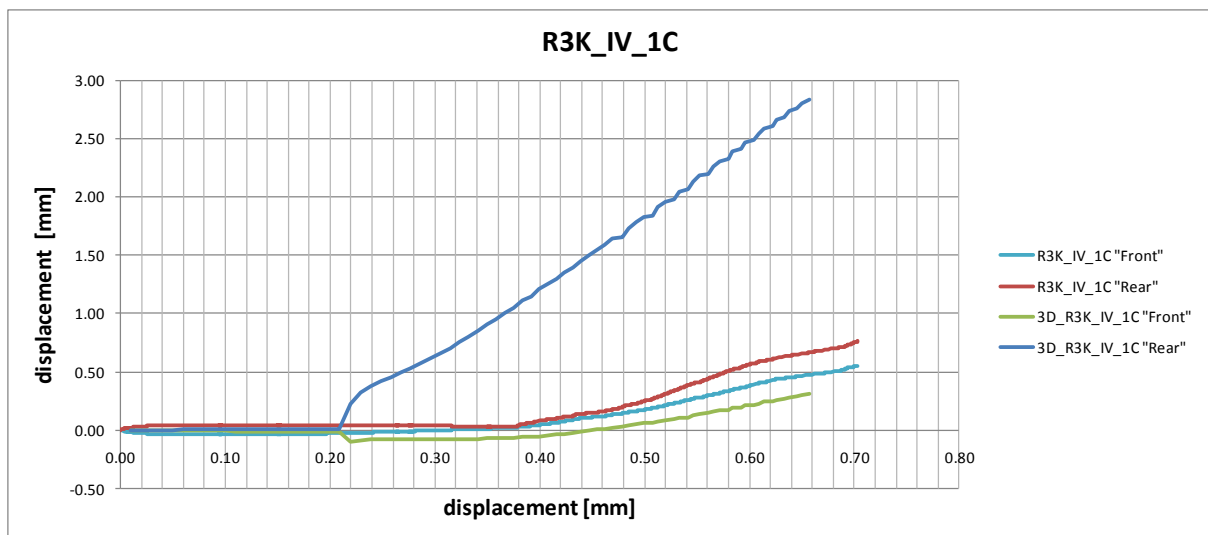


Figure 8-10 : Horizontal-vertical displacement curves – R3K\_IV\_1C

Specimen set Two was used for simulations. Available L–D diagrams from experimental tests were used for calibration of material models. Additionally, horizontal displacement (displacement perpendicular to the specimen side) of a specimen side lying in the  $x$ - $y$  plane and horizontal displacement of the opposite side were available (Figure 5-10 (a) shows orientation of axes; the measuring device (right) can be observed in Figure 8-9 (b)). Values of horizontal displacement were helpful for determination of contact parameters between the bottom jaw of testing machine and the concrete specimen (1C; Figure 8-10 shows the graph for R3K\_IV\_1C where the horizontal axis indicates displacement of upper loading prism and the vertical axis shows the horizontal displacement (displacement perpendicular to the specimen side) and showed that the friction coefficient between concrete and steel is about 0.35. The calculated distances of fracture events were separated into three



graphs according to the three axes of coordinate system, i.e.  $x$ ,  $y$  and  $z$  and are denoted in labels in graphs as ":X", ":Y" and ":Z", respectively.

It is worth pointing out that some of the results were already published in paper [52].

#### 8.4.1 Configuration CC

This configuration was modelled in order to see whether the numerical simulations with inputted material parameters obtained from conducted experimental compression tests (for details, see subsection 5.4) correspond to the L–D diagrams from the experiments. As can be observed from the graphs in Figure 8-11 and Figure 8-12, the curves show good agreement. It should be noted that the configuration CC was not used for the emission measurements.

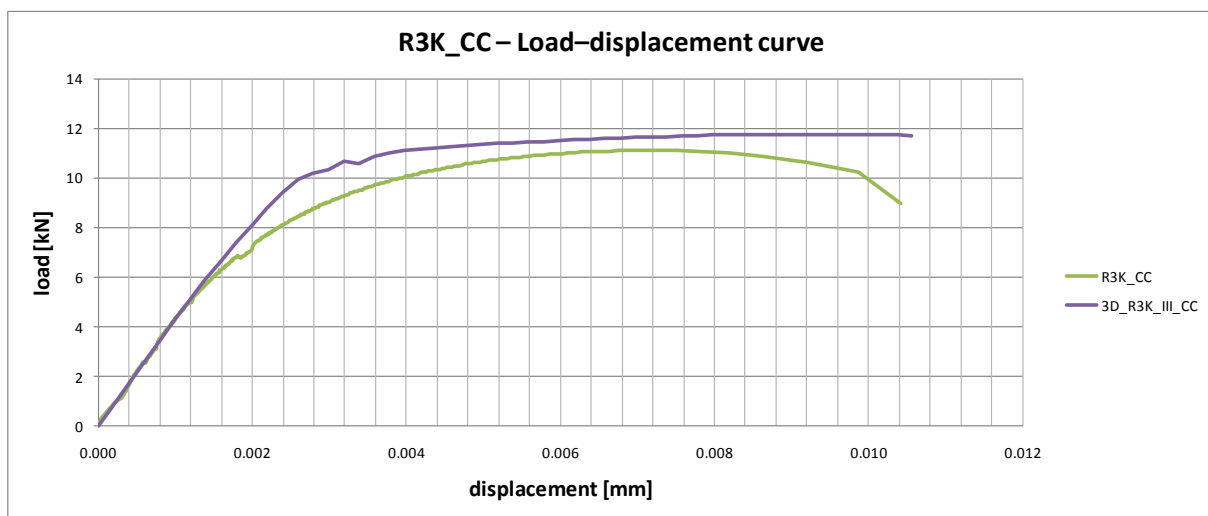


Figure 8-11 : Load–displacement curves – R3K\_CC

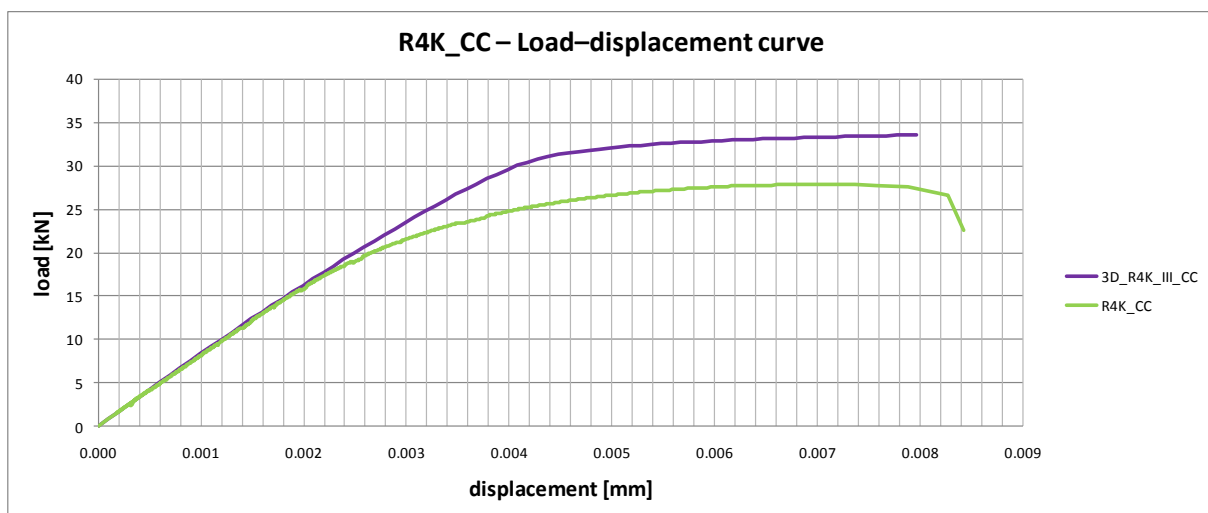


Figure 8-12 : Load–displacement curves – R4K\_CC

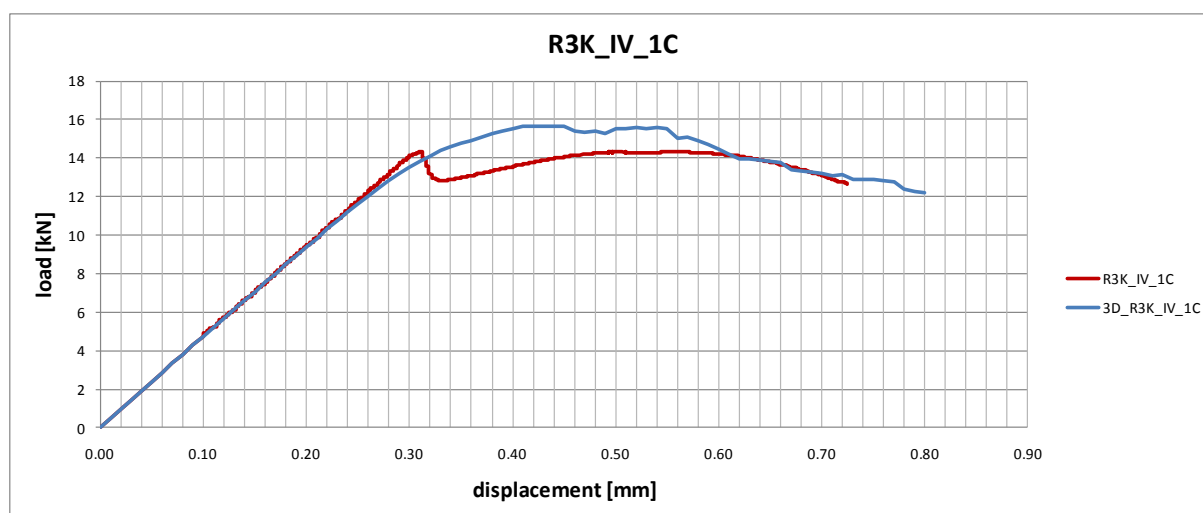
#### 8.4.2 Configuration 1C

The material model for the concrete mix R3 (for details, see subsection 5.3) was calibrated with the help of numerous parametric studies, the final relevant parameters of the material

model can be observed in Table 8-2 and the L–D curves for the specimen R3K\_IV\_1C comparing simulation with the experiment are shown in Figure 8-13.

**Table 8-2 : Relevant parameters of material model for the set Two**

	Material model
	<b>3D Non Linear Cementitious 2</b>
Elastic modulus $E$ [MPa]	4 340
Poisson's ratio $\nu$ [-]	0.200
Tensile strength $f_t$ [MPa]	0.793
Compressive strength $f_c$ [MPa]	-5.100
Specific fracture energy $G_f$ [MN/m]	1.981E-05
Fixed crack model coefficient	1.0
Critical compressive displacement $w_d$ [m]	-5.000E-04



**Figure 8-13 : Load–displacement curves – R3K\_IV\_1C**

### 8.4.3 Configuration 2C

The PFS outputs were processed for 21<sup>st</sup> (= peak point of L–D curve; the L–D curves for the specimen R3I\_2C comparing simulation with the experiment are shown in Figure 8-17) and 40<sup>th</sup> analysis step (denoted as Analysis step in graphs). The calculated distances for one chosen representative specimen (3D\_R3I\_2C\_5E-5) are shown in Figure 8-14, Figure 8-15 and Figure 8-16 and show the trend that can be observed for other specimens as well. It is not difficult to see that relative frequencies of simulations in the  $x$  and  $y$  direction (Figure 8-14 and Figure 8-15, respectively) do not fully correspond with the experimental data (labelled as TWO and KUR according to the methods described in the subsection 4.1.5; the interval in the bracket denotes the number of detected signal peaks, e.g. (0–168) denotes 168 detected signal

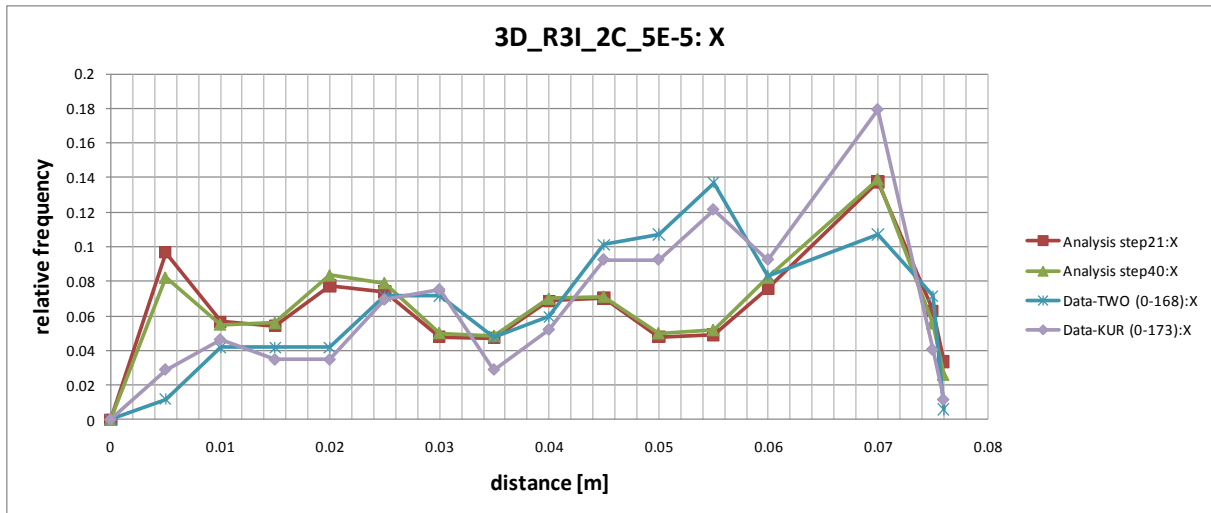


Figure 8-14 : Distances of fracture events in the x direction – 3D\_R3I\_2C\_5E-5

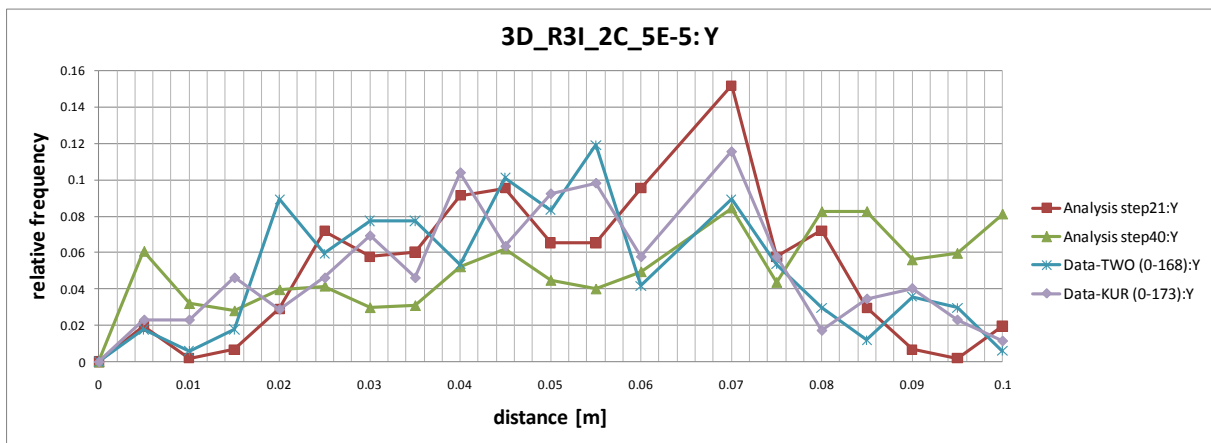


Figure 8-15 : Distances of fracture events in the y direction – 3D\_R3I\_2C\_5E-5

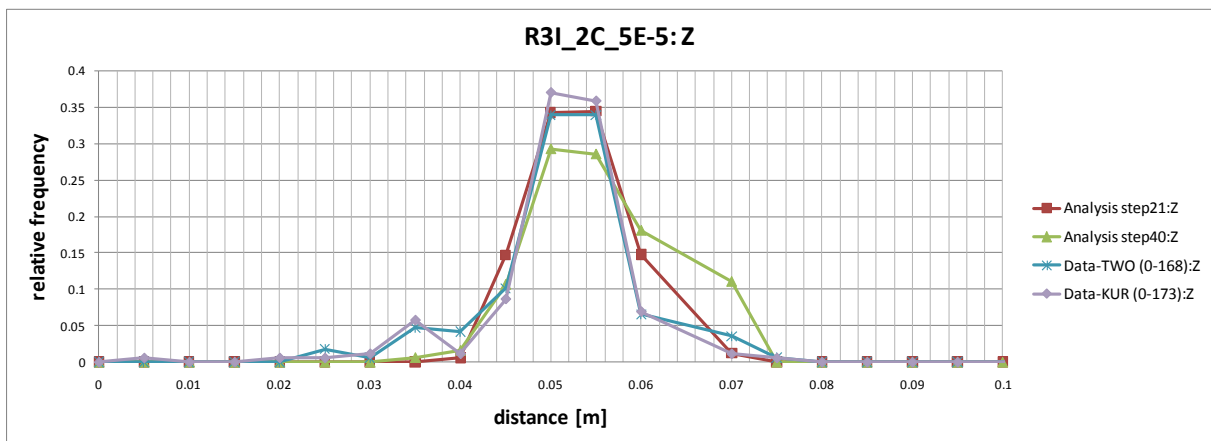


Figure 8-16 : Distances of fracture events in the z direction – 3D\_R3I\_2C\_5E-5

peaks used for the location with help of the method stated in front of the bracket) nevertheless are oscillating around the values obtained from experiments. On the contrary, relative frequencies of simulations in the  $z$  direction (Figure 8-13) are very satisfactory. Other graphs showing the distances of fracture events and the L–D curves for specimen R5I\_2C can be found in the Appendix A 11 and A 12, respectively.

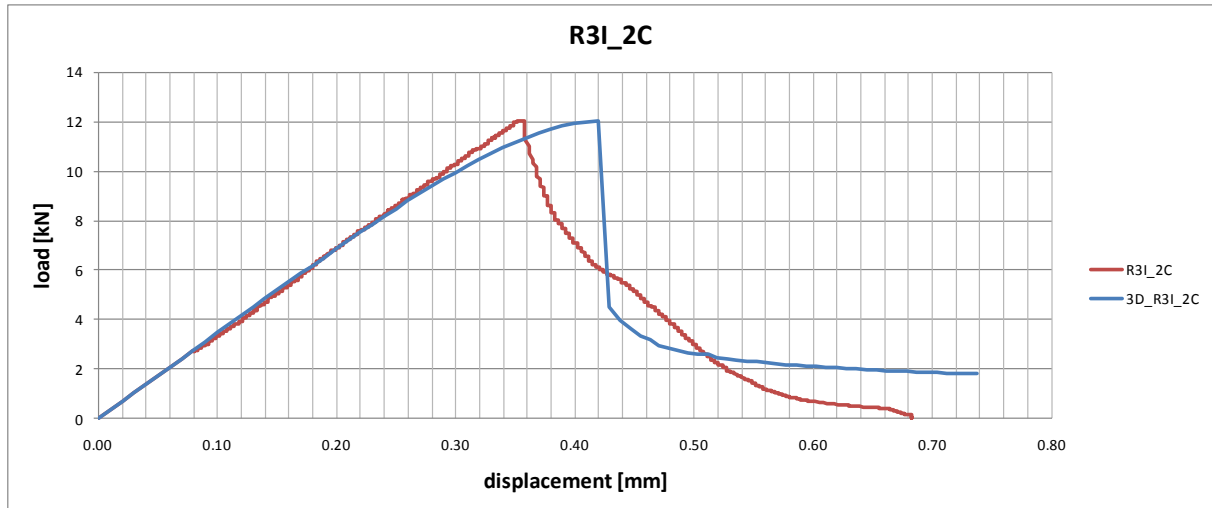


Figure 8-17 : Load–displacement curves – R3I\_2C

#### 8.4.4 Conclusion

From the conducted analyses it can be concluded that the approximate size of the smallest experimentally detectable fracture events was determined as principal fracture strain of magnitude  $5 \times 10^{-5}$ .



Figure 8-18 : Fracture plane – (a) Specimen R3K\_II\_1C, (b) Specimen R5I\_2C

The calculated relative frequencies of simulations in the  $z$  direction are very satisfactory, however, the relative frequencies of simulations in the  $x$  and  $y$  direction do not fully correspond with the experimental data nevertheless are oscillating around the values obtained

from experiments. A poor quality of used concrete blocks can be the reason for such behaviour. According to the compression tests, carried out on one block for each concrete mix (i.e. R3, R4, R5 and R6), the compressive strength of concrete was lower than the value listed in Eurocode 2 (subsection 5.5) and the modulus of elasticity was significantly lower for all tested specimens than the Eurocode 2 presents. During the experiments, it was observed that the concrete has unnatural colour and that the fracture planes contain unbroken aggregate particles (Figure 8-18) what confirms the poor quality of concrete. Therefore, it could happen that the performed numerical analyses are not capable to truly simulate a concrete of very poor quality and therefore, in order to be sure, it is necessary to conduct additional experiments on other concrete blocks having the parameters according to the Eurocode 2 (i.e. the concrete properties should roughly correspond to the default material model settings available in the software ATENA for the strength classes listed in the Eurocode 2).

## 9 Post-processing

### 9.1 Data processing in AtenaWin

AtenaWin working environment [47] was utilised to post-process all simulations performed in ATENA 3D to a form suitable for import into Microsoft Excel. Simulations results were saved in ATENA 3D post-processing environment as data files with extension denoting the analysis step (e.g. .001 denotes results of 1<sup>st</sup> analysis step). Reason for such decision was the fact that ATENA 3D displays results in form of sheets (Figure 9-1) which include header on every page and these headers prevent import of such outputs into Microsoft Excel. Additionally, the sheets can be saved only in file format .pdf or .rtf (.txt file format is not supported), which complicates the import into Microsoft Excel.

	Description:	<b>Specimen B</b>	Unit system:	Metric
	Note:	30x99x30 mm + 6x9 mm steel		
<b>MONITOR U1</b>				
Name: Force				
	<b>Step</b>		<b>Value [MN]</b>	
	3			-3.689E-03
	4			-4.800E-03
	5			-5.768E-03
	6			-6.666E-03

Figure 9-1 : Example of ATENA 3D results sheet

The desired result files were imported into AtenaWin by issuing the Monitors Export/Import command. For unknown reason, AtenaWin displays error message (Figure 9-2) at first attempt to import results files. It is necessary to hit "OK" button and try it for the second time. After successful import of result files, Data request command enables to select desired outputs of result file. IP coordinates and PFS in elements were imported into AtenaWin output window and saved as text files with .txt extension. Such data were prepared for further post-processing in Microsoft excel.

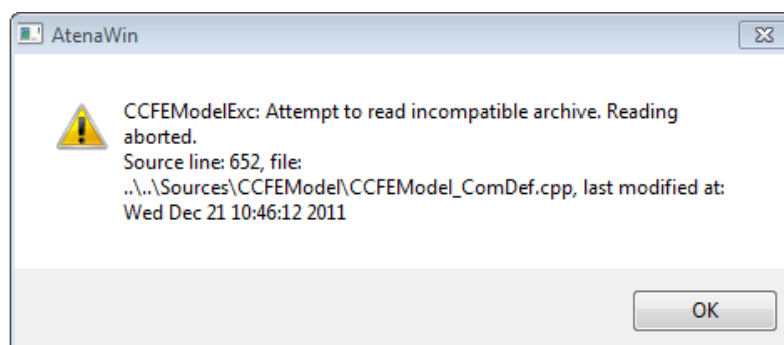


Figure 9-2 : AtenaWin error message

## 9.2 Post-processing in Microsoft Excel

In order to plot various graphs and compare large amount of data Microsoft (MS) Excel was used. As described in [48] MS Excel is software developed and manufactured by Microsoft Corporation that allows users to organise, format and calculate data with formulas using a spreadsheet system broken up by rows and columns. The first software program similar to Excel (Excel's precursor) was released in 1982 and was called Multiplan. Important part of MS Excel are macros described in [49; 50] as sets of instructions for tasks to perform on a given worksheet or data. By recording or programming certain actions, macros are used to utilise automate repetitive tasks, format data sheets or perform complex mathematical operations. By using macros it is possible to launch a virtually infinite number of tasks and processes with the simple touch of one button. Macro programming language is called VBA (Visual Basic for Applications) which is a subset of Visual Basic that provides a common language for customising Microsoft applications. VBA supports COM (Component Object Model) which allows a VBA script to invoke internal functions within Excel, Word and other COM-based programs.

Data obtained from simulations in ATENA were post-processed in MS Excel Workbooks using the advantages of macros in order to collect, move, filter, or plot the obtained data. Macros increase effectiveness of data processing and decrease the risk of errors during processing (with exception of systematic errors introduced in the code written by user). Workbooks with macros created by the author of this thesis are described in the following subsections.

### 9.2.1 Load Results workbook

Load Results workbook was utilised to post-process all simulations performed in ATENA 2D. Simulations results were saved in ATENA 2D post-processing environment as text files with .txt extension. ATENA 2D offers results saving only in format .txt or .rtf, and due to the problems with .rtf files import into MS Excel, only .txt file format was used.

In order to skip clicking-through MS Excel Text Import Wizard the LoadData macro, one of the two macros in Load Results workbook, includes commands performing this procedure automatically. LoadData macro (VBA code can be viewed in Figure 9-3) reads the A1 cell value entered in Load Results workbook by user, which represents number of .txt files being imported. Filenames have to be entered into cells starting B1 and continuing B2 and so on until all filenames are entered. It is important to note that all files have to be saved in direc-

tory listed in the VBA code (i.e. D:\Vodak\For calculation\). In order to make macro more user-friendly, keyboard shortcut Ctrl + l was assigned.

LoadData macro imports all data from .txt files to separate workbooks but this is not practical in the case that the data should be plotted on one graph. For this reason another macro was utilised. MoveResults macro (VBA code can be viewed in Figure 9-5), as follows from the name, moves simulations results imported in separate workbooks to Load Results workbook. The principle is similar to previous macro. It reads filenames in Load Results workbook, copies data from already opened workbooks by LoadData macro to Load Results and assigns them the filenames. Data are copied into columns according to the column labels entered into cells starting D1 (or E1) and continuing D2 (or E2) and so on until the number of labels is corresponding to number of filenames. Screenshot of Load Results is shown in Figure 9-4. For this macro was assigned the keyboard shortcut Ctrl + m.

```

Sub LoadData()
'
' Load data from txt files
' Keyboard shortcut: Ctrl+l
'
Dim a As Long
Dim b As String
Dim i As Long

a = 0
i = 0

a = Range("A1").Value           ' number of .txt files being imported
For i = 1 To a

    b = 0

    Windows("Load Results.xlsm").Activate
    b = Range("B" & i).Value    ' loads filenames

    ChDir "D:\Vodak\For calculation"
    Workbooks.OpenText Filename:= _
        "D:\Vodak\For calculation\" & b, _
        Origin:=852, StartRow:=1, DataType:=xlDelimited, TextQualifier:= _
        xlDoubleQuote, ConsecutiveDelimiter:=True, Tab:=True, Semicolon:=False, _
        Comma:=False, Space:=True, Other:=False, FieldInfo:=Array(Array(1, 1), _
        Array(2, 1), Array(3, 1)), DecimalSeparator:= ".", TrailingMinusNumbers:=True

Next
End Sub

```

**Figure 9-3 : LoadData Macro – VBA code**

With help of the above described macros the simulations results as displacements, loads, IP coordinates and PFS were imported into Load Results workbook and plotted on the graphs, which can be found in the section 7 or in the Appendix A.



	A	B	C	D	E	M	N	O	P	Q	R	S	T	U	V		
1		Sbeta_es10_2x2		M	O												
2		Sbeta_es10_7x10		R	T												
3		Sbeta_es10_8x8		W	Y												
4		Sbeta_es10_8x10		AB	AD												
5		Sbeta_es10_10x10		AG	AI												
6				AL	AN												
7				AQ	AS												
12								Sbeta_es10_2x2				Sbeta_es10_7x10					
13																	
14								[m]	[MN]	0	0	[m]	[MN]	0	0		
15								1	-4.58E-06	0.00E+00	4.58E-03	0.00E+00	1	-4.71E-06	-1.76E-03	4.71E-03	1.76E+00
16								2	-9.21E-06	0.00E+00	9.21E-03	0.00E+00	2	-9.42E-06	-3.50E-03	9.42E-03	3.50E+00
17								3	-1.38E-05	0.00E+00	1.38E-02	0.00E+00	3	-1.41E-05	-5.19E-03	1.41E-02	5.19E+00

Figure 9-4 : Screenshot of worksheet in Load Results workbook

```

Sub MoveResults()
'
' Moves results from opened workbooks to Load Results
' Keyboard shortcut: Ctrl+m
'
Dim a As Long
Dim b As String
Dim c As String
Dim d As String
Dim i As Long

a = 0
i = 0
c = 0

a = Range("A1").Value           ' number of .txt files being moved

For i = 1 To a
    b = 0
    c = Range("D" & i).Value    ' loads column labels
    d = Range("E" & i).Value
    Windows("Load Results.xlsm").Activate
    b = Range("B" & i).Value    ' loads filenames

    Range("B" & i).Select
    Application.CutCopyMode = False
    Selection.Copy
    Range(c & "12").Select
    ActiveSheet.Paste
    Windows(b).Activate
    Range("B15:C44").Select
    Application.CutCopyMode = False
    Selection.Copy
    Windows("Load Results.xlsm").Activate
    Range(c & "15").Select
    ActiveSheet.Paste
    Windows(b).Activate
    Range("C57:C86").Select
    Application.CutCopyMode = False
    Selection.Copy
    Windows("Load Results.xlsm").Activate
    Range(d & "15").Select
    ActiveSheet.Paste

Next

End Sub

```

Figure 9-5 : MoveResults macro – VBA code

### 9.2.2 Import of data workbook

Import of data workbook was utilised to import results of all simulations performed in ATENA 3D to MS Excel. In order to skip clicking-through MS Excel Text Import Wizard the Import of data macro includes commands performing this procedure automatically. Filenames of desired result files have to be entered into cells starting C3 and continuing C4 and so on until all filenames are entered. It is important to note that all files have to be saved in a folder whose name is entered into cell C2. The folder has to be saved in the directory listed in the VBA code (i.e. E:\ATENA\Diplomka\Exported results\). Import of data macro (VBA code can be viewed in Figure 9-6) reads all filenames which are entered in Import of data workbook and imports them to separate workbooks.

In order to make macro more user-friendly, keyboard shortcut Ctrl + i was assigned. Additionally, this macro includes command "PlaySound" that plays sound when the import is completed. This is useful in the case when the user imports a great number of files because the user can, in the meantime, do another task and is noticed when the import finishes.

```
Public Declare Function sndPlaySound32 _
    Lib "winmm.dll" _
    Alias "sndPlaySoundA" ( _
        ByVal lpszSoundName As String, _
        ByVal uFlags As Long) As Long ' declaration of sound function

Sub Import_of_data()
'
' Import data into Excel
' Keyboard shortcut: Ctrl+i
'
Set R = ActiveSheet.Range("C4") ' selects the cells
a = 1
Do While IsEmpty(R.Cells(a, 1)) = False ' finds first empty cell
    a = a + 1
Loop
b = a ' no of files for import
a = a + 2 ' last non-empty cell
folder = Range("C2").Value
For i = 3 To a
    Windows("Import of data.xlsm").Activate
    file = Range("C" & i).Value
    ChDir "E:\ATENA\Diplomka\Exported results\" & folder 'imports listed file
    Workbooks.OpenText Filename:= "E:\ATENA \Exported results\" & folder & "\" & file _
        , Origin:=852, StartRow:=1, DataType:=xlDelimited, TextQualifier:= _
        xlDoubleQuote, ConsecutiveDelimiter:=True, Tab:=True, Semicolon:=False, _
        Comma:=False, Space:=True, Other:=False, FieldInfo:=Array(Array(1, 1), _
        Array(2, 1), Array(3, 1), Array(4, 1), Array(5, 1), Array(6, 1)), TrailingMinusNumbers:=True
Next i
sndPlaySound32 "C:\Windows\Media\Chord.wav", 0& 'plays sound when finished
MsgBox ("Number of imported files: " & b)

End Sub
```

Figure 9-6 : Import of data macro – VBA code

### 9.2.3 Fracture strain 3D workbook

Fracture strain 3D workbook was utilised to assign IP coordinates to the corresponding PFS in order to be able to locate principal fracture strains. IP coordinates and PFS were copied from workbooks, already opened by Import of data macro, to Fracture strain 3D workbook by copy and paste command. PFS at each integration point were filtered by various threshold filter values (ranging between  $1 \times 10^{-3}$  and  $1 \times 10^{-7}$ ) in order to investigate the sensitivity of the examined experimental method. Values exceeding a chosen threshold were taken into account as fracture event. Subsequently, distance between the acoustic transducer and fracture event (represented by PFS) was calculated as vector length according to the formula given below.

$$\|\mathbf{d}\| = \sqrt{(x_T - x_P)^2 + (y_T - y_P)^2 + (z_T - z_P)^2} \quad (9.1)$$

where  $\|\mathbf{d}\|$  is the length or magnitude or norm of the vector  $\mathbf{d}$ ,

$x_T$  is the transducer position in the  $x$  direction,

$x_P$  is the PFS position in the  $x$  direction,

$y_T$  is the transducer position in the  $y$  direction,

$y_P$  is the PFS position in the  $y$  direction,

$z_T$  is the transducer position in the  $z$  direction,

$z_P$  is the PFS position in the  $z$  direction.

Obtained distances were classified into intervals and the intervals together with their representative values (= values shown on horizontal axis in the graph) can be found in Table 7-12. Quantities of fracture events in the individual intervals were subsequently divided by the total number of fracture events. This step brings the possibility to compare computed data with the experimental one because the obtained relative frequency is independent on number of events (of course, this is only true if the number of events is not too low; at least several tens are necessary) and the trend, representing how the fracture events are distributed, can be shown. It should be noted that the graphs presented in the section 8 (Simulations in ATENA 3D) show values on horizontal axis only for certain part of the interval (e.g. [0.02, 0.065]). This is in the case when there were no obtained distances belonging to the rest of the interval (e.g. (0, 0.02]).

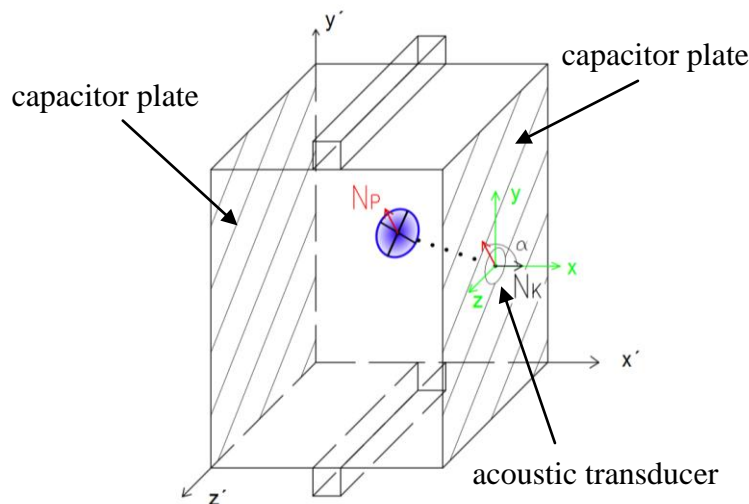
The above described procedure was conducted for evaluation of simulations of failure location and its comparison with locations of experimentally measured fracture events triggering acoustic emission. The simulations of experimental tests recording simultaneously the acoustic and electromagnetic emission contained one extra step in the post-processing in Fracture strain 3D workbook. The reason for this extra step is the fact that the capacitor plates are

capable to record only fracture events that are spreading parallel to them. This fact was already described in the subsection 7.2 and therefore is not given here. The principle of this extra step was already published in paper [53]. Before the PFS at each integration point were filtered by various threshold filter values they were multiplied by a coefficient whose value is dependent on the mutual spatial orientation of the monitored inelastic fracture strain and the plates of the capacitor placed on the sides of the specimen (angle  $\alpha$ , see Figure 9-7). The value of this coefficient is determined by the value of the cosine of the  $\alpha$  angle, i.e. if the normal vector of the fracture strain ( $N_p$ , herein it is a normal component of the unit vector that is used in the ATENA software to describe the direction of the deformation) forms a zero degree angle with the normal vector of the capacitor's plate ( $N_k$ ), the coefficient value is equal to one; in the case of a  $90^\circ$  angle it is equal to zero. Projection of the inelastic part of the principal tensile fracture strain on the plane perpendicular to the capacitor's plate plane is determined as:

$$\varepsilon^f = \varepsilon^{f,1} \cos \alpha \quad (9.2)$$

where  $\varepsilon^{f,1}$  is the inelastic (fracture) part of the principal tensile strain,

$\alpha$  is the spatial angle between the direction of the principal fracture strain and the normal vector of the capacitor's plate.



**Figure 9-7 : Scheme showing the determination of the spatial angle  $\alpha$  between the normal vector of a plane of a forming crack and the normal vector of the capacitor's plate**

## 10 Conclusion

The set goals were met and are briefly evaluated below:

- 2D and 3D numerical models representing real test specimens were created in ATENA 2D and ATENA 3D, respectively,
- 3D Non Linear Cementitious 2 material model was selected as a proper material for 2D and 3D simulations,
- 2D simulations were not satisfactorily capable to capture fracture events therefore solely 3D simulations are recommended for the simulations investigating the detection of acoustic/electromagnetic emission,
- 3D Non Linear Cementitious 2 material model was calibrated for 3D simulations,
- principal fracture strains were chosen as the proper program outputs for the comparison with the experimental results since they are least dependent upon the finite element size (i.e. mesh density),
- the approximate size of the smallest experimentally detectable fracture events was determined as principal fracture strain of magnitude  $5 \times 10^{-5}$  or  $1 \times 10^{-6}$ .

Disadvantage of the EME measurements is the fact that the capacitor plates are capable to record only fracture events (cracks) that are spreading parallel to them. It should be possible to restrain this disadvantage in further experiments via application of two capacitors placed on all 4 vertical sides of a specimen. Additionally, this improvement should enable to reveal what kind of fracture events or how many of them are recorded when the angle between them and capacitor plates lies in interval  $(0^\circ, 90^\circ)$ . The AE measurements show good agreement of the experimental results with the test ones.

The EME is accompanying AE (there is always less EME events than AE events detected by today's instrumentation). The reason for that is that the AE occurs already during formation of microcracks and the EME occurs afterwards because the electric charge has to accumulate before it can be detected. The AE can provide almost precise information concerning the crack location in the stressed material but only rough information concerning the crack properties. On the other hand, the EME can give almost precise information concerning crack formation, size, orientation and evolution but only rough information concerning the crack location [14]. Therefore, further investigations on combination of the AE and EME can provide relevant data concerning cracks.

The next step in the analysis should be to investigate the shape of EME signal because the shape can give more information concerning cracks, as already stated above, and the ob-

tained information can be compared with the cracks-related results of the numerical simulations. Additionally, further experiments can confirm/disprove current calibration of the numerical models.

## 11 Bibliography

1. **Federal Highway Administration.** U.S. Department of Transportation. *Guide to Nondestructive Testing of Concrete*. [Online] 1997. [Cited: 31 December 2012.] <http://isddc.dot.gov/OLPFiles/FHWA/006641.pdf>. FHWA-SA-97-105.
2. **Internal atomic energy agency.** *Guidebook on non-destructive testing of concrete structures*. Vienna : IAEA, 2002. ISSN 1018-5518.
3. **Carino, N. J.** American Concrete Institute (ACI). *Nondestructive Testing of Concrete: History and Challenges*. [Online] 1994. [Cited: 31 December 2012.] <http://fire.nist.gov/bfrlpubs/build94/PDF/b94056.pdf>.
4. **ACI Committee 228.** American Concrete Institute. *Nondestructive Test Methods for Evaluation of Concrete in Structures*. [Online] 24 June 1998. [Cited: 31 December 2012.] <http://citeseerx.ist.psu.edu/viewdoc/download?doi=10.1.1.111.2707&rep=rep1&type=pdf>.
5. **Bungey, J and Millard, S.** *Testing of concrete in structures*. 3rd ed. London : Blackie Academic & Professional, 1996. ISBN 0751402419.
6. **Engineers Daily.** Rebound Hammer Test. [Online] 2011. [Cited: 31 December 2012.] <http://www.engineersdaily.com/2011/04/rebound-hammer-test.html>.
7. **Humboldt Mfg. Co.** Concrete Test Hammers, Schmidt Hammers, Concrete Strength Testing. *Construction Materials Testing Equipment*. [Online] Humboldt, 2012. [Cited: 31 December 2012.] <http://www.humboldtmfg.com/c-3-p-246-id-3.html>.
8. *Acoustic emission and electrical properties of quasi-brittle materials under compression.* **Lacidogna, G., et al.** Conference Proceedings of the Society for Experimental Mechanics , New York : Springer New York, 2011, Vol. 6. ISBN 978-1-4614-0221-3.
9. **Carpinteri, A, et al.** Electromagnetic and neutron emissions from brittle rocks failure: Experimental evidence and geological implications . *Sadhana Vol.37, Part 1*. February 2012.
10. **NDT Education Resource Center.** Iowa State University. *Acoustic Emission Testing*. [Online] 2012. [Cited: 15 December 2012.] [http://www.ndt-ed.org/EducationResources/CommunityCollege/Other%20Methods/AE/AE\\_Index.htm](http://www.ndt-ed.org/EducationResources/CommunityCollege/Other%20Methods/AE/AE_Index.htm).
11. **NIH MBI Laboratory for Structural Genomics and Proteomics.** *Introduction to Hemihedral Twinning*. [Online] 2012. [Cited: 15 December 2012.] <http://nihserver.mbi.ucla.edu/Twinning/intro.html>.

12. **ESA.** IMPRESS Education: Mechanical Properties, Dislocations. *Dislocations*. [Online] 17 November 2009. [Cited: 16 December 2012.] <http://www.spaceflight.esa.int/impresstext/education/Mechanical%20Properties/Dislocations.html>.
13. *Noise diagnostics of advanced composite materials for structural applications.* **Koktavý, Pavel, Trčka, Tomáš and Koktavý, Bohumil.** Toronto : 21st International Conference on Noise and Fluctuations, 2011. ISBN: 978-1-4577-0191- 7.
14. **Trčka, Tomas, Tofel, Pavel and Koktavý, Pavel.** Electromagnetic and Acoustic Emission Signals Real-Time Measurement, Processing and Data Evaluation. *Key Engineering Materials. Materials Structure & Micromechanics of Fracture VI*, 2011, Volume 465.
15. **Burděj, Václav.** *Využití signálů elektromagnetické a akustické emise pro lokalizaci trhlin vznikajících při mechanickém zatěžování pevných látek.* Brno, 2008. Diplomová práce : Vysoké učení technické v Brně, Fakulta elektrotechniky a komunikačních technologií, Ústav telekomunikací.
16. **National Instruments Corporation.** *NI LabVIEW - Improving the Productivity of Engineers and Scientists.* [Online] 2012. [Cited: 22 December 2012.] <http://sine.ni.com/np/app/main/p/docid/nav-104/lang/cs/>.
17. **Kurz, Jochen H., Grosse, Christian U. and Reinhardt, Hans-Wolf.** Strategies for reliable automatic onset time picking of acoustic emissions and of ultrasound signals in concrete. *Elsevier. Ultrasonics*, June 2005, Vol. 43, Issue7.
18. **Sedlak, Petr, et al.** New automatic localization technique of acoustic emission signals in thin metal plates. *Elsevier. Ultrasonics*, February 2009, Vol. 49, Issue 2.
19. **O'Keefe, Steven G. and Thiel, David V.** A mechanism for the production of electromagnetic radiation during fracture of brittle materials. *Elsevier. Physics of the Earth and Planetary Interiors*, May 1995, Vol. 89, Issue 1-2.
20. **TechTarget.** SearchCIO-Midmarket. *What is charge (electric charge)? – Definition from WhatIs.com.* [Online] March 2010. [Cited: 10 November 2012.] <http://searchcio-midmarket.techtarget.com/definition/charge>.
21. **Frid, V., Rabinovitch, A. and Bahat, D.** Fracture induced electromagnetic radiation. *Journal of physics. Applied physics*, 2003, Vol. 36.



22. **EPP.** *Electromagnetic Radiation Shielding & Magnetic Field Shielding Technology for Buildings, Equipment Rooms and like applications.* [Online] 2011. [Cited: 27 December 2012.] [http://www.euro-emc.co.uk/faqs\\_electromagneticshielding.html](http://www.euro-emc.co.uk/faqs_electromagneticshielding.html).
23. **ČSN EN 1992-1-1 Eurokód 2.** *Navrhování betonových konstrukcí – Část 1-1: Obecná pravidla a pravidla pro pozemní stavby.* Praha : Úřad pro technickou normalizaci, metrologii a státní zkušebnictví, 2006.
24. **ČSN EN 12390-3.** *Zkoušení ztvrdlého betonu – Část 3: Pevnost v tlaku zkušebních těles.* Praha : Úřad pro technickou normalizaci, metrologii a státní zkušebnictví, 2009.
25. **ČSN ISO 6784 .** *Beton. Stanovení statického modulu pružnosti v tlaku.* Praha : Federální úřad pro normalizaci a měření, 1993.
26. **Cikrle, Petr, et al.** *NDT zkoušení ve stavebnictví.* Brno : Ústav stavebního zkušebnictví, Fakulta stavební, VUT v Brně, 2010. ISBN 978-80-214-4198-9.
27. **Skaarhoj, Kasper.** *Non Destructive Test Equipment.* [Online] Proceq, 2012. [Cited: 24 October 2012.] <http://www.proceq.com/en/non-destructive-test-equipment-home-europe-non-destructive-test-equipment.html?setpqr=1&pqr=2>.
28. **Proceq.** *Portable Concrete Testing Instruments For Non-Destructive Site Investigation.* [Online] 2012. [Cited: 24 October 2012.] [http://www.jroma.pt/PDFS/catalogo\\_proceq.pdf](http://www.jroma.pt/PDFS/catalogo_proceq.pdf).
29. **Tico Operating Instructions.** *Ultrasonic Testing Instrument.* [Online] 2008. [Cited: 29 December 2012.] [http://www.abmbv.nl/files/proceq\\_tico\\_user\\_manual\\_en.pdf](http://www.abmbv.nl/files/proceq_tico_user_manual_en.pdf).
30. **Dynamické moduly pružnosti.** Ústav stavebního zkušebnictví, FAST, VUT v Brně. *BI02 Zkušebnictví a technologie – Návod do cvičení.* [Online] 9 November 2009. [Cited: 30 December 2012.] [http://147.229.27.214/vyuka/BI02/D\\_navod.pdf](http://147.229.27.214/vyuka/BI02/D_navod.pdf).
31. **ČSN 73 1371.** *Nedestruktivní zkoušení betonu – Ultrazvuková impulzová metoda zkoušení betonu.* Praha : Úřad pro technickou normalizaci, metrologii a státní zkušebnictví, 2011.
32. **ČSN 73 2011.** *Nedestruktivní zkoušení betonových konstrukcí.* Praha : Úřad pro technickou normalizaci, metrologii a státní zkušebnictví, 2012.
33. **Pryl, Dobromil and Červenka, Jan.** *ATENA Program Documentation, Part 11, Troubleshooting Manual.* Prague : Cervenka Consulting Ltd., 2012.
34. **Jendele, Libor.** *ATENA Program Documentation, Part 2-1, User's Manual for ATENA 2D.* Prague : Cervenka Consulting Ltd., 2012.

35. **Červenka, Vladimír and Červenka, Jan.** *ATENA Program Documentation, Part 2-2, User's Manual for ATENA 3D.* Prague : Cervenka Consulting Ltd., 2011.
36. **Bruch, John C.** MODULE for Plane Stress and Plain Strain Analysis. *ME 271/MATRL 240.* [Online] 10 March 2006. [Cited: 28 October 2012.]  
<http://www.engineering.ucsb.edu/~hpscicom/projects/stress/introge.pdf>.
37. **TKT4192-Elementstyrksmethode – lecture notes.** *Appendix A: Topics in Theory of Elasticity.* Trondheim : Norges teknisk-naturvitenskapelige universitet, 2008.
38. **Červenka, Vladimír, Jendele, Libor and Červenka, Jan.** *ATENA Program Documentation, Part1, Theory.* Prague : Cervenka Consulting Ltd., 2012.
39. **Červenka, Jan and Papanikolaou, Vassilis K.** Three dimensional combined fracture-plastic material model for concrete. *International Journal of Plasticity* 24. 2008.
40. **Cervenka, Vladimír, Cervenka, Jan and Pukl, Radomir.** ATENA-A tool for engineering analysis of fracture in concrete. *Sadhana Vol.27, Part 4.* 2002.
41. *Analýza napjatosti a šíření trhlin ve zkušebních vzorcích pro měření poškození kvazikřehkého materiálu pomocí elektromagnetické emise.* **Veselý, Václav, Frantík, Petr and Keršner, Zbyněk.** Ostrava : Vysoká škola báňská - Technická univerzita Ostrava, 2007. ISBN: 978-80-248-1330- 1.
42. **Wikiversity.** *Nonlinear finite elements/Lagrangian and Eulerian descriptions.* [Online] 2 September 2010. [Cited: 30 November 2012.]  
[http://en.wikiversity.org/wiki/Nonlinear\\_finite\\_elements/Lagrangian\\_and\\_Eulerian\\_descriptions](http://en.wikiversity.org/wiki/Nonlinear_finite_elements/Lagrangian_and_Eulerian_descriptions).
43. **S.L.Chan.** "Stability of Structures" with application to practical design. *结构与岩土工程研究中心 (Harbin Institute of Technology Shenzhen Graduate School).* [Online] September 2004. [Cited: 2 December 2012.]  
<http://sys.hitsz.edu.cn/rc/ResCenter/city/jgyt/service/courseware/steel/Chapter%204.pdf>.
44. **Koktavý, Pavel, et al.** Utilization of Electromagnetic and Acoustic Emission in Monitoring of Fracture of Cementitious Composites. *Key Engineering Materials.* 2011, Vol. 465, ISSN: 1013- 9826.
45. **Cusatis, Gianluca, et al.** Lattice Discrete Particle Model (LDPM) for failure behavior of concrete. II: Calibration and validation. *Cement and Concrete Composites.* Volume 33, 2011, Issue 9.

46. **Kabele, Petr, Červenka, Vladimír and Červenka, Jan.** *ATENA Program Documentation, Part 3-1, Example Manual ATENA Engineering.* Prague : Cervenka Consulting Ltd., 2012.
47. **Jendele, Libor.** *ATENA Program Documentation, Part 7, AtenaWin Description.* Prague : Cervenka Consulting Ltd., 2011.
48. **WebFinance, Inc.** BusinessDictionary.com. *What is Microsoft Excel? definition and meaning.* [Online] 2012. [Cited: 5 December 2012.]  
<http://www.businessdictionary.com/definition/Microsoft-Excel.html>.
49. **Demand Media, Inc.** eHow. *Definition of an Excel Macro.* [Online] 16 April 2012. [Cited: 5 December 2012.] [http://www.ehow.com/facts\\_4970349\\_definition-excel-macro.html](http://www.ehow.com/facts_4970349_definition-excel-macro.html).
50. **The Computer Language Company Inc.** PCMAG. *VBA Definition from PC Magazine Encyclopedia.* [Online] 2012. [Cited: 5 December 2012.]  
[http://www.pcmag.com/encyclopedia\\_term/0,1237,t=VBA&i=53690,00.asp](http://www.pcmag.com/encyclopedia_term/0,1237,t=VBA&i=53690,00.asp).

**Published papers containing author's contribution**

51. *Verifikace lokalizace a průběhu porušení v betonových vzorcích stanovených pomocí AE a EME: Numerické simulace.* **Veselý, Václav, Frantík, Petr, and Vodák, Ondřej.** In: Sborník příspěvků mezinárodní konference Modelování v mechanice 2011. Ostrava: Vysoká škola báňská - Technická univerzita Ostrava, Fakulta stavební, 2011. ISBN: 978-80-248-2384-3.

52. *Numerical simulation of failure processes in plain concrete causing acoustic and electromagnetic emission.* **Vodák, O., Veselý, V., Trčka, T., Kockavý, P., Kockavý, B. and Keršner, Z.** In: Book of extended abstracts of conference Computational Mechanics 2012 (CD-ROM), Špičák, November 12–14, 2012. V. Adámek, M. Zajíček, A. Jonášová (Eds.). University of West Bohemia, Pilsen, 2012, 2 p. ISBN 978-80-261-0157-4.

53. *Localization of Propagation of Failure in Concrete Specimens Assessed by Means of Acoustic and Electromagnetic Emission and Numerical Simulations.* **Veselý, Václav, Frantík, Petr, Vodák, Ondřej and Keršner, Zbyněk.** s.l. : Transactions of the VŠB – Technical University of Ostrava, December 2011, Vol. XI. ISSN (Online) 1804-4824, ISSN (Print) 1213-1962.

## 12 List of symbols, physical constants and abbreviations

$a$	Specimen width
$a_i$	Width/height of specimen side
$a_{ij}$	Entry in the $i$ -th row and $j$ -th column of a matrix
$b$	Specimen breadth
$\underline{b}$	Right hand side of linear algebraic equation
$c$	Compressive strength in cracked concrete
$dxdy$	Infinitesimal element in 2D space
$dV$	Volume of Infinitesimal particle
$\mathbf{d}$	Vector representing distance between acoustic transducer and fracture event
$\ \mathbf{d}\ $	Length or magnitude or norm of the vector $\mathbf{d}$
$\mathbf{e}$	Strain vector
$f_c; f'_c$	Concrete cylinder strength
$f_{cd}$	Design value of concrete compressive strength
$f_{ck}$	Characteristic compressive cylinder strength of concrete at 28 days
$f_{ck,cube}$	Characteristic compressive cube strength of concrete at 28 days
$f'_{cu}$	Concrete cube strength
$f_t; f'_t$	Concrete tensile strength
$f'_{ti}$	Tensile strength in the material direction $i$
$f(\underline{p})$	Internal joint forces vector
$g$	Acceleration due to gravity (chosen in this thesis as $10 \text{ m/s}^2$ ),
$h$	Specimen height
$k$	Size coefficient
$m$	Material mass
$m_1; m_2$	Orthotropy axes
$m(X)$	Mean measure of central tendency
$\underline{p}$	Structure deformations prior to load increment
$s$	Second (unit of time)
$\mathbf{s}$	Stress vector
$\mathbf{s}_c$	Concrete stress vector
$\mathbf{s}_s$	Steel (reinforcement) stress vector
$t$	Time
$t_L$	Passing time of ultrasound across specimen length
$u$	Displacement in the $x$ direction
$v$	Displacement in the $y$ direction
$v_L$	Average propagation speed of ultrasound across specimen length
$v_{L3}$	Average propagation speed of ultrasound in three-dimensional environment
$w_d$	Softening compression
$x_p$	PFS position in the $x$ direction

$x_T$	Transducer position in the $x$ direction
$y_P$	PFS position in the $y$ direction
$y_T$	Transducer position in the $y$ direction
$z_P$	PFS position in the $z$ direction
$z_T$	Transducer position in the $z$ direction
$A$	Cross section of composite material
$A_c$	Material area of concrete
$A_m$	Mean value (= arithmetic mean)
$\mathbf{A}$	Global structural matrix
$\mathbf{A}'$	Preconditioning matrix
$C$	Coulomb (unit of electrical charge)
$D$	Standard deviation (= average absolute deviation)
$\mathbf{D}$	Material stiffness matrix; Diagonal matrix
$\mathbf{D}_c$	Material stiffness matrix for uncracked concrete
$\mathbf{D}_c^L$	Local material stiffness matrix for cracked concrete
$\mathbf{D}'$	Diagonal preconditioning matrix
$[\mathbf{D}]$	Stiffness (stress/strain) matrix
$E$	Modulus of elasticity
$E_{bu}$	Dynamic modulus of elasticity in tension and compression
$E_c$	Initial elastic modulus; Static modulus of elasticity in compression
$E_{cm}$	Secant modulus of elasticity of concrete
$F_{max}$	Maximal imposed load
$G$	Shear modulus
$G_f$	Fracture energy
$G_t$	Tangent shear modulus
$\mathbf{K}(p)$	Stiffness matrix relating loading increments to deformation increments
$L$	Specimen length
$\mathbf{L}$	Lower triangular matrix
$\mathbf{L}'$	Lower triangular preconditioning matrix
$N_K$	Normal vector of the capacitor's plate
$N_P$	Normal vector of the fracture strain
$R_{be}$	Informative concrete compressive strength
$\mathbf{U}$	Upper triangular matrix
$\mathbf{U}'$	Upper triangular preconditioning matrix
$V$	Volume of specimen
$X$	Body forces per unit volume in the $x$ direction
$Y$	Body forces per unit volume in the $y$ direction

$\alpha$	Spatial angle
$\alpha_{cc}$	Coefficient taking account of long term effects on the compressive strength
$\gamma$	Specific material weight
$\gamma_C$	Partial factor for concrete
$\gamma_{max}$	Orientation factor for strain localization
$\gamma_{xy} = \gamma_{yx}$	Shear strain in $x$ - $y$ plane
$\gamma_{xz} = \gamma_{zx}$	Shear strain in $x$ - $z$ plane
$\gamma_{yz} = \gamma_{zy}$	Shear strain in $y$ - $z$ plane
$\{\varepsilon\}$	Strain vector
$\varepsilon_1; \varepsilon_2$	Principal strains
$\varepsilon_{abs.force}$	Norm of out-of-balance forces in terms of maximum components
$\varepsilon_{rel.displ}$	Norm of deformation changes
$\varepsilon_{rel.energy}$	Norm of out-of-balance energy
$\varepsilon_{rel.force}$	Norm of out-of-balance forces
$\varepsilon_x$	Strain in the $x$ direction
$\varepsilon_y$	Strain in the $y$ direction
$\varepsilon_{ij}^e$	Elastic strain component
$\varepsilon_{ij}^f$	Fracturing strain component
$\varepsilon_{ij}^p$	Plastic strain component
$\lambda_L$	Wave length
$\nu$	Poisson's ratio
$\rho$	Material density; Specific material weight
$\{\sigma\}$	Normal stress vector
$\sigma_1; \sigma_2$	Principal stresses
$\sigma_{c1}$	Stress normal to the crack plane
$\sigma_{c2}$	Stress parallel to the crack plane
$\sigma_{max}; \sigma_{min}$	Maximum and minimum normal stresses
$\sigma_{st}$	Tension stiffening stress
$\sigma_x$	Normal stress in the $x$ direction
$\sigma_y$	Normal stress in the $y$ direction
$\sigma_z$	Normal stress in the $z$ direction
$\sigma_{xy}$	Shear stress in the $x$ - $y$ plane
$\sigma_{xz}$	Shear stress in the $x$ - $z$ plane
$\sigma_{yz}$	Shear stress in the $y$ - $z$ plane
$\sigma_{ii}^t$	Trial stress in the material direction $i$
$\tau_{xy} = \tau_{yx}$	Shear stress in the $x$ - $y$ plane
$\Delta$	Increment
$\Delta p$	Deformation increment due to loading increment

$\partial$	Partial derivative
<sup>T</sup>	Transpose of matrix or vector ( <sup>T</sup> as superscript)
kB	Kilobyte (multiple of the unit byte for digital information)
max.	Maximum
MB	Megabyte (multiple of the unit byte for digital information)
min.	Minimum
pcs.	Pieces
vs.	Versus
2D	Two-dimensional
3D	Three-dimensional
AE	Acoustic Emission(s)
AET	Acoustic Emission Testing
AIC	Akaike Information Criterion
ATENA	Advanced Tool for Engineering Nonlinear Analysis
COD	Crack Opening Displacement
COM	Component Object Model
CPU	Central Processing Unit
EME	Electromagnetic Emission(s)
FE	Finite Element
FEM	Finite Element Method
FNR	Full Newton-Raphson
FPZ	Fracture process zone
IP	Integration Points
LabVIEW	Laboratory Virtual Instrumentation Engineering Workbench
L–D	Load–displacement
MNR	Modified Newton-Raphson
MS	Microsoft
NDT	Non-Destructive Test
No.	Number
PFS	Principal Fracture Strain(s)
PZT	Lead zirconate titanate (inorganic compound)
TL	Total Lagrangian
UL	Updated Lagrangian
VBA	Visual Basic for Applications

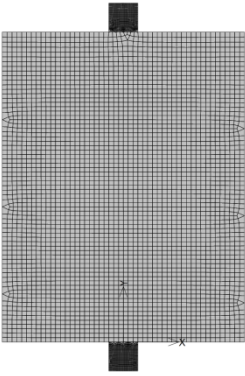
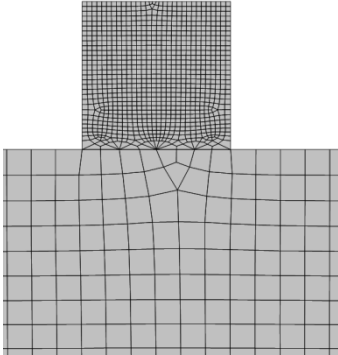
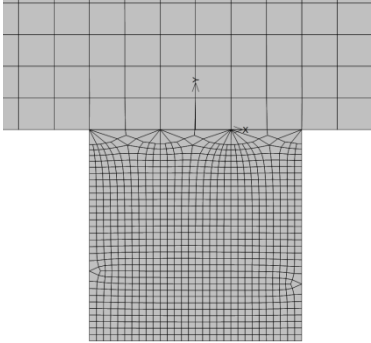
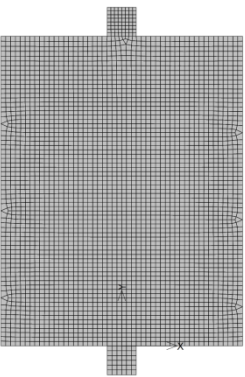
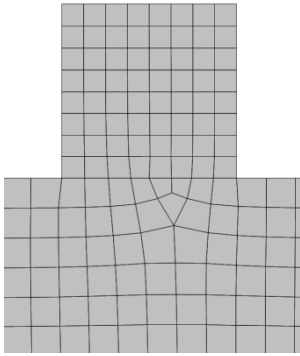
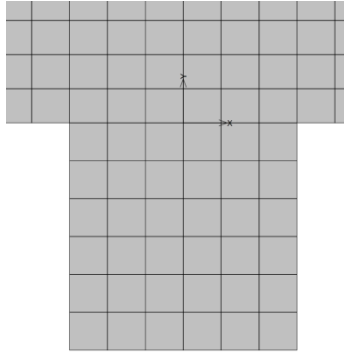
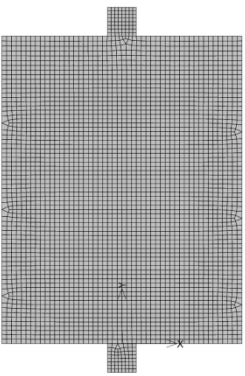
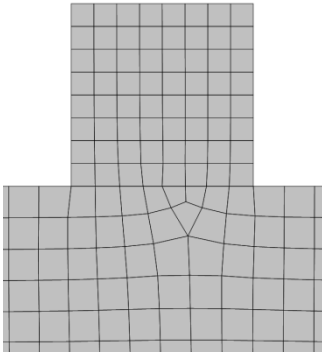
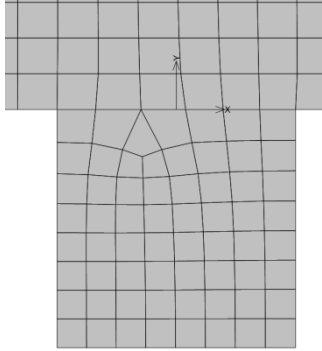


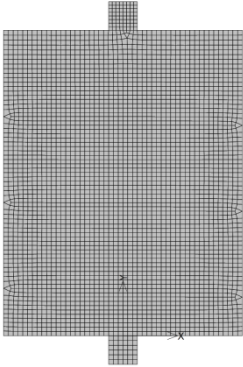
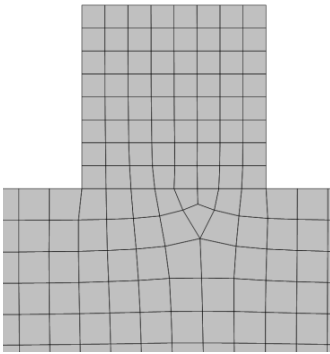
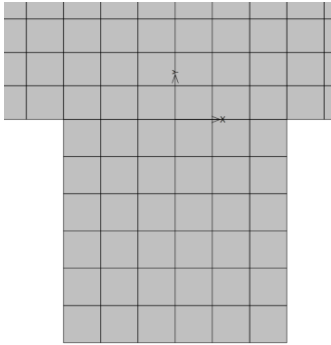
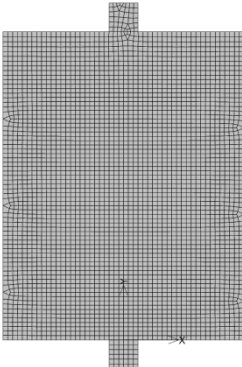
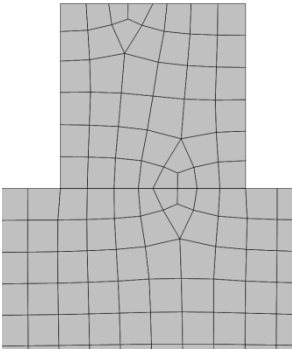
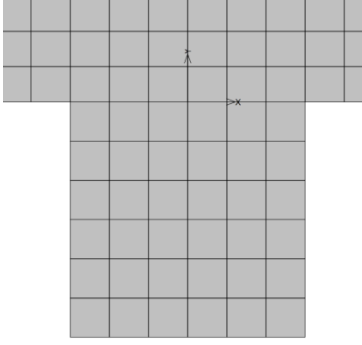
## List of Appendices

A 1 : Mesh connectivity – generated mesh .....	II
A 2 : Mesh connectivity – crack pattern .....	IV
A 3 : Mesh size – generated mesh.....	V
A 4 : Mesh size – crack pattern .....	VIII
A 5 : Material model – load–displacement curves .....	XI
A 6 : Failure location in 2D (AE + EME) – distances of fracture events.....	XIII
A 7 : Failure location in 3D (AE + EME) – load–displacement curves .....	XV
A 8 : Failure location in 3D (AE + EME) – distances of fracture events for 3D_BII .....	XVI
A 9 : Failure location in 3D (AE + EME) – distances of fracture events for 3D_AI .....	XVII
A 10 : Failure location in 3D (AE + EME) – distances of fracture events for 3D_AII.....	XVIII
A 11 : Failure location in 3D (AE) – distances of fracture events for 3D_R5I_2C_5E-5.....	XIX
A 12 : Failure location in 3D (AE) – load–displacement curves for R5I_2C .....	XX

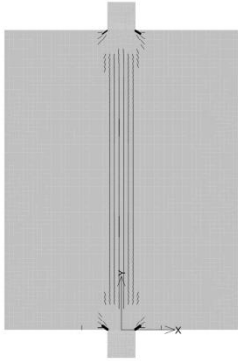
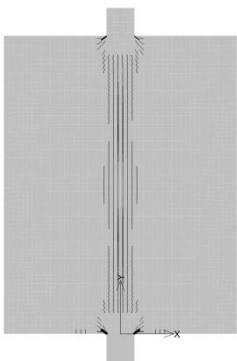
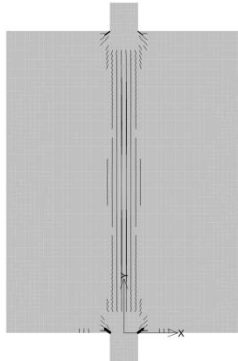
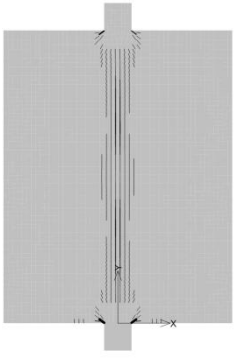
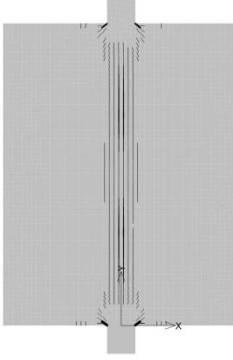
## A Appendix

### A 1 : Mesh connectivity – generated mesh

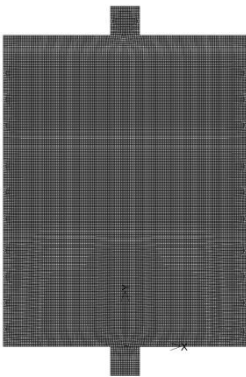
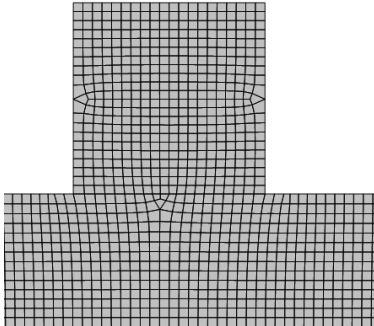
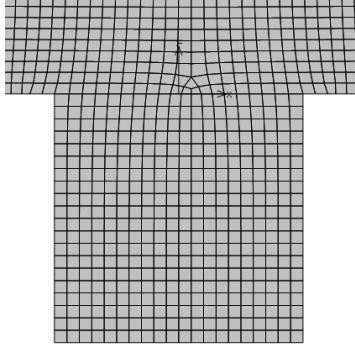
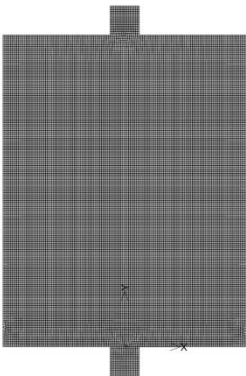
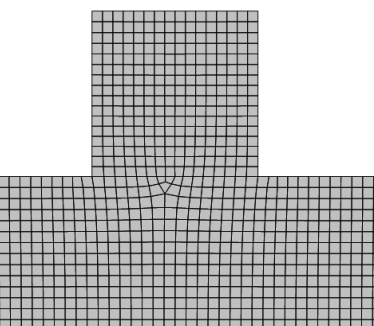
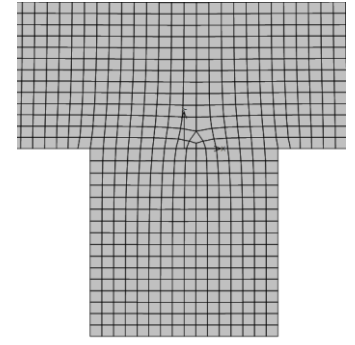
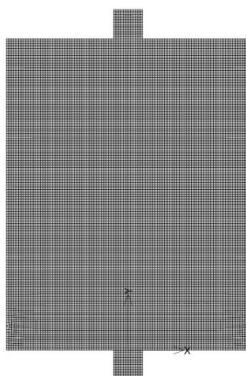
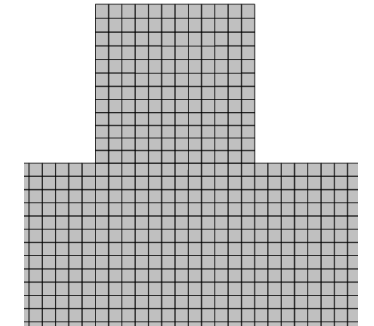
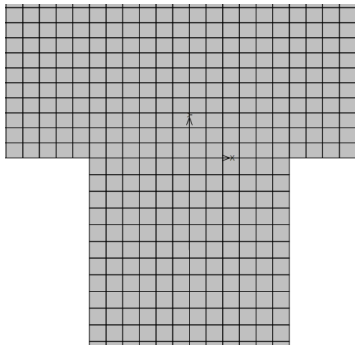
Whole specimen	Magnified upper part	Magnified bottom part
 <p data-bbox="288 837 475 869">SBeta_es10_2x2</p>		
 <p data-bbox="284 1339 481 1370">SBeta_es10_7x10</p>		
 <p data-bbox="288 1839 475 1870">SBeta_es10_8x8</p>		

Whole specimen	Magnified upper part	Magnified bottom part
 <p data-bbox="284 685 481 712">SBeta_es10_8x10</p>		
 <p data-bbox="277 1189 491 1216">SBeta_es10_10x10</p>		

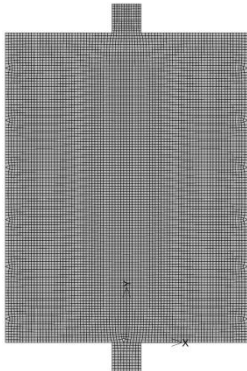
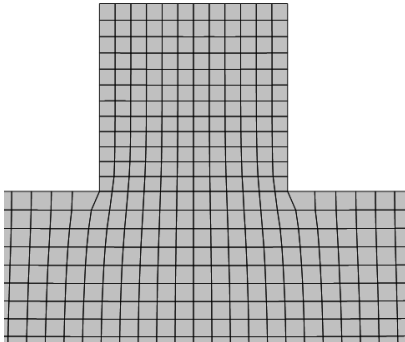
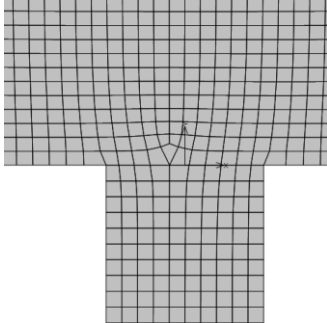
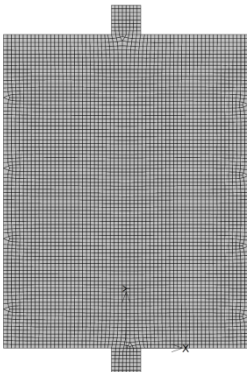
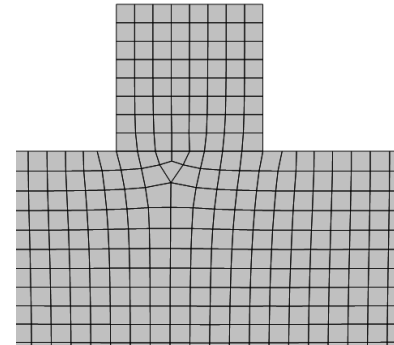
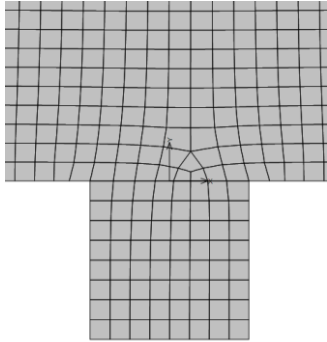
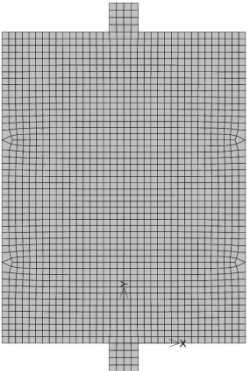
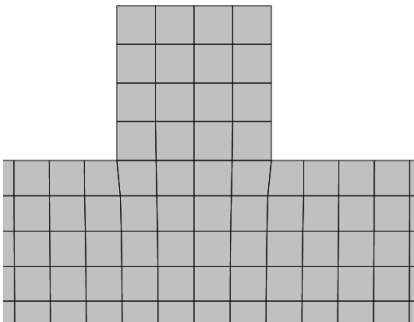
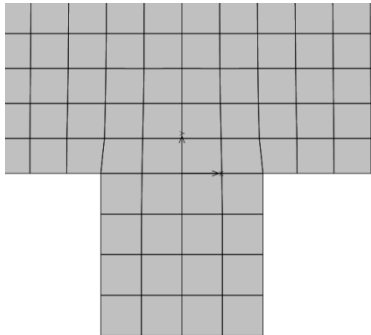
**A 2 : Mesh connectivity – crack pattern**

Loading step no.9	Loading step no.9	Loading step no.9
 <p data-bbox="288 748 472 779">SBeta_es10_2x2</p>	 <p data-bbox="699 752 898 784">SBeta_es10_7x10</p>	 <p data-bbox="1123 752 1307 784">SBeta_es10_8x8</p>
Loading step no.9	Loading step no.9	
 <p data-bbox="284 1328 486 1359">SBeta_es10_8x10</p>	 <p data-bbox="692 1332 908 1364">SBeta_es10_10x10</p>	

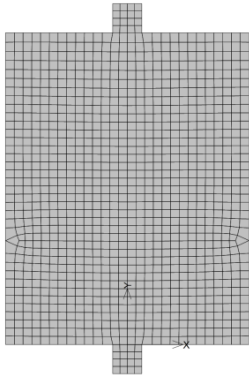
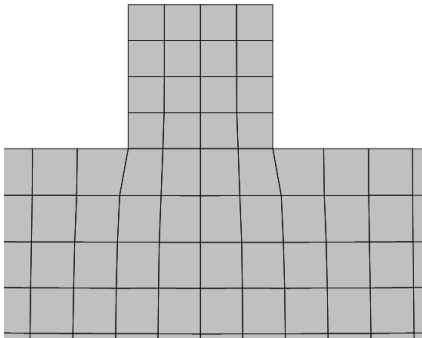
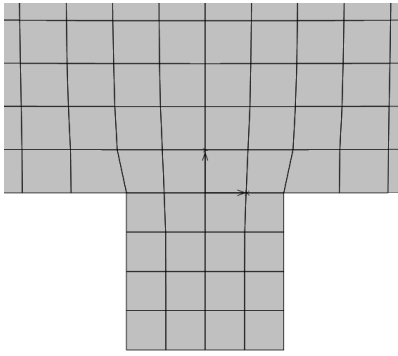
**A 3 : Mesh size – generated mesh**

Whole specimen	Magnified upper part	Magnified bottom part
 <p data-bbox="300 741 459 775">XX_es03_3x3</p>		
 <p data-bbox="300 1238 459 1272">XX_es04_4x4</p>		
 <p data-bbox="300 1736 459 1769">XX_es05_5x5</p>		

XX = SBeta or 3D Non Linear Cementitious 2 material model

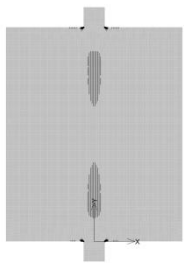
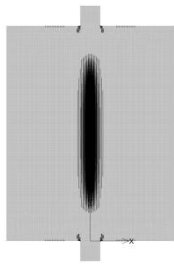
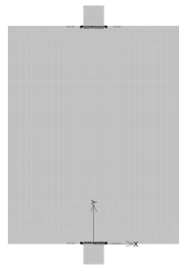
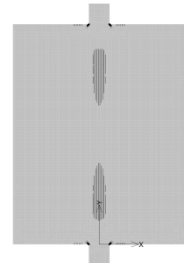
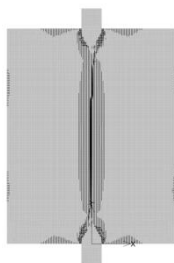
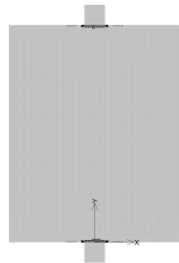
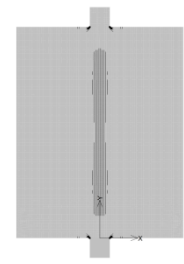
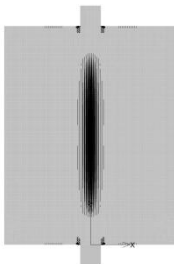
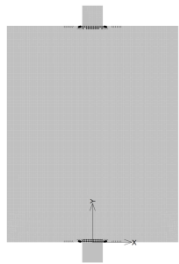
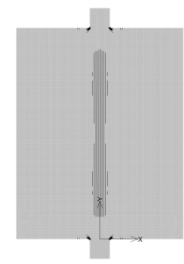
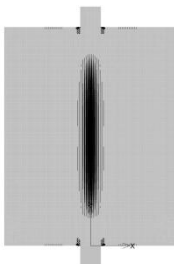
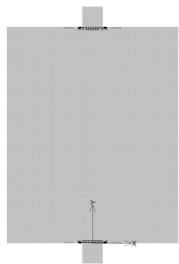
Whole specimen	Magnified upper part	Magnified bottom part
 <p data-bbox="284 680 448 712">XX_es06_5x6</p>		
 <p data-bbox="284 1180 448 1211">XX_es08_8x8</p>		
 <p data-bbox="272 1680 467 1711">XX_es14_15x15</p>		

XX = SBeta or 3D Non Linear Cementitious 2 material model

Whole specimen	Magnified upper part	Magnified bottom part
 <p>XX_es18_15x15</p>		

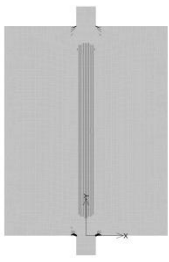
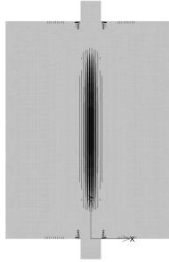
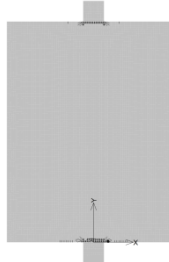
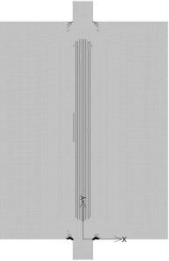
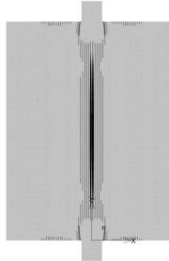

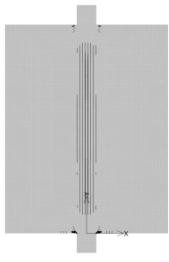
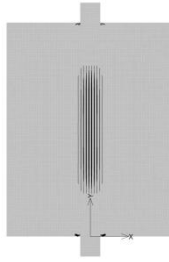
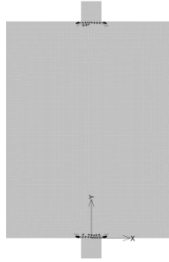
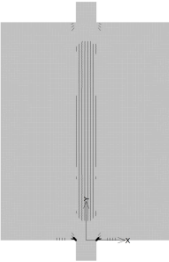
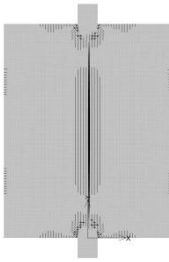
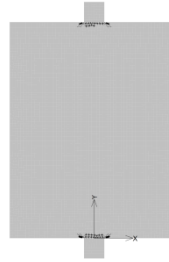
XX = SBeta or 3D Non Linear Cementitious 2 material model

**A 4 : Mesh size – crack pattern**

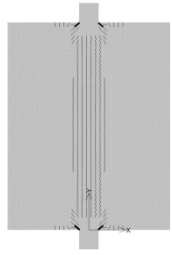
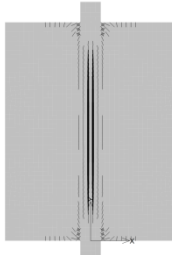
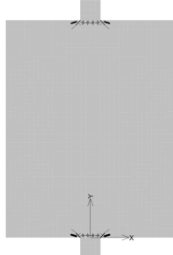
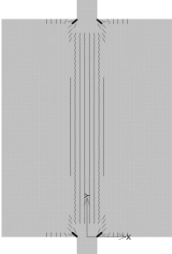
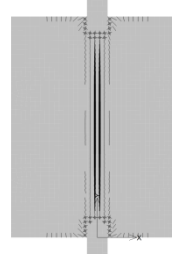
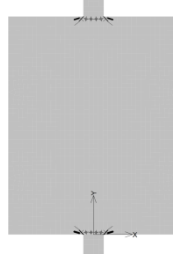
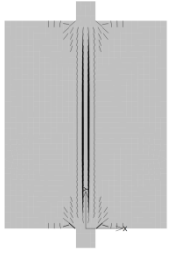
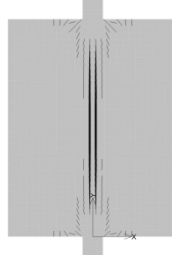
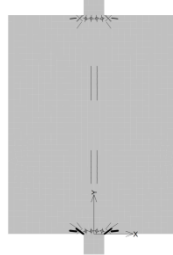
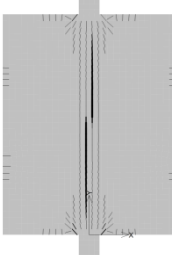
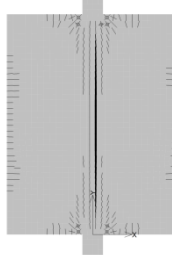
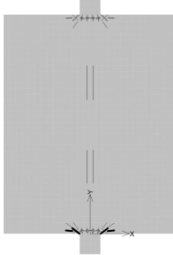
<p>Loading step no.9 (peak)</p>  <p>SBeta_es04_4x4</p>	<p>Loading step no.10 (peak)</p>  <p>NLC2sa_es04_4x4</p>	<p>Loading step no.9 (peak)</p>  <p>NLC2se_es04_4x4</p>
<p>Loading step no.10</p>  <p>SBeta_es04_4x4</p>	<p>Loading step no.11</p>  <p>NLC2sa_es04_4x4</p>	<p>Loading step no.10</p>  <p>NLC2se_es04_4x4</p>
<p>Loading step no.9 (peak)</p>  <p>SBeta_es05_5x5</p>	<p>Loading step no.10 (peak)</p>  <p>NLC2sa_es05_5x5</p>	<p>Loading step no.10 (peak)</p>  <p>NLC2se_es05_5x5</p>
<p>Loading step no.10</p>  <p>SBeta_es05_5x5</p>	<p>Loading step no.11</p>  <p>NLC2sa_es05_5x5</p>	<p>Loading step no.11</p>  <p>NLC2se_es05_5x5</p>

(peak) = peak point of load–displacement curve at given step



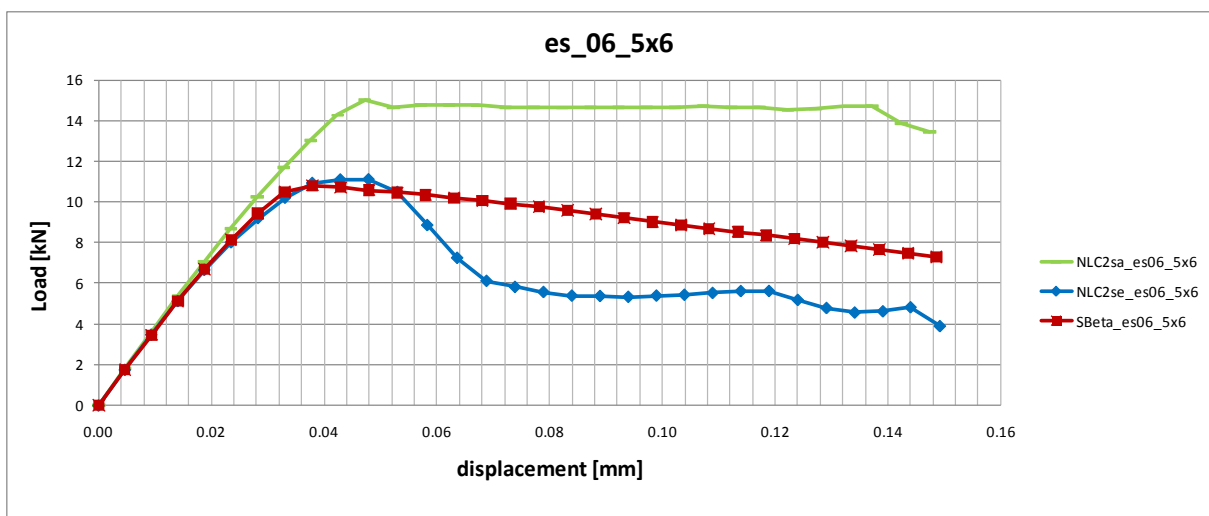
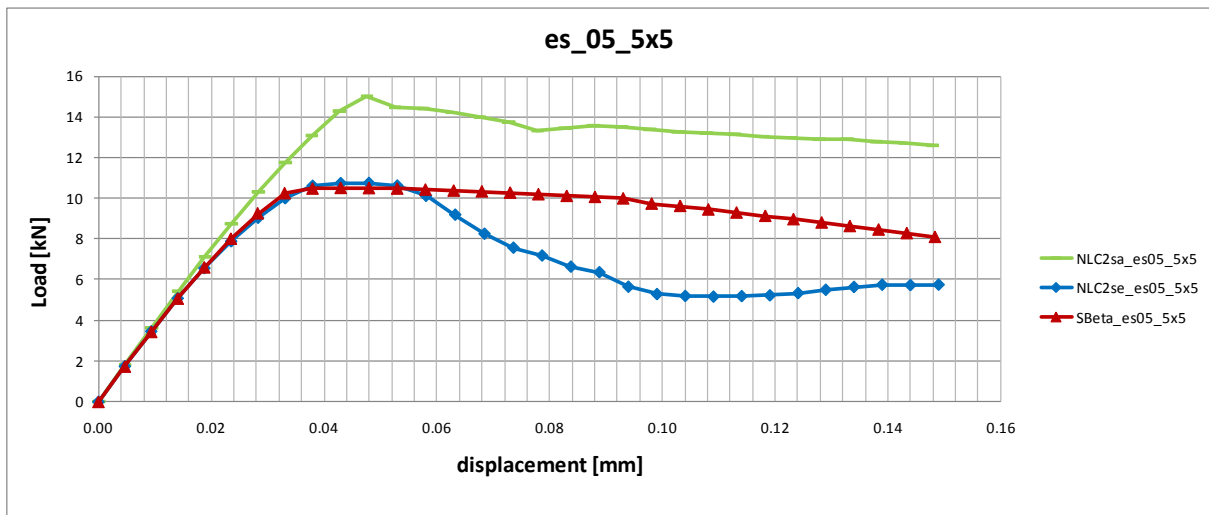
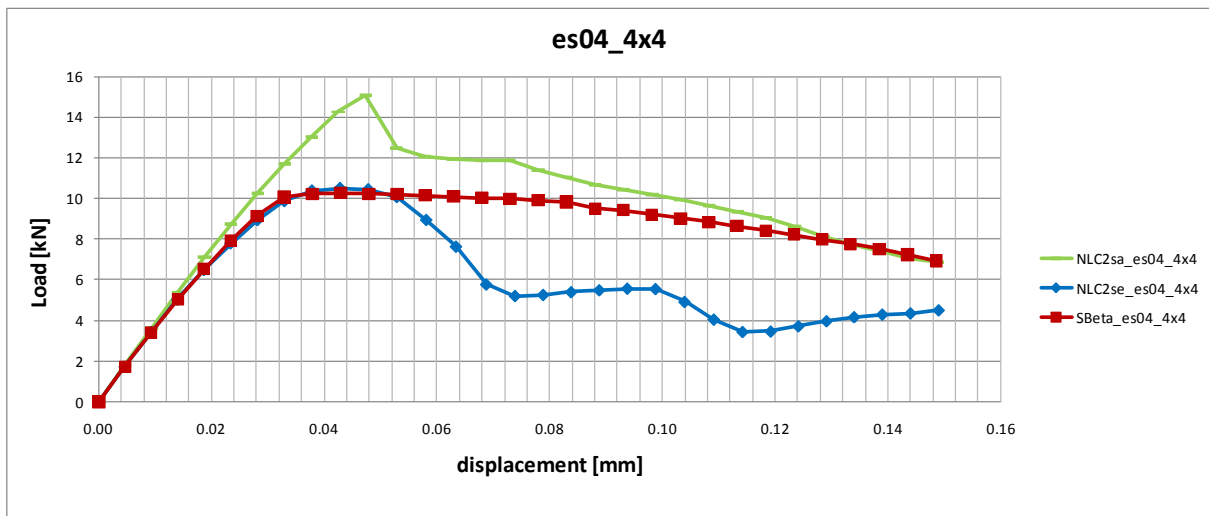
<p>Loading step no.8 (peak)</p>  <p>SBeta_es06_5x6</p>	<p>Loading step no.10 (peak)</p>  <p>NLC2sa_es06_5x6</p>	<p>Loading step no.10 (peak)</p>  <p>NLC2se_es06_5x6</p>
<p>Loading step no.9</p>  <p>SBeta_es06_5x6</p>	<p>Loading step no.11</p>  <p>NLC2sa_es06_5x6</p>	<p>Loading step no.11</p>  <p>NLC2se_es06_5x6</p>
<p>Loading step no.9 (peak)</p>  <p>SBeta_es08_8x8</p>	<p>Loading step no.9 (peak)</p>  <p>NLC2sa_es08_8x8</p>	<p>Loading step no.10(peak)</p>  <p>NLC2se_es08_8x8</p>
<p>Loading step no.10</p>  <p>SBeta_es08_8x8</p>	<p>Loading step no.10</p>  <p>NLC2sa_es08_8x8</p>	<p>Loading step no.11</p>  <p>NLC2se_es08_8x8</p>

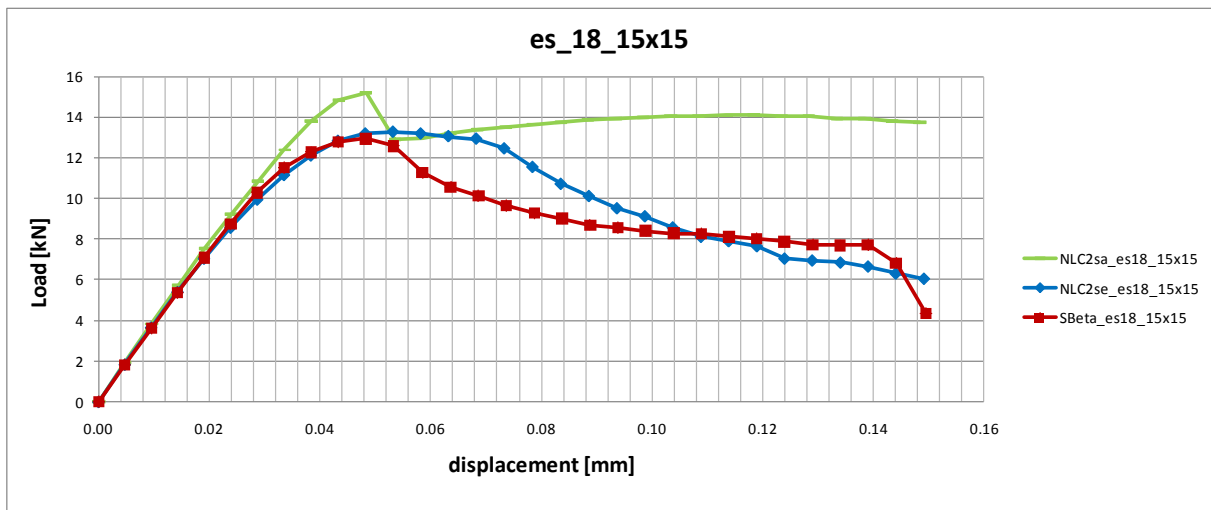
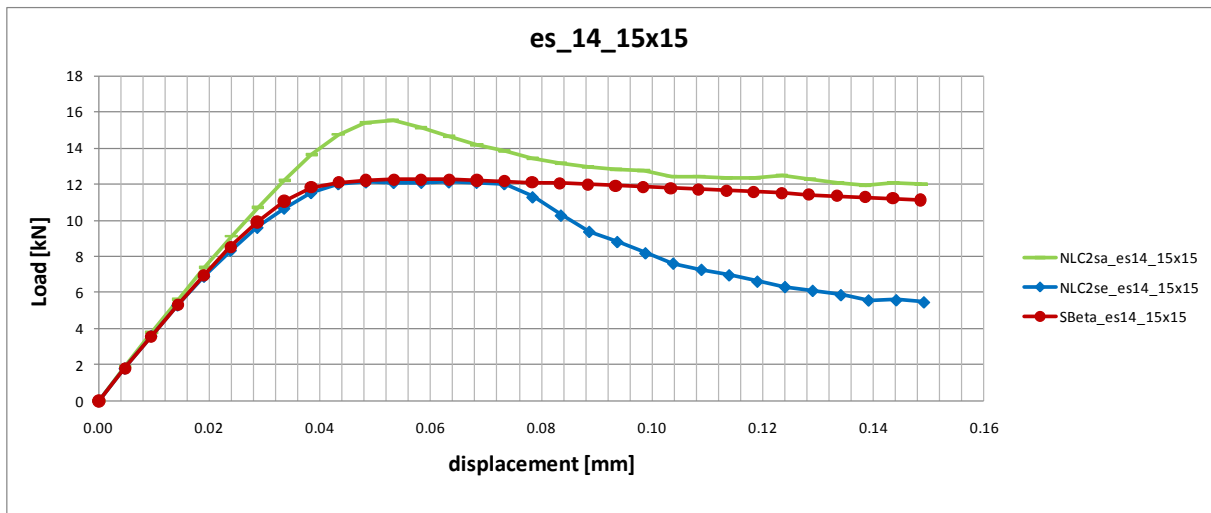
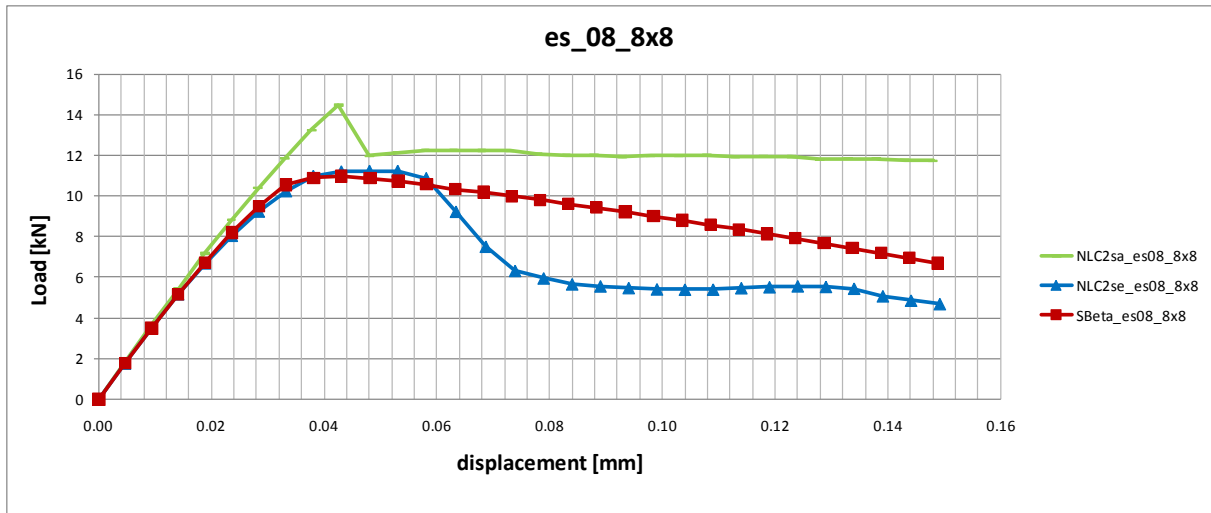
(peak) = peak point of load–displacement curve at given step

<p>Loading step no.12 (peak)</p>  <p>SBeta_es14_15x15</p>	<p>Loading step no.11 (peak)</p>  <p>NLC2sa_es14_15x15</p>	<p>Loading step no.13 (peak)</p>  <p>NLC2se_es14_15x15</p>
<p>Loading step no.13</p>  <p>SBeta_es14_15x15</p>	<p>Loading step no.12</p>  <p>NLC2sa_es14_15x15</p>	<p>Loading step no.14</p>  <p>NLC2se_es14_15x15</p>
<p>Loading step no.10 (peak)</p>  <p>SBeta_es18_15x15</p>	<p>Loading step no.10 (peak)</p>  <p>NLC2sa_es18_15x15</p>	<p>Loading step no.11(peak)</p>  <p>NLC2se_es18_15x15</p>
<p>Loading step no.11</p>  <p>SBeta_es18_15x15</p>	<p>Loading step no.11</p>  <p>NLC2sa_es18_15x15</p>	<p>Loading step no.12</p>  <p>NLC2se_es18_15x15</p>

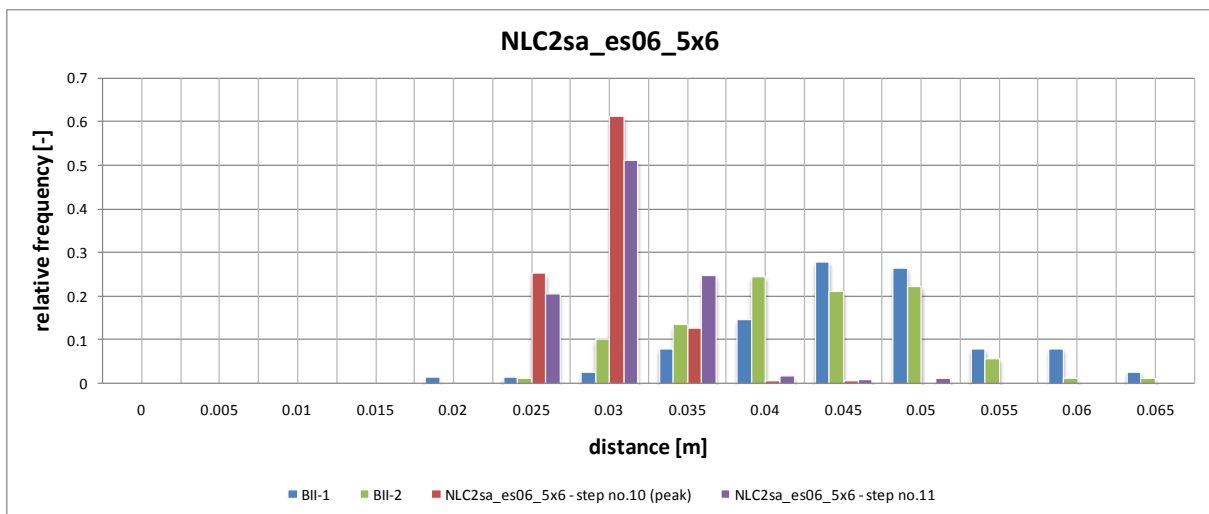
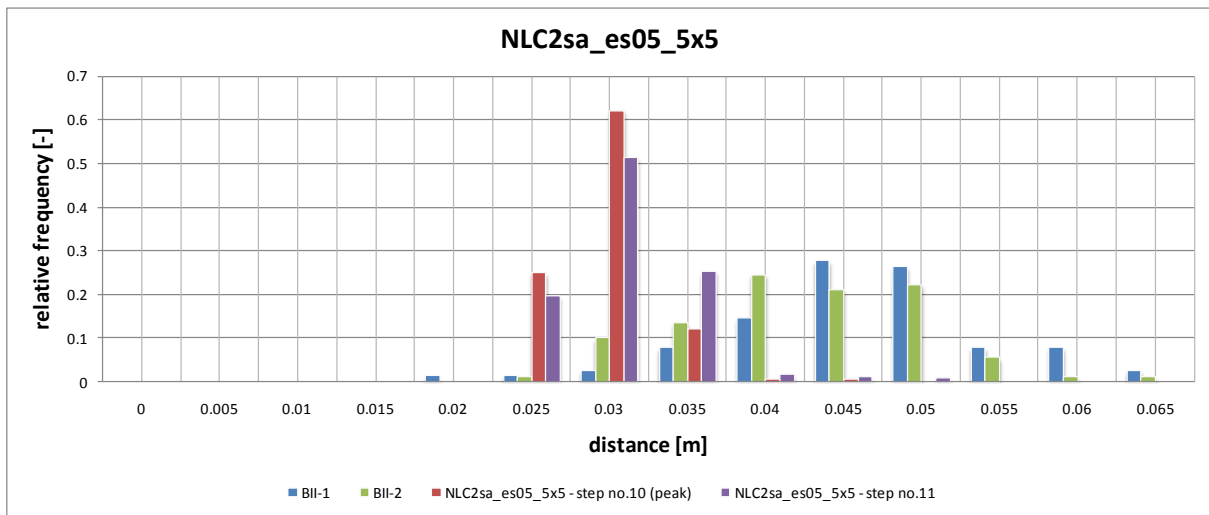
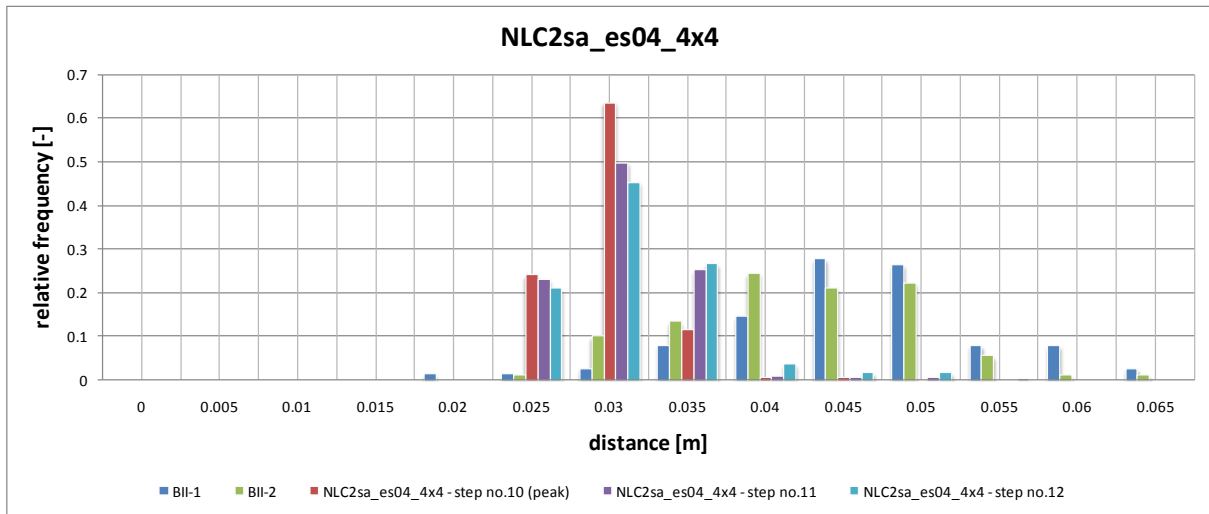
(peak) = peak point of load–displacement curve at given step

**A 5 : Material model – load–displacement curves**

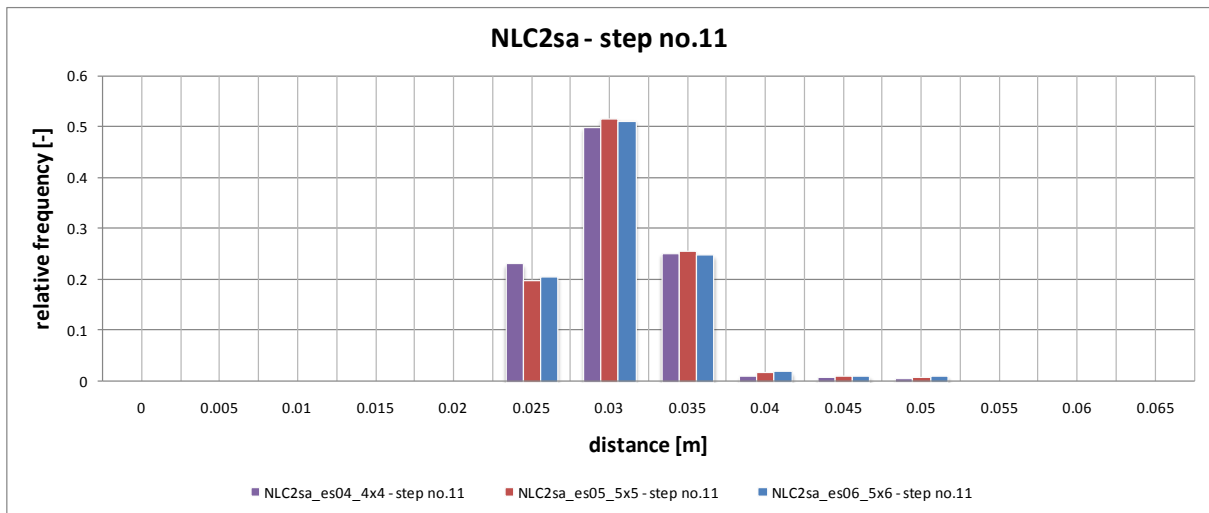
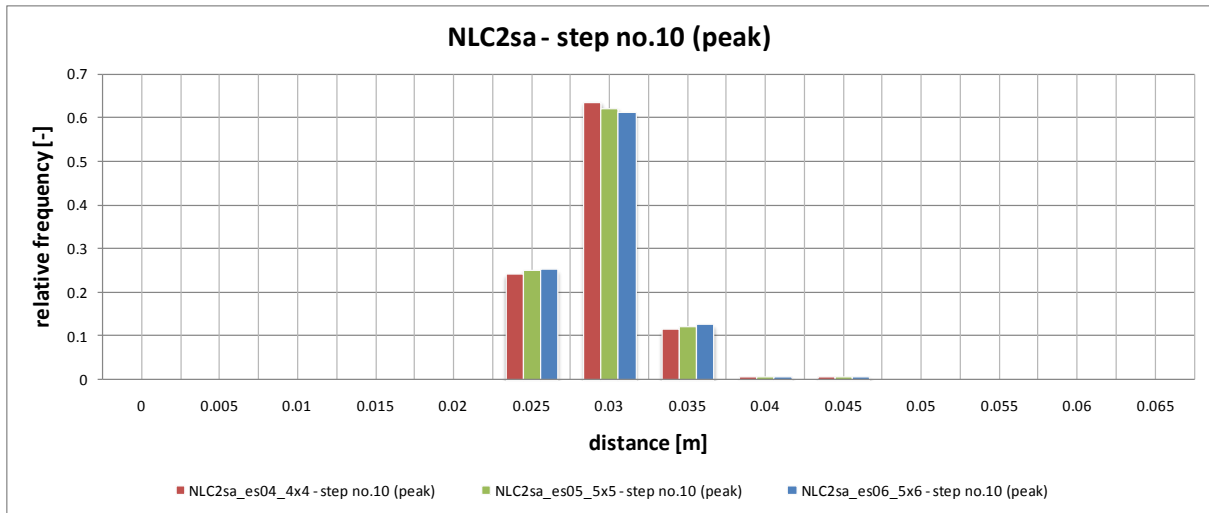




**A 6 : Failure location in 2D (AE + EME) – distances of fracture events**

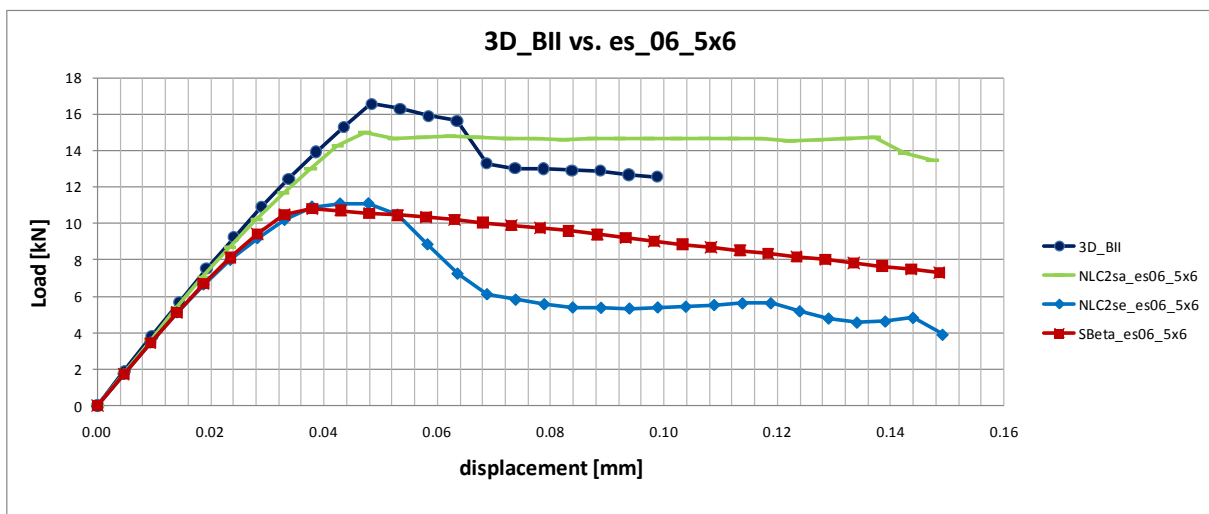
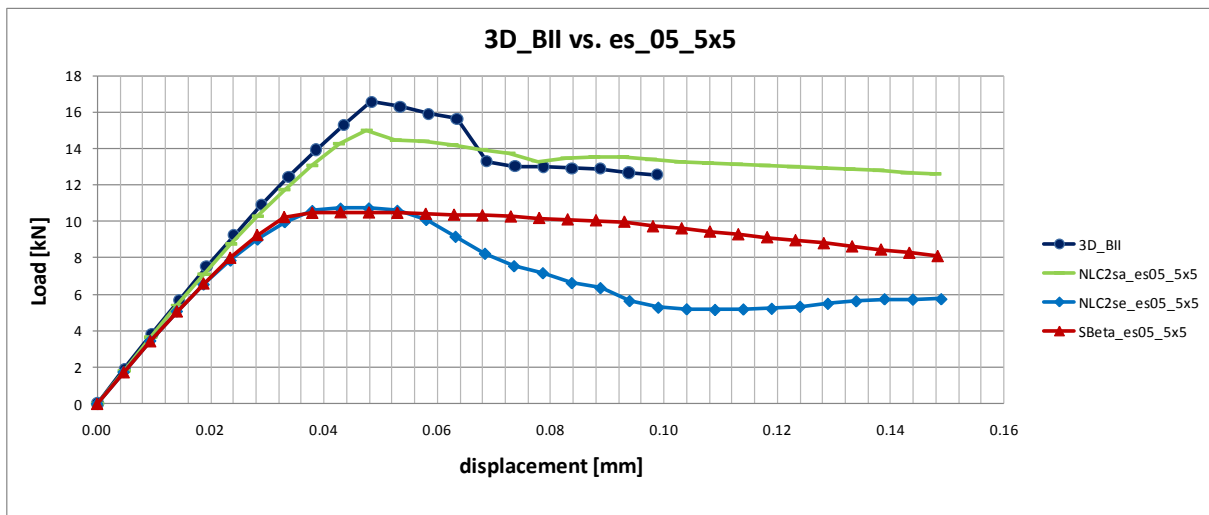
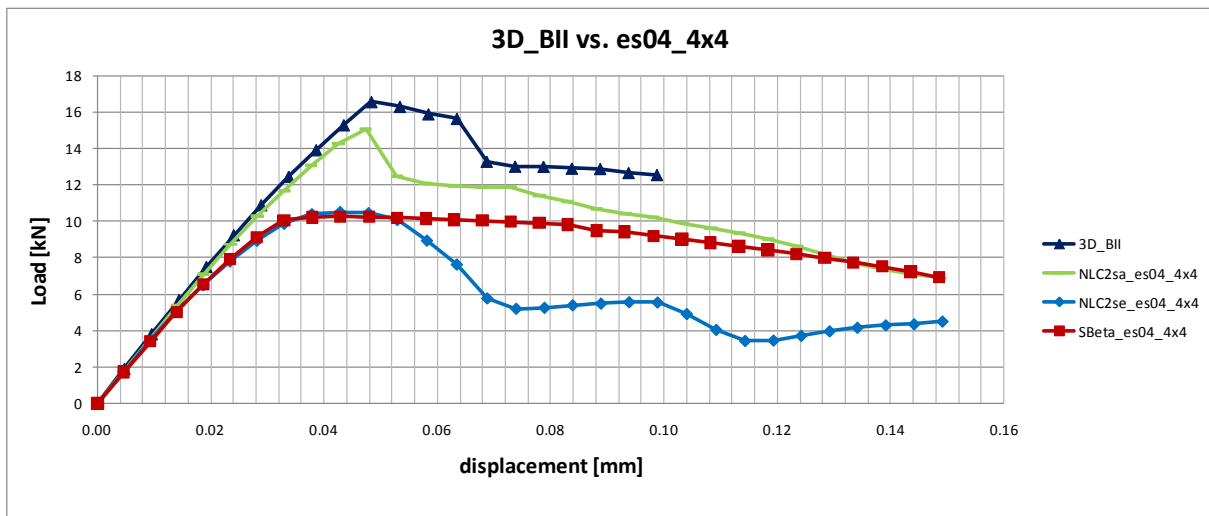


(peak) = peak point of load–displacement curve at given step

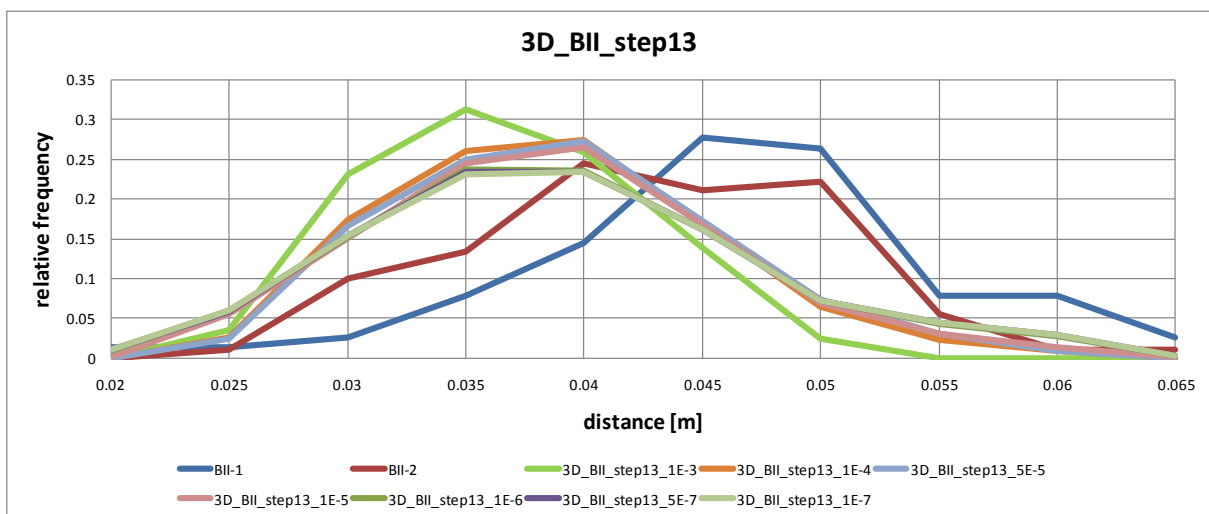
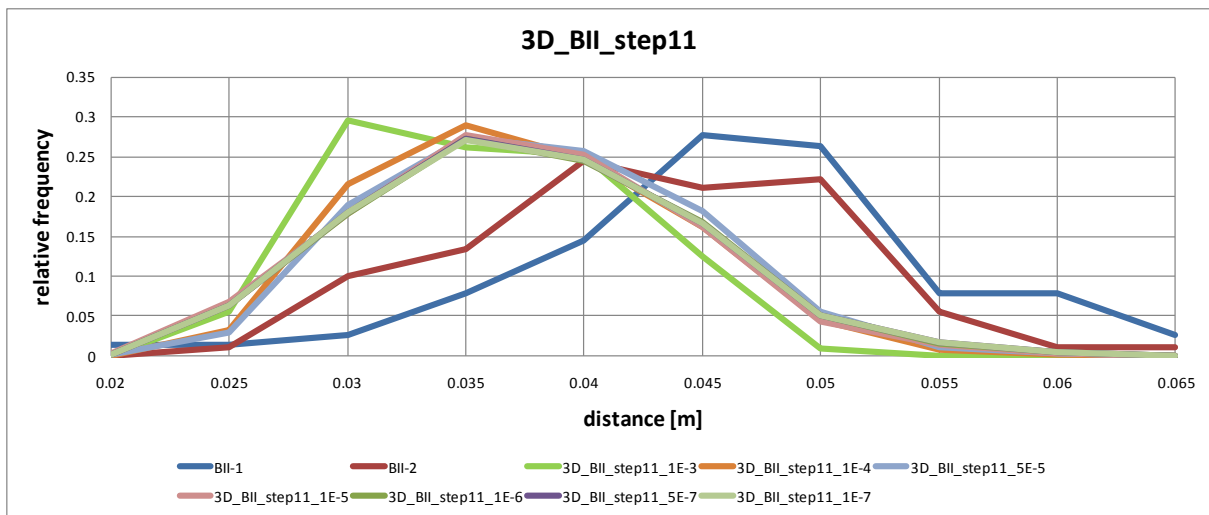
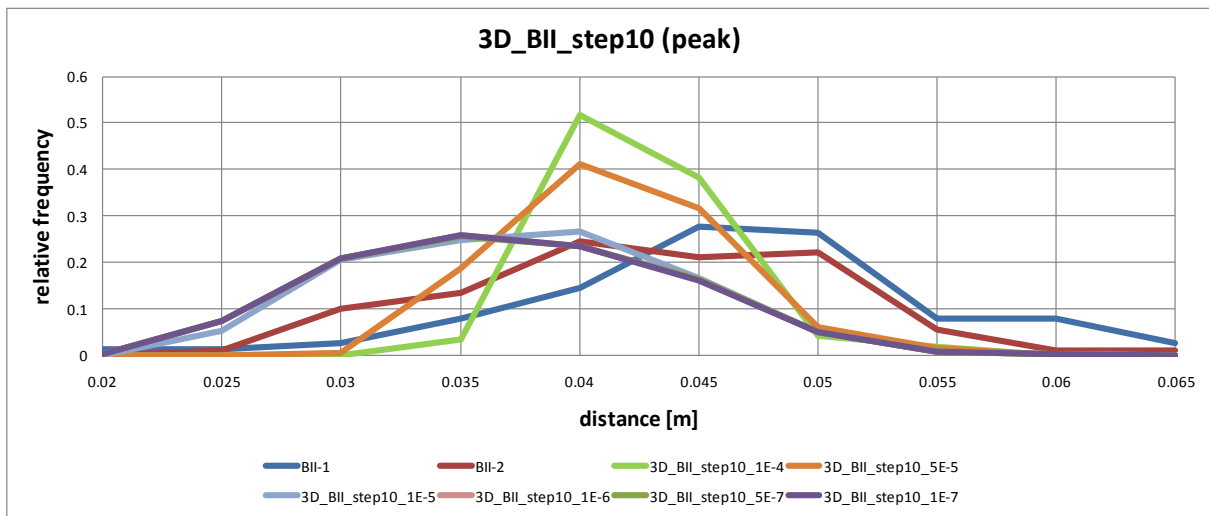


(peak) = peak point of load–displacement curve at given step

**A 7 : Failure location in 3D (AE + EME) – load–displacement curves**



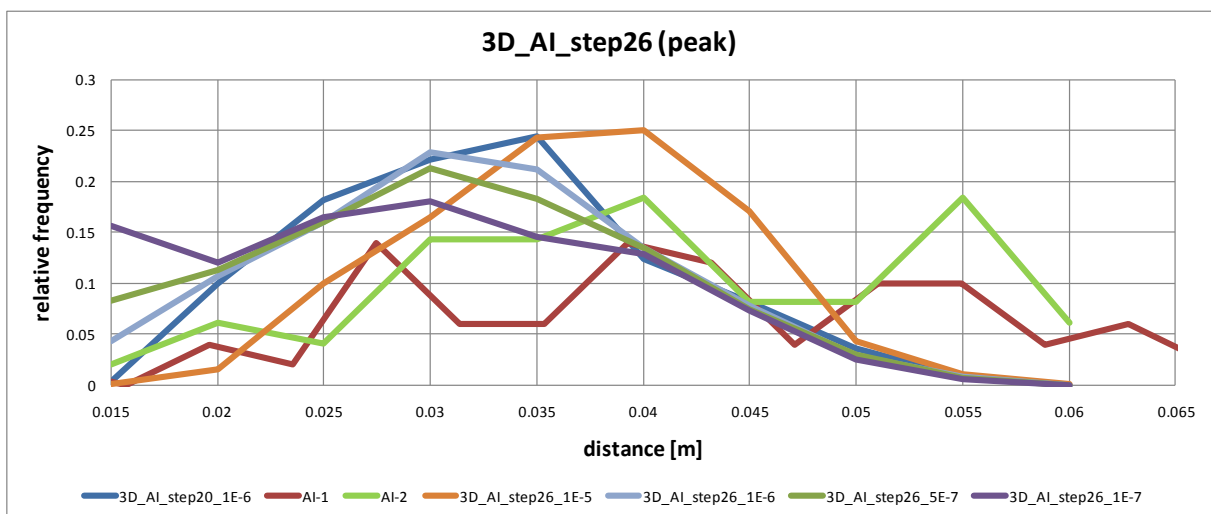
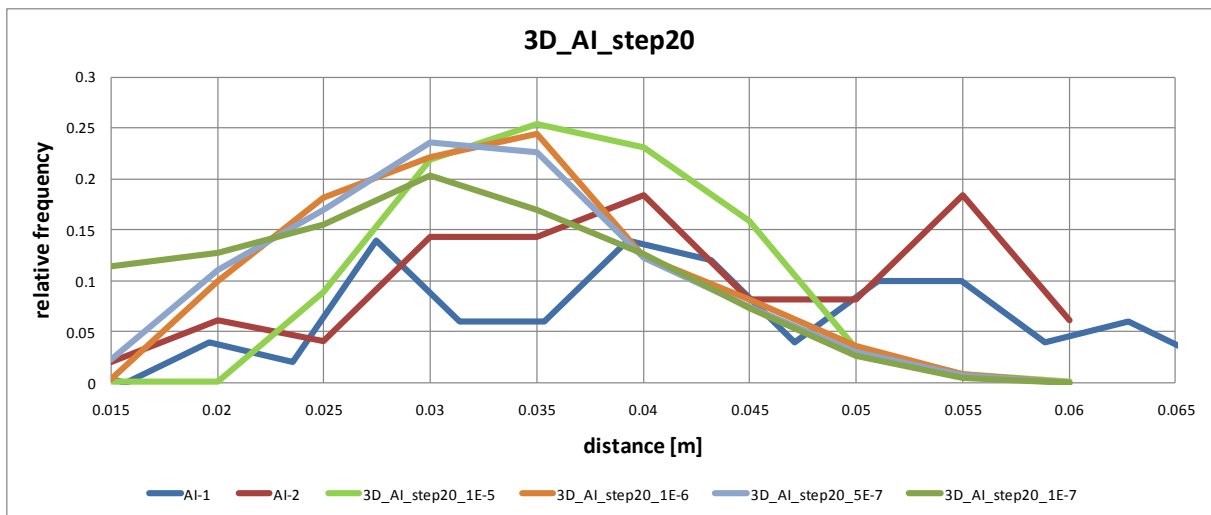
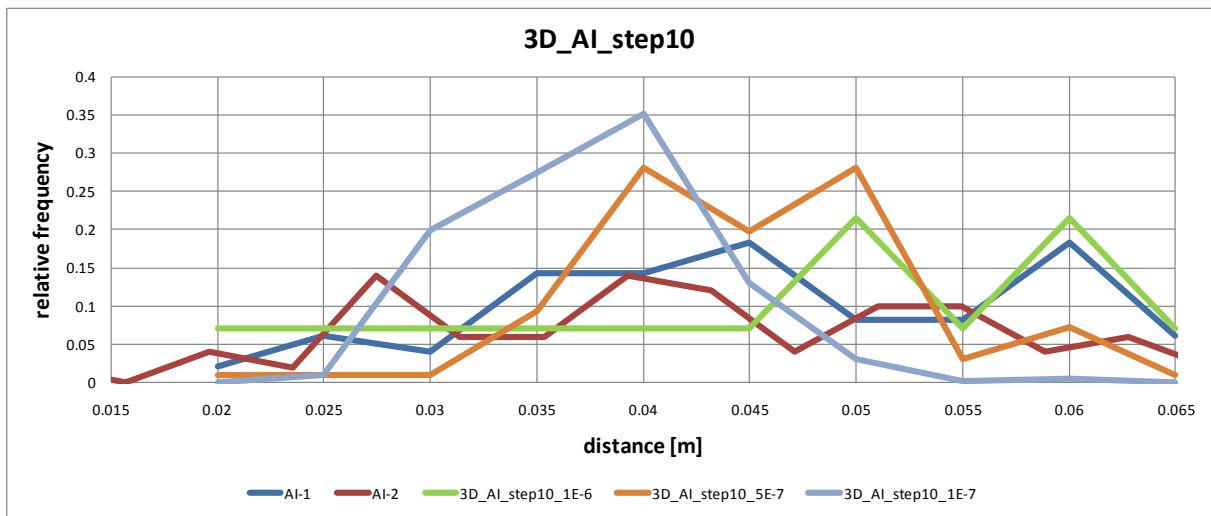
**A 8 : Failure location in 3D (AE + EME) – distances of fracture events for 3D\_BII**



(peak) = peak point of load–displacement curve at given step

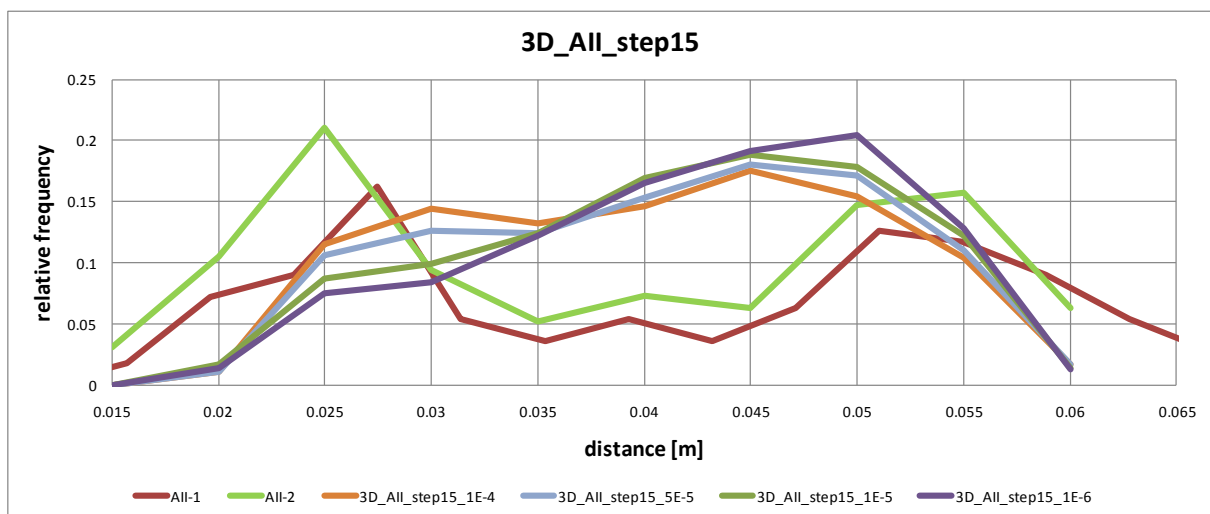
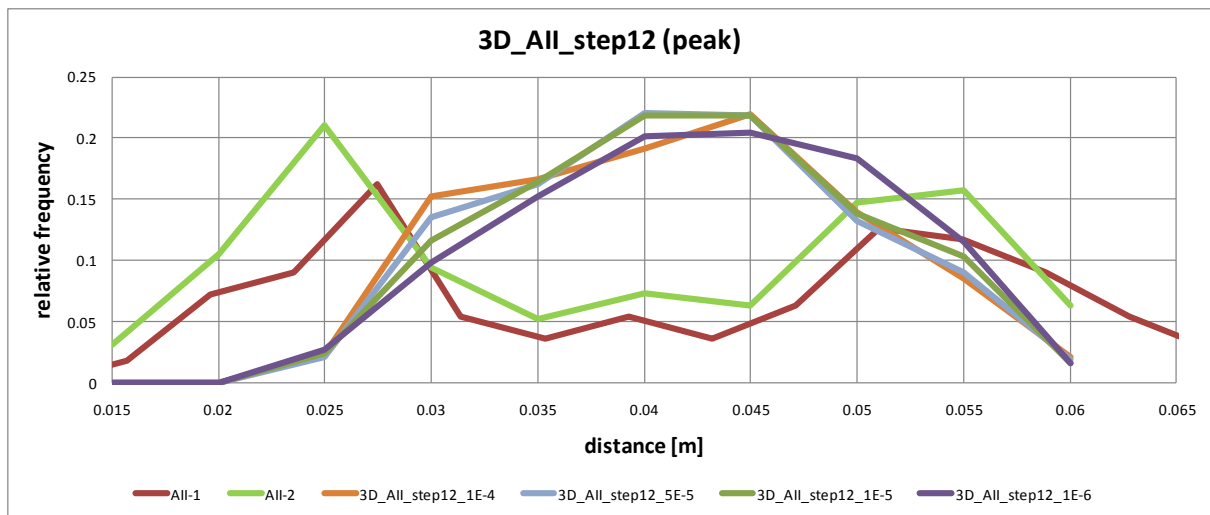
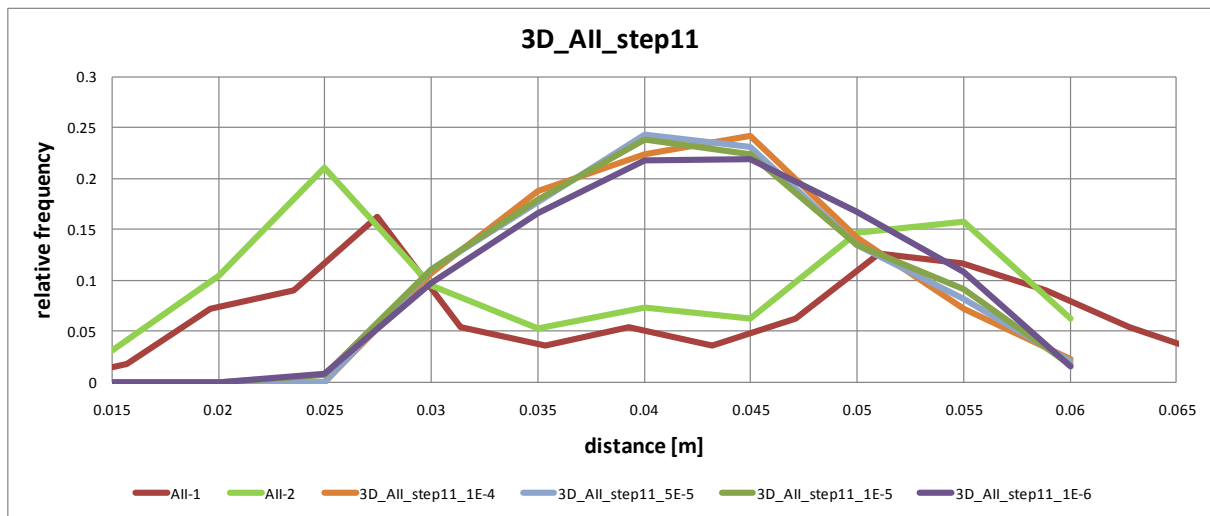


**A 9 : Failure location in 3D (AE + EME) – distances of fracture events for 3D\_AI**



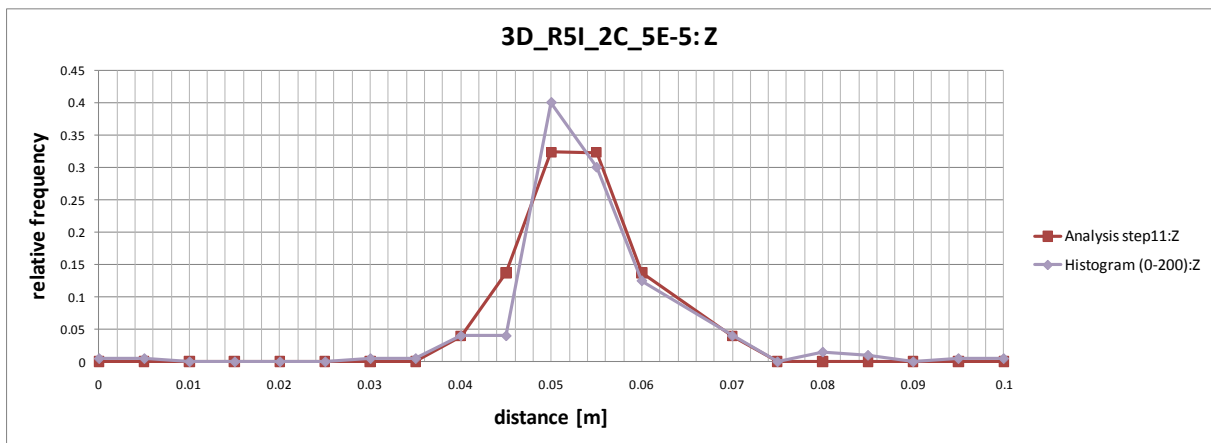
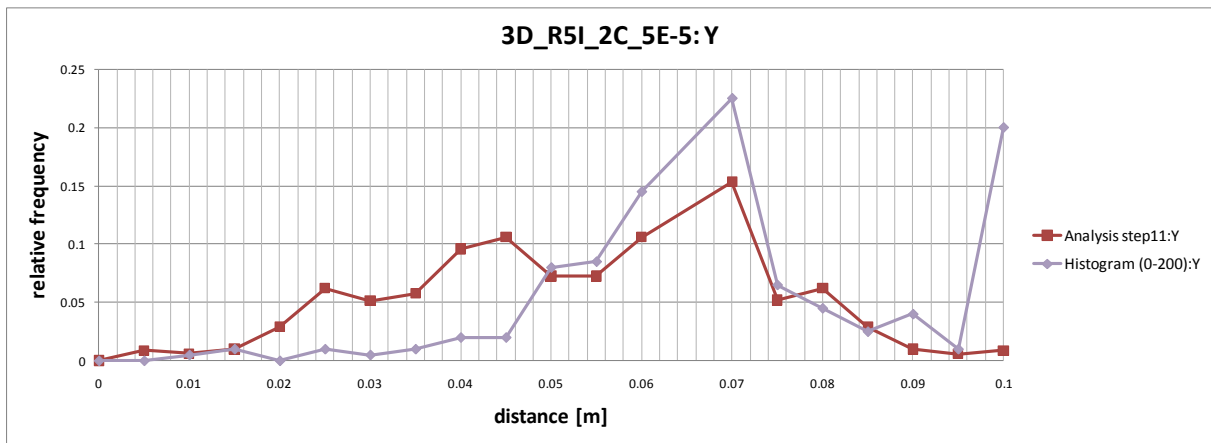
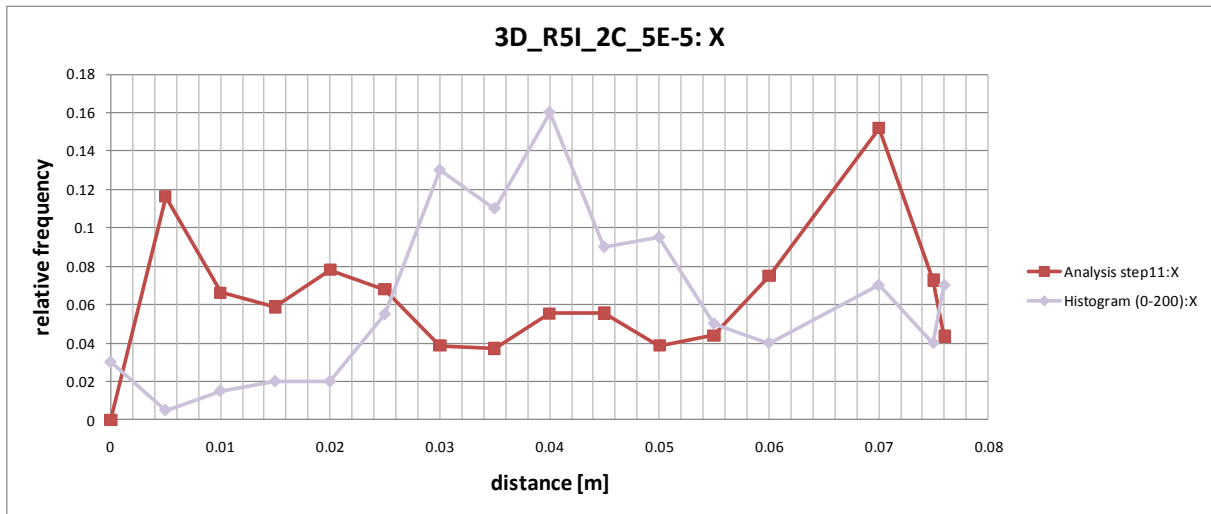
(peak) = peak point of load–displacement curve at given step

**A 10 : Failure location in 3D (AE + EME) – distances of fracture events for 3D\_AII**



(peak) = peak point of load–displacement curve at given step

**A 11 : Failure location in 3D (AE) – distances of fracture events for 3D\_R5I\_2C\_5E-5**



**A 12 : Failure location in 3D (AE) – load–displacement curves for R5I\_2C**